Designing of hetero-bimetallic cyclic trinuclear, polymeric chains, and linear trinuclear from Cu(II), Fe(III), and Co(III) complexes using alkali, alkaline, and transition metal ions

By

Chanreingam L

Roll No. 186122009

Thesis Supervisor

Prof. Manabendra Ray

Department of Chemistry

Indian Institute of Technology Guwahati,

Guwahati-781039

भारतीय प्रौद्योगिकी संस्थान गुवाहाटी
Indian Institute of Technology Guwahati

INDIAN INSTITUTE OF TECHNOLOGY GUWAHATI

Department of Chemistry

STATEMENT

I hereby declare that the matter embodied in this thesis is the result of investigations carried out by me in the Department of Chemistry, Indian Institute of Technology Guwahati, India under the supervision of Prof. Manabendra Ray, Professor, Department of Chemistry, Indian Institute of Technology Guwahati, India.

In keeping with the general practice of reporting observations, due acknowledgements have been made wherever the work described is based on the findings of other investigations.

December, 2023

I. I. T. Guwahati Chanreingam.L

Prof. Manabendra Ray
Professor
Indian Institute of Technology Guwahati
Department of Chemistry
Tel. 91 361 258 2310
Fax.91 361 258 2349

CERTIFICATE

This is to certify that Mr. Chanreingam. L has been working under my supervision since July 2018. I am forwarding his thesis, entitled, "**Designing of hetero-bimetallic cyclic trinuclear, polymeric chain, and linear trinuclear from Cu(II), Fe(III), and Co(III) complexes using alkali, alkaline, and transition metal ions"** being submitted for the degree of Doctorate of Philosophy of this Institute. I certify that he has fulfilled all the requirements according to the rules of this Institute and that the investigations embodied in this thesis have not been submitted elsewhere for a degree.

December, 2023
I. I. T. Guwahati

Prof. Manabendra Ray
Supervisor

Acknowledgement

As I reached towards the completion of my Ph.D journey. I take this opportunity to express my deep sense of gratitude and appreciation towards my supervisor Prof. Manabendra Ray, Department of Chemistry, IIT Guwahati for his excellent guidance, tireless efforts, patience, kindness and moral support at each and every step of my research work, He have been an inspiration to me. He helped me to recognize what was important and made many contributions to this work. I am fortunate enough to have his teaching about how to cultivate scientific thoughts.

I would like to acknowledge my sincere gratitude to the chairman of my doctoral committee, Prof. Gopal Das and the members of the Doctoral Committee, Prof. Chandan. K. Jana and Prof. Animesh. Das, for their insightful advice and valuable suggestions to improve the quality of my research work.

I also express my sincere thanks to all faculty members, of the Department of Chemistry, IIT Guwahati for their help and encouragement.

I am thankful to the Institute, Indian Institute of Technology Guwahati for providing me with the state-of-the-art infrastructure and facilities for advanced research.

I am grateful to all non-teaching staff of the Department for their technical support.

I would like to thank DST under FIST program for providing single crystal XRD instrument.

I acknowledge, Ministry of Education (MoE) India for the research scholarship.

I would like to thank my former group members Dr. Sounak. Bhattacharya and Dr. Jinat Aktar for their timely help, support and for the wonderful time we shared during this period.

I would like to thank Dr Tanmay Dutta not only for the time we spent together but for the moral support and assist that I received from him including the technical part.

I would like to thank my present group member, Mr. Somnath Paik for the time we spent together and the suggestion.

I am thankful to all research scholars especially the 2018 batch, Department of Chemistry, IIT Guwahati for their help.

I wish to thank my childhood friends Tek and Tek for accompanying me in my harder days of my life.

At last, but not least, I want to express my sincere thanks to all of my family members, especially to my Father (Shri- Katuingam. L), Mother (Smt. Rapungla. L), Sisters (Ningamla. L), and (Phylathing. L) for their constant encouragements and moral supports during my research work.

Chanreingam. L

Synopsis of the thesis

Alkali metal ions are among the most abundant metal ions on earth's crust and in the human body.[1] Their biological functions are well-known and well-studied.[1] However, mimicking their binding in biology proved to be challenging. The limitation stems from their lack of binding to ligands through conventional coordination bonds. Their bonding to a hard ligand such as carboxylate, ether, or other oxygen donors is predominantly ionic and labile. These led to the development of organic crown ethers and cryptands.[2] The synthesis of metallacrowns, metal complexes that bind alkali ions similarly to crown ethers, showed that incorporating transition metal complexes has benefits.[3] Having transition metals along with alkali ions gives materials extra functions that organic crown ethers can't perform.[4] Metallacrowns have demonstrated functions as diverse as the stabilization of unstable molecules, single-molecule magnets, and anion recognition agents, to name a few.[5] Alkali metal ions have also been incorporated within the metal-organic framework (MOF) to synthesize interlocked molecules and in supramolecular metal-organic complexes (MOCs).[6] MOCs are distinctly different from MOFs. MOFs are coordination polymers and thus insoluble in most solvents by design.[7] As MOC are the assembly of molecules bound together through noncovalent or weaker bonds, they can be soluble, retaining their structure in solution.[8] Many MOCs have been reported with porous structures retained in solution. The research community has witnessed the prominent growth of chiral Metal-organic complexes (CMOCs) at the forefront of chiral solid-state materials and chiral technology over the past two decades.[9] The realm of CMOCs for enantioselective applications is still under fast development, and several reviews have covered the targeted synthesis of CMOCs for asymmetric heterogeneous catalysis and separation, including asymmetric catalysis, enantioselective separation, enantioselective recognition, sensing, and drug delivery.[9]

[1] A. Sigel, The alkali metal ions: their role for life, *Springer Berlin Heidelberg*, New York, NY, **2015**.

[2] S. O. Kang, J. M. Llinares, V. W. Day and K. Bowman-James, *Chem. Soc. Rev.*, 2010, **39**, 3980.

[3] A. J. Ryan, J. W. Ziller and W. J. Evans, *Chem. Sci.*, 2020, **11**, 2006–2014.

[4] G. Mezei, C. M. Zaleski and V. L. Pecoraro, *Chem. Rev.*, 2007, **107**, 4933–5003.

[5] J. Jankolovits, K. N. Raymond and V. L. Pecoraro, *Angew. Chem. Int. Ed.*, 2011, **50**, 9660– 9664.

Chapter I

Introduction

This chapter summarizes the literature on:

1. Water-soluble Metal-Organic Complexes (MOCs)
2. Chiral Metal-Organic Complexes (MOCs) and its advantages
3. Heterobimetallic complexes, sensing of spectroscopically silent metal ions
4. Metal-organic complex of reduced Schiff base ligands

Based on these information's, the objectives of the thesis have been defined.

Chapter II

Self-assembly-triggered *trans-to-cis* conversion of mononuclear Cu(II) via cyclic chiral tri-nuclear assembly

In this chapter, we used L-phenylalanine derived ligand ($H_2L^{L\text{-phe}}$) and synthesized Cu(II) monomer complex, which obtained facial and *trans*-oriented geometry. Using this monomer, we synthesized cyclic trinuclear[10] just by reacting with KNO_3 in MeOH. Structural characterization showed three $[Cu(HL^{L\text{-phe}})_2]$ units encapsulated K^+ similar to organic crown ethers/cryptand (Figure 1). Electrospray Ionization (ESI)-mass spectra of the assemblies in DMF showed the retention of assemblies in the solution.

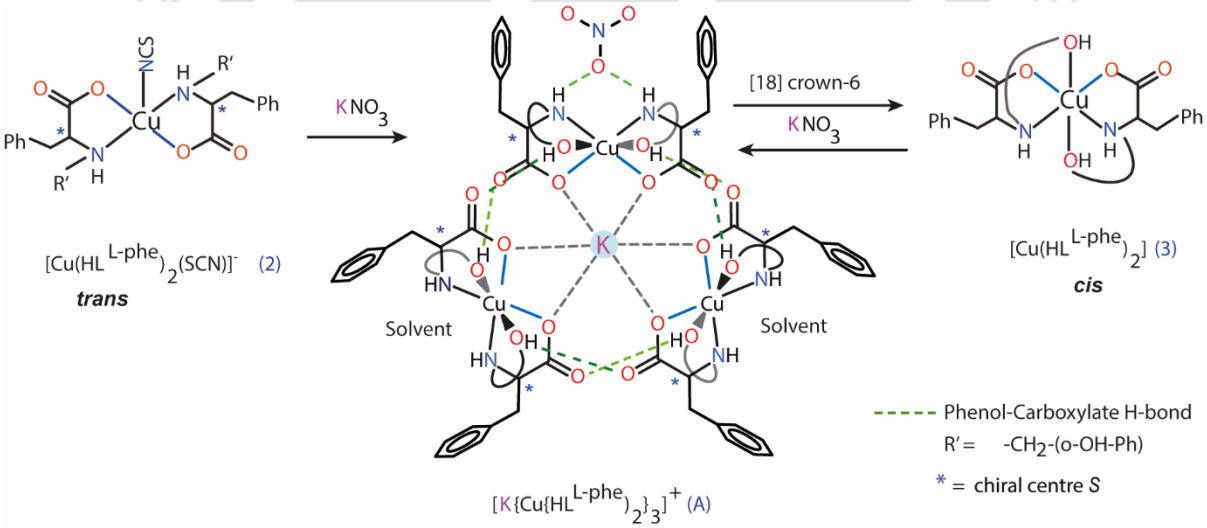

Figure 1. Sketch model of the synthesis of assembly and disassembly.

The three $[Cu(HL^{L\text{-phe}})_2]$ units in the assembly are exclusively *cis*-oriented octahedral. We called it K^+-induced *trans-to-cis* conversion. The K-$O_{carboxylates}$ bond lengths are 2.73 Å. When compared to [18]crown-6 potassium K-O bond lengths (2.7 Å), they are very closed.[11] Taking

advantage of the K^+ strong affinity to crown ether, we used an excess of [18] crown-6 and removed the K^+ from the assembly, thereby obtaining a cis-oriented Cu(II) monomer where the *cis*- identity of the Cu(II) in the assembly was retained. The *cis*-oriented disassembled Cu(II) monomer, when reacted with $K^{+,}$ forms back the assembly. Therefore, assembly formation and disassembly are reversible processes. The process can be monitored by UV-visible and ESI-Mass techniques.

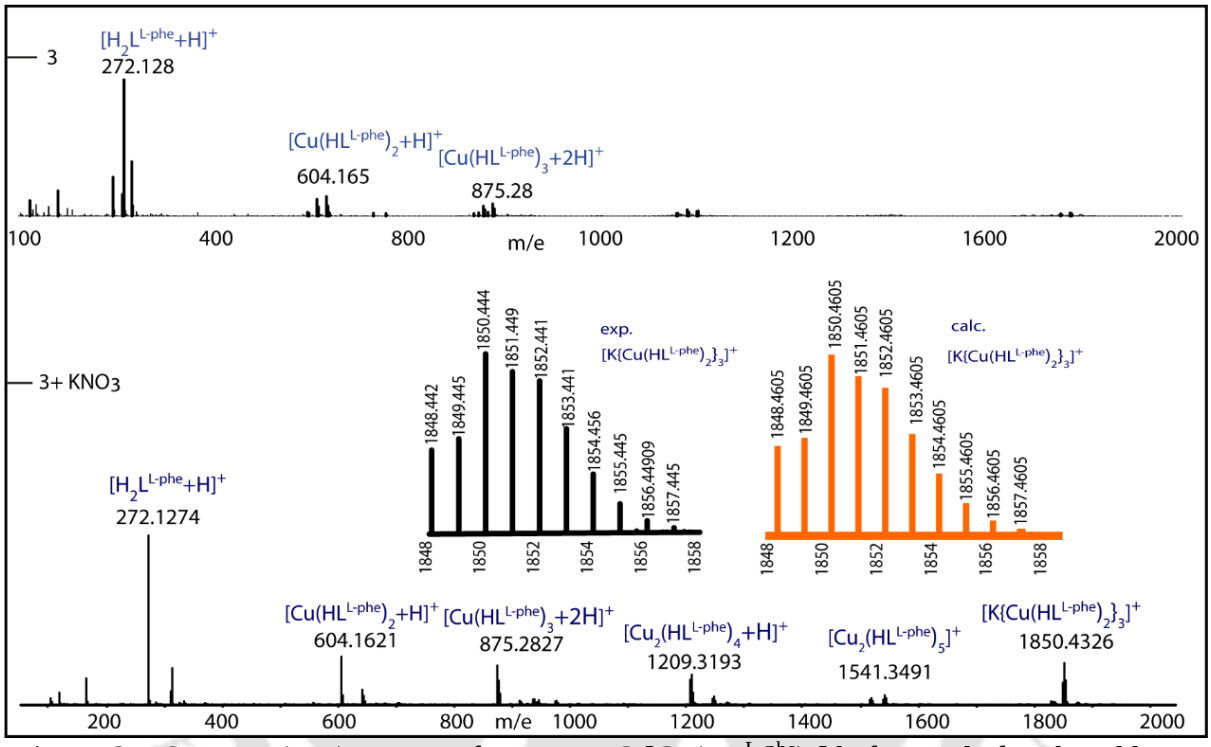

Figure 2. ESI-Mass (+ve) spectra of monomer **3** $[Cu(HL^{L\text{-}phe})_2]$ before and after the addition of KNO_3.

[6] S. Burazer, F. Morelle, Y. Filinchuk, R. Černý and J. Popović, *Inorg. Chem.*, 2019, **58**, 6927–6933

[7] M. Liu, L. Zhang and T. Wang, *Chem. Rev.*, 2015, **115**, 7304–7397.

[8] P. J. Low, J. Jiang and Y. Cui, *J. Am. Chem. Soc.*, 2017, **139**, 1554–1564.

[9] L. Ma, C. Abney and W. Lin, *Chem. Soc. Rev.*, 2009, **38**, 1248.

[10] M. Dubey, R. R. Koner and M. Ray, *Inorg. Chem.*, 2009, **48**, 9294–9302.

[11] M. Sellin and M. Malischewski, *Acta Crystallogr. E: Crystallogr. Commun.*, 2019, **75**, 1871-1874.

[12] A. H. Reath, J. W. Ziller, C. Tsay, A. J. Ryan and J. Y. Yang, *Inorg. Chem.*, 2017, **56**, 3713–3718.

[13] A. Kumar, D. Lionetti, V. W. Day and J. D. Blakemore, *Chem. – Eur. J.*, 2018, **24**, 141–149.

Chapter III

Redesigning of cyclic chiral trinuclear by changing amino acid sidearm, using inert Co(III) complex, and cation of different sizes and charges

In the previous chapter, we synthesized the Cu(II) monomer bis complex and its trinuclear assembly of the phenylalanine-derived reduced Schiff base, which has an aromatic sidearm. However, the complexes are insoluble in most of the solvents. Therefore, in this chapter, we synthesized the L-serine-derived reduced Schiff base, which has a hydrophilic side-arm (Figure 3). We intend to synthesize a similar trinuclear assembly using the newly synthesized ligand. We tried to replace the Cu(II) with the Co(III) metal ion. Our choice of metal ion is such that the Co(III) complexes are likely to be diamagnetic such that we can use ^{1}H NMR spectroscopy to understand the interactions in the solution,[12] and we also plan to replace the central metal K^{+} ion with metal ions of different charges and sizes[13] and compare it with the previously synthesized complexes.[11] The attempt to synthesize the assembly as proposed in Figure **3** was carried out by changing the -R group and Cu(II) to Co(III). The resultant architecture leads to a 2D polymeric chain with inert Co(III) bis complex as the monomeric units (Figure 4).

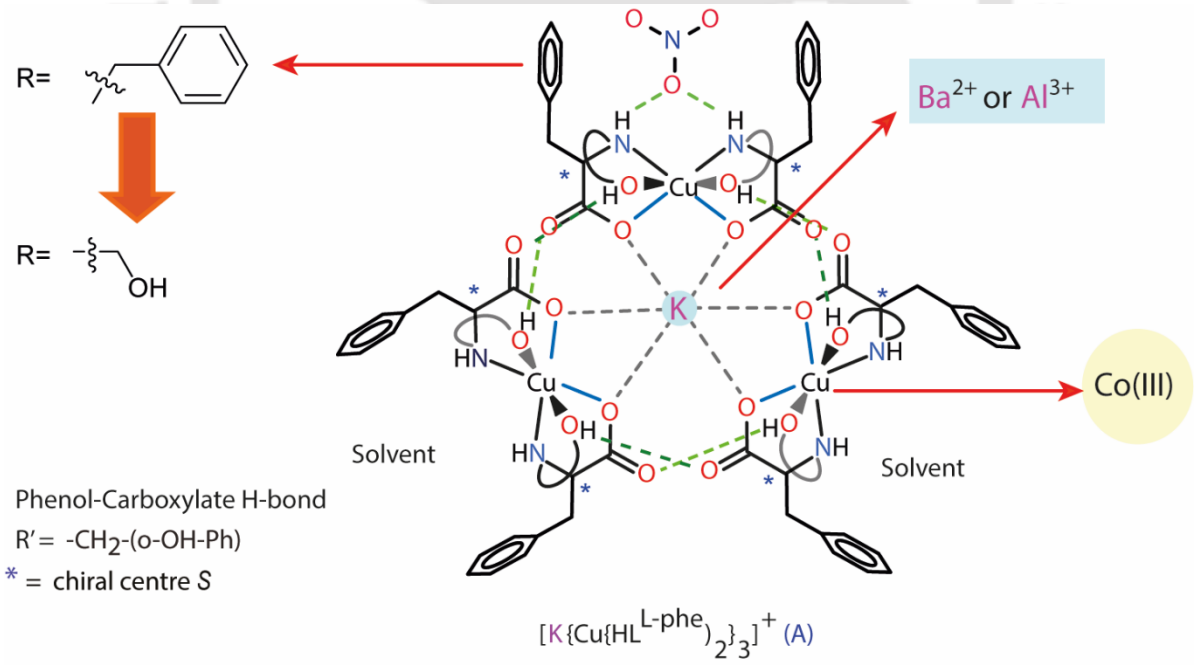

Figure 3. Sketch model for the proposed cyclic trinuclear

The ^{1}H NMR of the assembly was sharp and well resolved, and it was used in the characterization of the assemblies by changing K^{+} to cations of different sizes and charges.

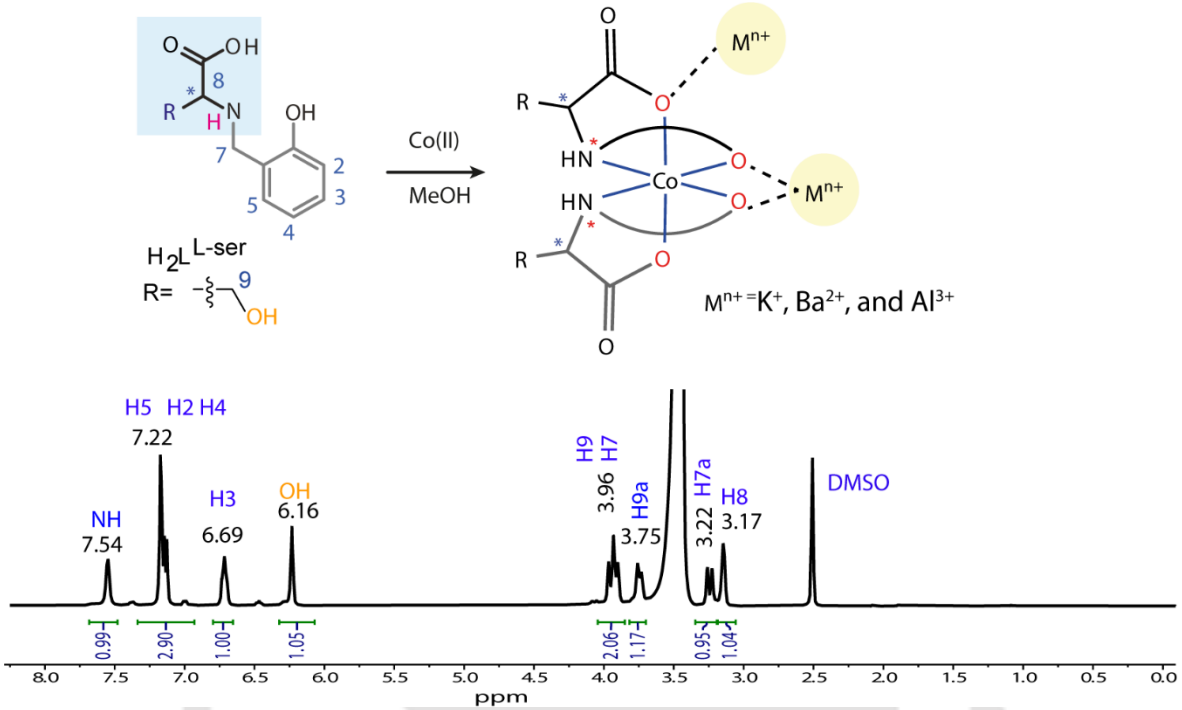

Figure 4. Sketch model of assembly formation with ^{1}H NMR spectra of one of the assemblies [Co(III), Ba^{2+}].

Chapter IV

Water-soluble chiral coordination polymers of Li^{+}, Na^{+}, K^{+}, and Ba^{2+} with an anionic Fe(III) complex of L-threonine derivative and significant red shift of visible spectra with Al^{3+} salt

In this chapter, we used a two-part network formation. An iron(III) chiral complex of L-threonine ligand, interconnected with alkali or alkaline earth metal cations. Depending on the cations used, the resulting networks are either linear, two-dimensional or three-dimensional (Figure 5). One has the solvent-accessible space occupied with a hydrated chloride. Water-soluble coordination polymers are rare, and few that are reported can't be recrystallized back to the original network.[14] Some are large water-soluble cages, not infinite chain networks.[15]

Here, we choose to work with Fe(III) and L-threonine-based ligand to change the shape of the complex and make it anionic to facilitate the binding of alkali or alkaline earth ions as countercations (Figure 5). We also hoped that the alcoholic side arm of L-threonine would increase the solubility of the complexes.

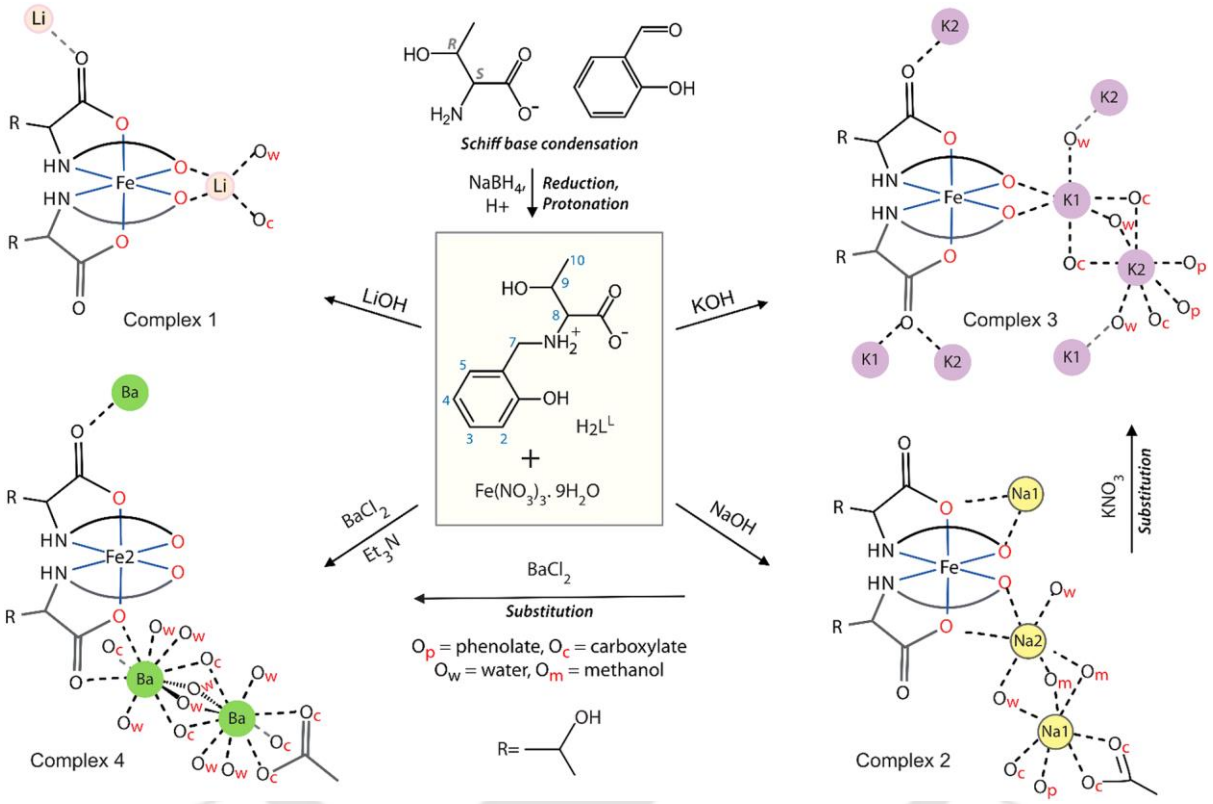

Figure 5. Syntheses of the complexes

[14] B. Liang, B. Li, Z. Li and B. Chen, Chem. Eur. J., 2021, **27**, 12940–12952.

[15] P. Mal, D. Schultz, K. Beyeh, K. Rissanen and J. R. Nitschke, *Angew. Chem. Int. Ed.*, 2008, **47**, 8133–8133.

[16] Y. Suzuki, I. Mizuno, Y. Tabei, Y. Fujioka, K. Shinozaki, T. Sugaya and K. Ishihara, *Inorg. Chem*., 2019, **58**, 9663–9671

We have not come across any water-soluble recrystallizable chiral coordination polymers. A few of the significant results are:

1. All are water-soluble chiral coordination polymers.
2. The structure before and after recrystallization are identical.
3. Except for lithium, all others (Na^+, K^+ and Ba^{2+}) form a bridged bimetal structure which connects the iron(III) complexes.
4. Cations are exchangeable: Ba^{2+} and K^+ networks can be formed from the Na^+ network by adding the salt of Ba^{2+} or K^+.
5. The addition of Al^{3+} salt causes a significant shift in colour.

The visible spectra of the **4** [Fe(III), Ba^{2+}] in Methanol or water showed ~10 nm shift of the charge transfer bands from **3** [Fe(III), K^+]. However, the addition of Al^{3+} salts showed a significant colour shift. Further investigation confirmed that colour shift is due to partial protonation of the complex with proton generated from salt hydrolysis. Most reports on visual aluminium detection consider aluminium's binding as the shift's source.[16] Our results show that protonation due to hydrolysis can skew the observation.

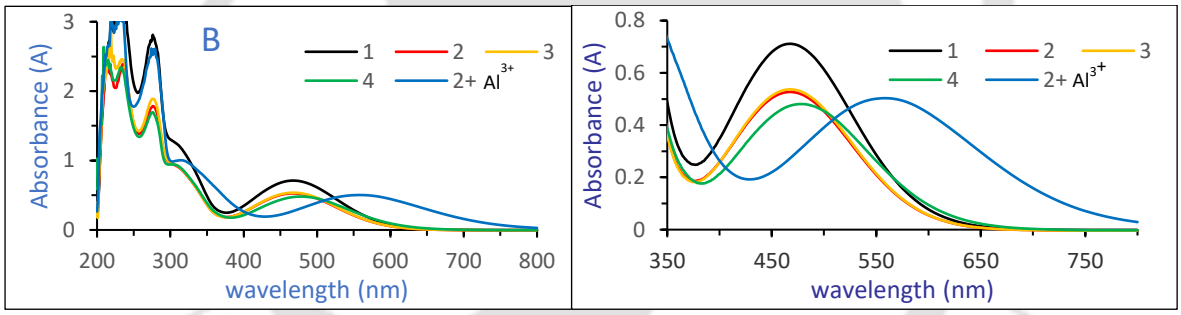

Figure 6. UV-visible spectra of the complexes in Water.

1=[Fe(III), Li^+], **2**=[Fe(III), Na^+], **3**=[Fe(III), K^+], **4**=[Fe(III), Ba^{2+}]

[17] G. Kumar, A. P. Singh and R. Gupta, *Eur. J. Inorg. Chem.*, 2010, 5103–5112.
[18] M. Zhao, H.-B. Wang, L.-N. Ji and Z.-W. Mao, *Chem. Soc. Rev.*, 2013, **42**, 8360.

Chapter V

Stepwise synthesis of a rigid linear trinuclear [Co^{3+}, M^{2+}, Co^{3+}] chiral complex with a labile M^{2+} site at the centre

In this chapter, using the same L-threonine ligand, we synthesized the Co(III) complex, the Fe(III) analogue. Our choice of metal ion is such that the Co(III) complexes are likely to be diamagnetic, so we can use ^{1}H NMR spectroscopy to understand the interactions in the solution. Like its Fe(III) analogue, it forms a polymeric chain when reacted with alkali metal ions. However, by replacing the alkali metal ions with transition metal ions, we obtained the [Co^{3+}– M^{2+}– Co^{3+}] type of linear heterobimetallic complex (Figure 7).[17] The resultant architecture where a Zn(II) or Cu(II) bound water surrounded by an H-bond capable chiral environment is reminiscent of the active site of hydrolytic enzymes.[18]

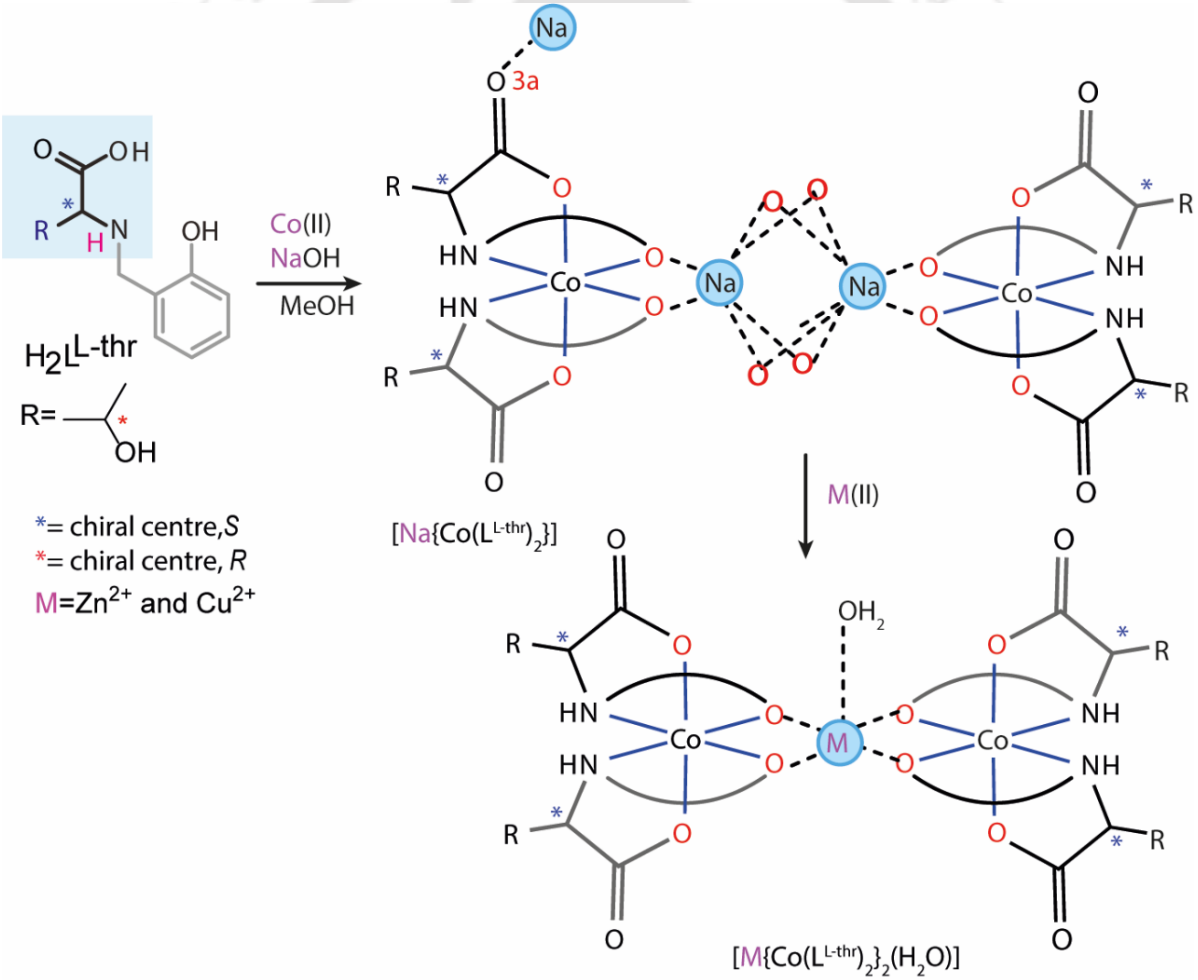

Figure 7. Syntheses of the complexes.

The ^{1}H NMR spectra of all the complexes ([Co(III), M^{n+}]) were sharp and well resolved. We notice the aromatic protons shift downfield as we move from Na^+ to Zn^{2+} (Figure 8).

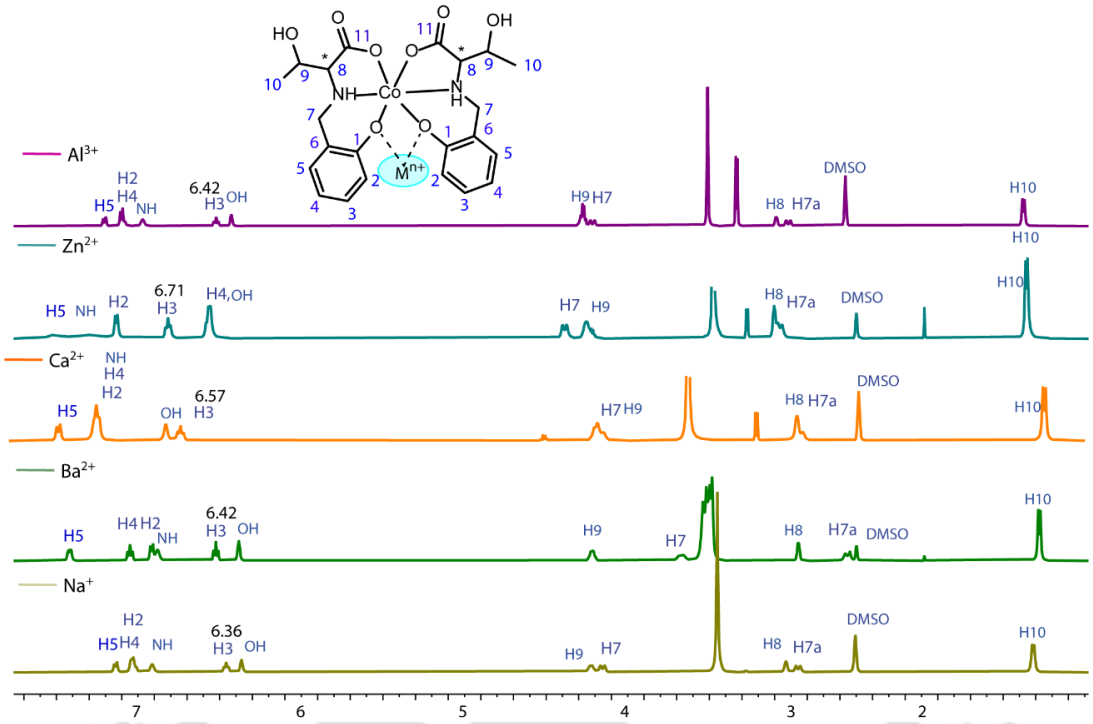

Figure 8. Combine ^{1}H NMR spectra of the complexes.

Table 1. polarising power of the cation data.

M^{n+}	charge	Ionic size(Å)	Charge/ionic size	^{1}H NMR Peak position of H3
Na^{+}	+1	1.02	0.98	6.36
Ba^{2+}	+2	1.35	1.48	6.42
Ca^{2+}	+2	1.06	1.88	6.57
Zn^{2+}	+2	0.74	2.7	6.71
Al^{3+}	+3	0.54	5.6	6.42

To quantify the magnitude of this downfield shift, we used the concept of the charge/ionic radius ratio of the secondary cation, also known as the polarising power of the cation. We calculate the charge/ionic size ratio value of the secondary cations of the complexes (Table 1) and plot the graph against the downfield shift of the aromatic phenol proton H3 (the H3 peak is sharp and does not overlap in all the complexes spectra). We obtained a linear graph (Figure 9) suggesting that the downfield shift of the aromatic phenol protons is directly proportional to the polarising power of the secondary cation. The protons of [Co(III), Al^{3+}] do not shift as predicted using the concept of cation polarising power. This is evidence that Al3+ is not binding to the Co(III) complex, supporting the finding of UV-visible in Chapter 4. The UV-visible spectra of the complexes show that as we move from Na^{+} to $Al^{3+,}$ the d-d transition band moves towards the higher energy (Figure 9B). Therefore, we employed an interesting way to sense and detect spectroscopically silent metal ions using 1H NMR and UV techniques in the visible region.

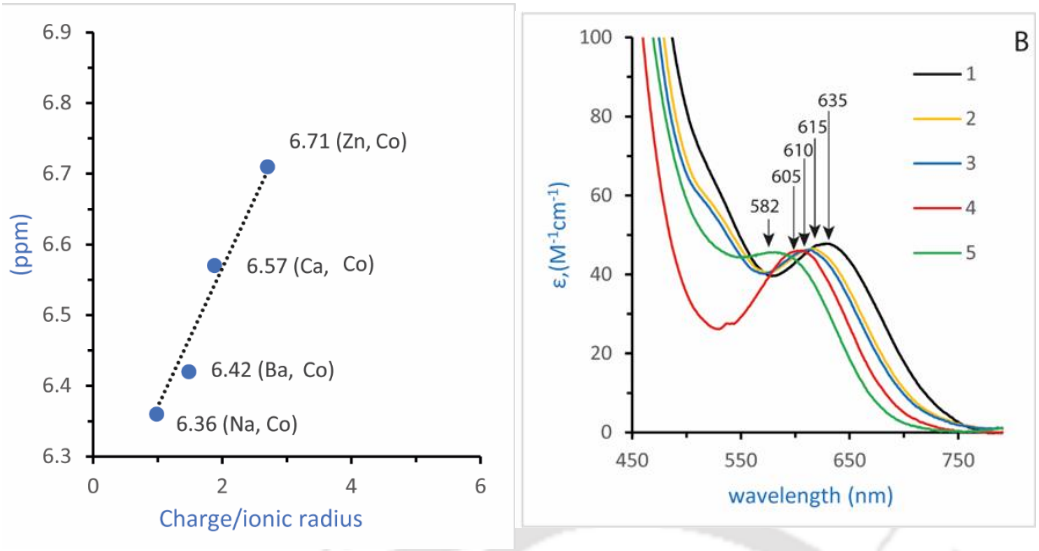

Fig 9. The plot of H3 peak position vs. charge/ionic. (B)UV-visible spectra of the complexes in MeOH (1=Na^{+}, 2=Ba^{2+}, 3=Ca^{2+}, 4=Zn^{2+}, 5=Cu^{2+}, and 6=Al^{3+}.

Conclusions

In this thesis work, we synthesized the hetero-bimetallic cyclic trinuclear assembly using the Cu(II) bis complex as a monomer and successfully disassembled the assembly. We effectively convert the *trans*-oriented Cu(II) monomer to the *cis*-oriented Cu(II) monomer. We attempt to modify the cyclic trinuclear by changing the central metal ion with different cations. We change the metal ion Cu(II) to Fe (III) and amino acid side-arm to execute the process. We obtained the Fe(III) bis complex with a different motif from the Cu(II) version. The Fe(III) bis complex is anionic, and depending on the cation charges and sizes used, one can obtain an assembly or polymeric chain with different dimensionalities. All the polymeric chains obtained are water-soluble. We have not come across any reported water-soluble chiral coordination polymer thus far. The work points out the problems in using UV-visible and fluorescence as a sensing tool for Al^{3+}.[16] As titration of the polymers with acid indicates, the hydrolysis of the salt and acid protonation is also possible. We also successfully synthesized the Co(III) complex, the Fe(III) analogue. The ^{1}H NMR of all the assemblies are sharp and well resolved, indicative of inert diamagnetic assemblies. We used transition metal ions Cu(II) and Zn(II) as secondary cations to synthesize hetero-bimetallic complexes. The resulting architecture where the Zn(II) or Cu(II) bound with water molecules surrounded by the hydrophilic environment is a reminiscence of a hydrolytic enzyme.[18]

Contents

I. Statement i

II. Certificate ii

III. Acknowledgments iii

IV. Abstract v

V. Contents xv

VI. Chapter I – Introduction 1

1.1 Introduction 1

1.2. Water-soluble Metal-Organic Complexes (MOCs) 2

1.3. Chiral Metal-Organic Complexes 4

1.4. Heterobimetallic complexes 5

1.5. Metal-organic complex of reduced Schiff base ligand 7

1.6. Conclusion from the literature survey and the objective of the thesis 9

1.7. References 11

VII. Chapter II - Self-assembly-triggered *trans*-to-*cis* conversion of mononuclear Cu(II) via cyclic chiral tri-nuclear assembly

2.1. Introduction 16

2.2. Experimental section 17

2.2.1. Materials and Methods 17

2.3. Synthesis and Characterization 17

2.3.1. Synthesis of $H_2L^{L\text{-phe}}$ 18

2.3.2. Synthesis of Et_4NSCN 18

2.3.3. Synthesis of $[Cu(HL^{L\text{-phe}})_2]$ (**1**) 19

2.3.4. Synthesis of $Et_4N[Cu(HL^{L\text{-phe}})_2(SCN)]$ (**2**) 19

2.3.5. Syntheses of $[K\{Cu(HL^{L\text{-phe}})_2\}_3]NO_3$ (**A**) 19

2.3.6. Synthesis of $[Cu(HL^{L\text{-phe}})_2]$ (**3**) 20

2.4. X-ray Crystallography 22

2.5. Result and discussion 23

2.6. Disassembly of assembly **A** using [18] crown-6 29

2.7. Absorption spectroscopy 32

2.8. Solid-state UV-visible spectra 33

2.9. Conclusion 36

2.10. References 37

VIII. Chapter III - Redesigning of cyclic chiral trinuclear by changing amino acid sidearm, using inert Co(III) complex, and cation of different sizes and charges

3.1. Introduction 41
3.2. Experimental section 42
3.2.1. Materials and Methods 42
3.3. Synthesis and Characterization 42
3.3.1. Synthesis of $H_2L^{L\text{-ser}}$ 43
3.3.2. Synthesis of $[K(Co(L^{L\text{-ser}})_2]$ (**1**) 43
3.3.3. Synthesis of $[Ba\{(Co(L^{L\text{-ser}})_2\}_2]$ (**2**) 43
3.4. X-ray Crystallography 44
3.5. Result and discussion 45
3.6. ESI-Mass spectrometry of the complexes 47
3.7. NMR spectroscopy 48
3.8. UV-visible spectroscopy 53
3.9. Conclusion 54
3.10. References 55

IX. Chapter IV – Water-soluble chiral coordination polymers of Li^+, Na^+, K^+, and Ba^{2+} with an anionic Fe(III) complex of L-threonine derivative and significant red shift of visible spectra with Al^{3+} salt

4.1. Introduction 56
4.2. Experimental section 57
4.2.1. Materials and Methods 58
4.3. Synthesis and Characterization 58
4.3.1. Synthesis of $H_2L^{L\text{-thr}}$ 58
4.3.2. Synthesis of $[Li\{Fe(L^{L\text{-thr}})_2\}(H_2O)]\bullet H_2O$ (**1**) 59
4.3.3. Synthesis of $[Na_2\{Fe(L^{L\text{-thr}})_2\}_2(MeOH)_2(H_2O)_2]\bullet 3MeOH$ (**2**) 59
4.3.4. Synthesis of $[K_2\{Fe(L^{L\text{-thr}})_2\}_2(H_2O)_2]\bullet MeOH$ (**3**) 59
4.3.5. Syntheses of $[Ba_2\{Fe(L^{L\text{-thr}})_2\}_3(H_2O)_{10}]Cl\bullet MeOH\bullet 3H_2O$ (**4**) 60
4.4. X-ray Crystallography 61
4.5. Result and discussion 62

4.6. Charge transfer transitions in the solution and ESI-Mass 67
4.7. The shift in charge transfer band with Al^{3+} salt 69
4.8. Conclusion 71
4.9. References 73

X. Chapter V – Stepwise synthesis of a rigid linear hetero-bimetallic [Co^{3+}, M^{2+}, Co^{3+}] chiral complex with a labile M^{2+} site at the centre

5.1. Introduction 77
5.2. Experimental section 78
5.2.1. Materials and Methods 78
5.3. Synthesis and Characterization 79
5.3.1. Synthesis of $H_2L^{L\text{-}thr}$ 79
5.3.2. Synthesis of $[Na\{Co(L^{L\text{-}thr})_2\}(H_2O)_2]$ (**1**) 79
5.3.3. Synthesis of $[Ba\{Co(L^{L\text{-}thr})_2\}_2]$ (**2**) 79
5.3.4. Synthesis of $[Ca\{Co(L^{L\text{-}thr})_2\}_2]$ (**3**) 80
5.3.5. $[Zn\{Co(L^{L\text{-}thr})_2\}_2(H_2O)]$ (**4**) 80
5.3.6. $[Cu\{Co(L^{L\text{-}thr})_2\}_2(H_2O)]$ (**5**) 80
5.3.7. $[Co(HL^{L\text{-}thr})_2](NO_3)$ (**6**) 81
5.4. X-ray Crystallography 81
5.5. Result and discussion 82
5.6. NMR spectroscopy 88
5.7. ESI-Mass spectrometry 93
5.8. UV-visible spectroscopy 95
5.9. Conclusion 98
5.10. References 99

X11. Findings of the thesis 102

X111. List of publications 104

भारतीय प्रौद्योगिकी संस्थान गुवाहाटी
Indian Institute of Technology Guwahati

Chapter I

1.1. Introduction

Alkali metal ions are among the most abundant metal ions on earth's crust and in the human body.[1] Their biological functions are well-known and well-studied. However, mimicking their binding in biology proved to be challenging. The limitation stems from their lack of binding to ligands through conventional coordination bonds. Their bonding to a hard ligand such as carboxylate, ether, or other oxygen donors is predominantly ionic and labile. These led to the development of organic crown ethers and cryptands[2–5], which helped us understand their binding in biology and generated many other applications. The synthesis of metallacrowns, metal complexes that bind alkali ions similarly to crown ethers, showed that incorporating transition metal complexes has benefits.[6,7] Having transition metals along with alkali ions gives materials extra functions that organic crown ethers can't perform.[8] Metallacrowns have demonstrated functions as diverse as the stabilization of unstable molecules, single-molecule magnets, and anion recognition agents, to name a few.[9–12] Alkali metal ions have also been incorporated within the metal-organic framework (MOF) for biomedical applications, used as a template to synthesize interlocked molecules and in supramolecular metal-organic complexes (MOCs).[13–16] Crystalline MOFs, with their well-defined porous structures, can store smaller molecules, act as catalysts, and even function as capacitors.[17,18] MOCs are distinctly different from MOFs. MOFs are coordination polymers and thus insoluble in most solvents by design.[19–22] As MOC are the assembly of molecules bound together through noncovalent or weaker bonds, they can be soluble, retaining their structure in solution. Many MOCs have been reported with porous structures retained in solution.[23–27] The research community has witnessed the prominent growth of chiral Metal organic complexes (CMOCs) at the forefront of chiral solid-state materials and chiral technology over the past two decades The realm of CMOCs for enantioselective applications is still under fast development, and several reviews have covered the targeted synthesis of CMOCs for asymmetric heterogeneous catalysis and separation, including asymmetric catalysis, enantioselective separation, enantioselective recognition, sensing, and circularly polarized luminescence (CPL), second-order nonlinear optics (NLO), and drug delivery.[28–31]

1.2.Water-soluble Metal-Organic Complexes (MOCs)

The search for industrial processes and the need for reduced environmental impact has prompted research on nonconventional solvents. Among the alternatives, water is the green

solvent par excellence, as it is nontoxic, safe and readily available at a very affortable cost. Transition-metal complexes that are water-soluble is a growing interest for catalytic applications, owing to their simple product separation, and pH-dependent selectivity in aqueous media. Moreover, the bioavailability and bioactivity of coordination compounds are often dependent on their hydrosolubility. Fujita *et al* have worked on the square planar geometry of palladium and pyridine base bridging ligands for the construction of highly symmetric metal-organic complexes and cages. The positive charge of the metal centre makes the complex highly water soluble.[32] The hydrophobic channel provided by the ligand is capable of trapping and binding the guest molecules.[33] In recent years, Various water-soluble MOCs have been synthesized by self-assembling the water-soluble Pd(II) complex with different pyridine-based ligands (Fig 1.1).[34–36]

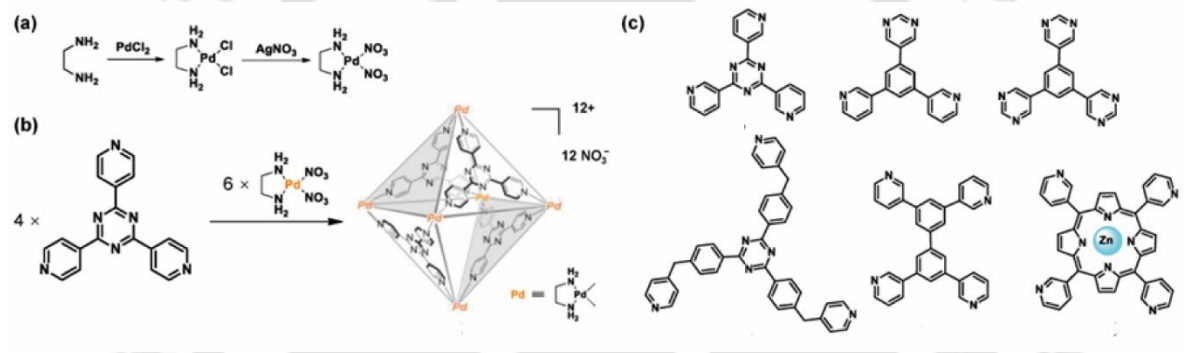

Fig 1.1. synthesis of (**a**) [cis-(en)Pd(NO_3)$_2$]; (**b**) water-soluble MOC (**c**) different ligands used to synthesize water-soluble MOC.

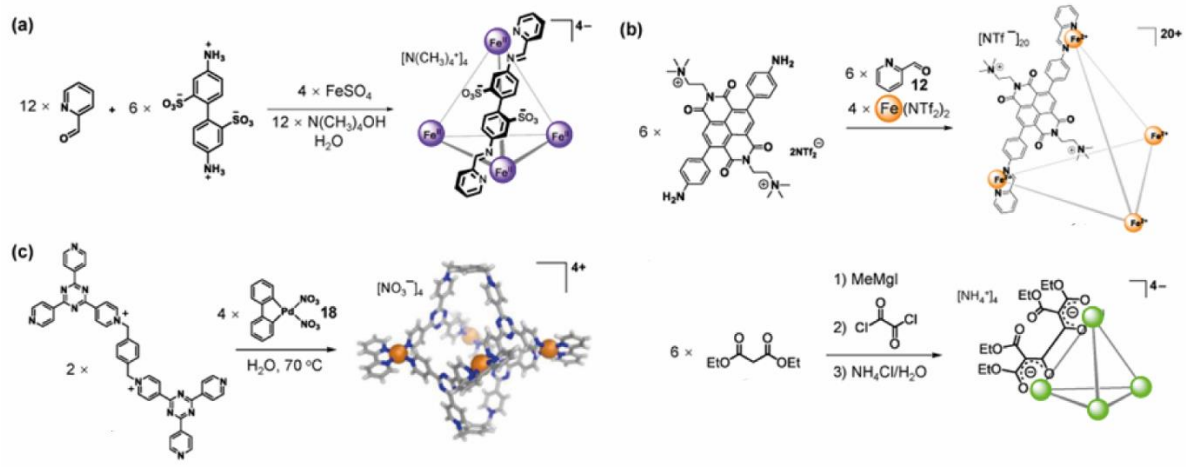

Fig 1.2. Reported water-soluble MOC assembled from ligands with (**a**) sulfonate, (**b**) ammonium, and (**c**) pyridinium and (**d**) assembled from ligands after dehydrogenation under alkali conditions

Nitschke group have reported a new type of water-soluble tetrahedral, which was constructed by a charged ligand through sub-component self-assembly in water (Fig 1.2). The complex has high hydrophilicity, mainly because highly hydrophilic sulfonate groups extend out of the cavity and are arranged symmetrically through the crystal structure analysis. It is noted that the hydrophobic internal cavity (141 $Å^3$) can encapsulate a wide range of guests.[37–39] This method has been shown to be helpful for the construction of water-soluble cages with charged properties.[37]

There are many alkali and alkaline earth metal ions induced MOCs and coordination polymers, with different sizes and shapes.[40–43] However, very few of them are water-soluble.[44–46]

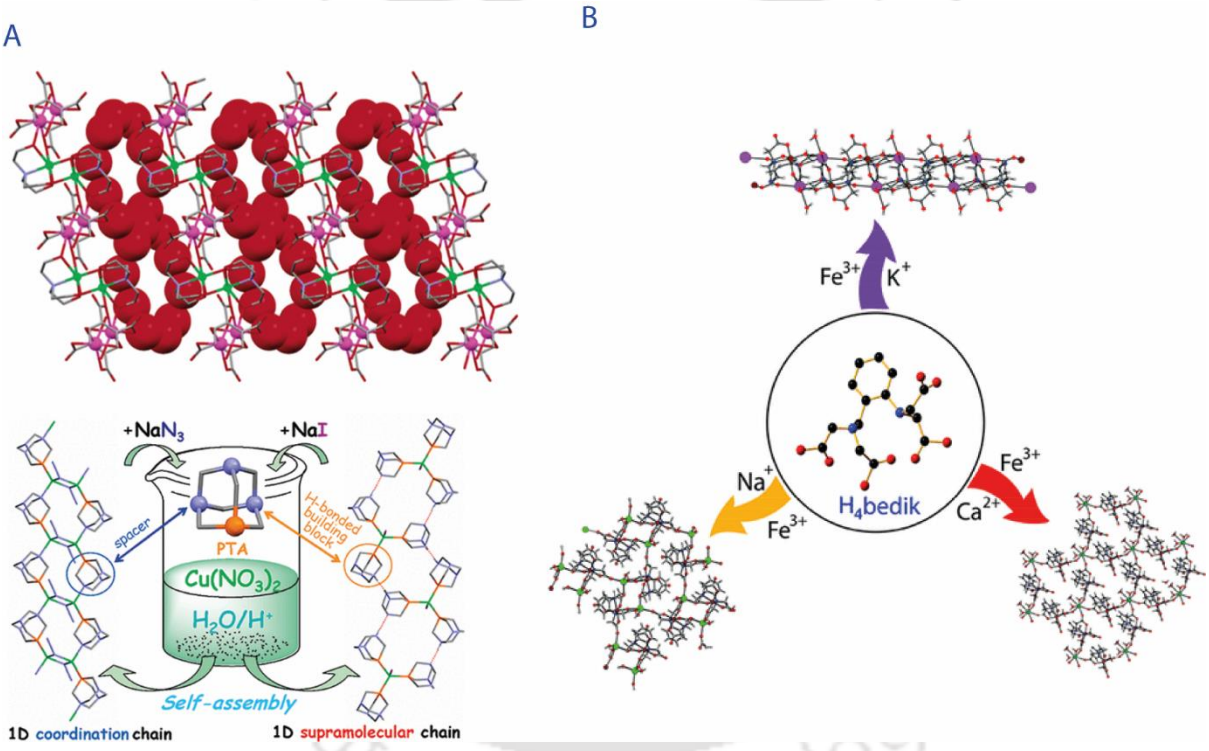

Fig 1.3. (A) metal−organic chains with intercalated guests of infinite decameric water clusters represented by the space-filling model. (B) ORTEP presentation of the complex coordination environment of K

A few examples of cations-induced water-soluble coordination polymers and their interaction with water molecules are given in Figure 1.3.

1.3. Chiral Metal-Organic Complexes

We live in a chiral world. Nature exhibits a remarkable degree of specificity in the chiral recognition of biomolecules, leading to the mirror image arrangements of the two forms eliciting quite different biological responses.[47] While most of the reported MOC materials are achiral.[48–50] Many biological macromolecules or supramolecular systems (such as nucleotides, carbohydrates, peptides, and proteins) are chiral.[51] Chirality is crucial in various physiological processes through stereospecific interactions.[52] Therefore, the development of chiral MOCs is of great importance and interest in diverse fields of science and technology. Y. Chui and workers worked on developing chiral MOCs and understanding their chirality expression at the supramolecular level (Fig 1.3). Their design principle mainly exploited the "three-point interaction" rule. The selector can discriminate between the two enantiomers if there are at least three points of interaction between the chiral selector and one or both of the enatiomers. Additionally, complementary size and shape between host and guest are crucial to regulating enantiomer-to-host interactions. Considering these factors might enable an excellent opportunity to acquire novel chiral materials with outstanding chiral recognition and separation performance.

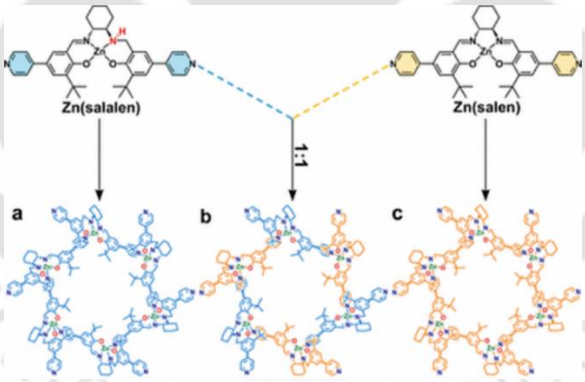

Figure 1.4. Self-assembly and crystal structures of chiral NH-controlled metallacycles: (a) $Zn_3(Salalen)_6$; (b) $Zn_3(Salalen)_3(salen)_3$; (c) $Zn_3(Salen)_6$

In this article[53] (Fig 1.4) they report a strategy for the assembly of three chiral NH-controlled supramolecular metallacycles, Zn6(salalen)6, Zn6(salalen)3(salen)3, and Zn6(salen)6, and demonstrate their use as fluorescent chiral receptors for α-hydroxycarboxylic acids, amino acids, amines, and selected small pharmaceutical molecules, with high binding affinity and enantioselectivity. They directly observe the key role of chiral NH functionalities in the metallacycles that lead to monitoring the chiral recognition and discrimination of biomolecules.

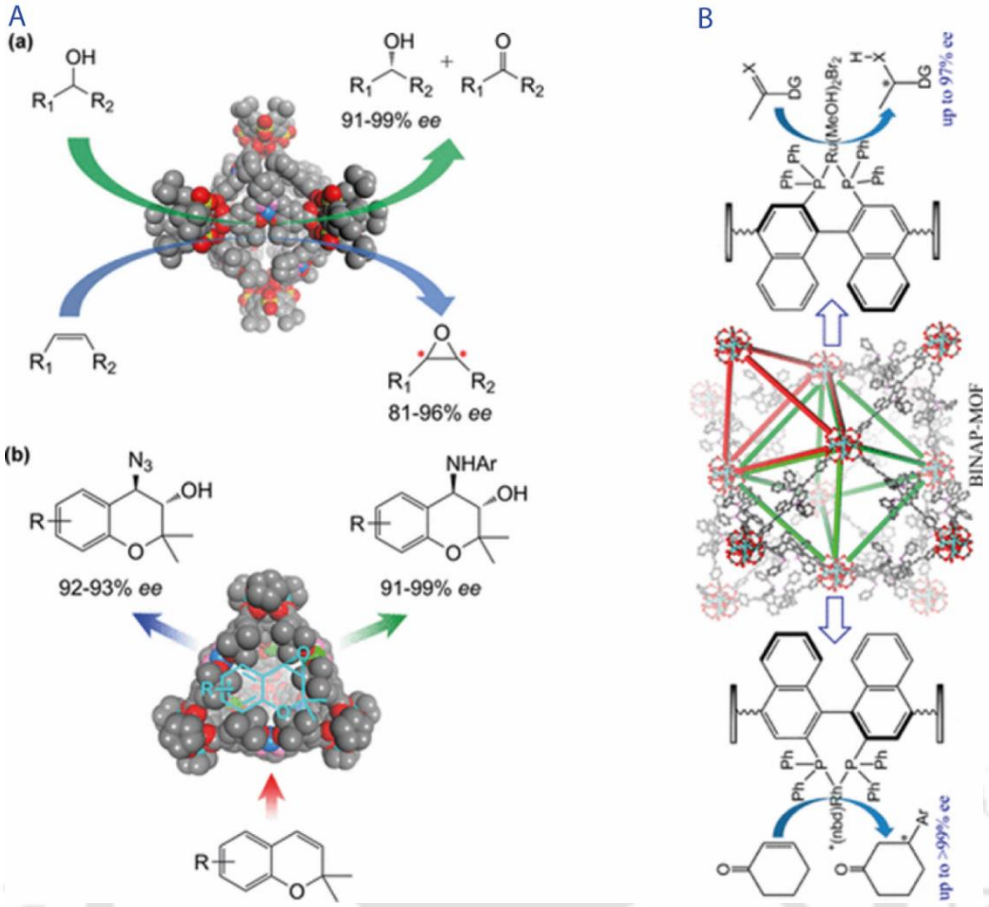

Figure 1.5. (A) (a) epoxidation of olefins. (b) Sequential asymmetric epoxidation/ring-opening reactions by using the chiral cage. (B) BINAP-based chiral cage and its postsynthetic metalation for catalytic applications.

Y. Chui *et al* have also worked on the oxidative kinetic resolution of racemic secondary alcohols and epoxidation of olefins by using a chiral cage and sequential asymmetric epoxidation/ring-opening reactions by using a cage (Fig 1.5A).[54–56] Lin *et al* also worked on phosphine-based metal-organic complexes for broad-scope asymmetric catalysis. Their Rh-functionalized MOF is highly enantioselective (up to >99% ee) and 3 times as active as the homogeneous control (Fig 1.5B).[57,58]

1.4. Heterobimetallic complexes

Blackmore *et al* focus on metal complexes of the ligands featuring a platform with a hydrogen bond donating or an accepting environment with a secondary coordination sphere inorder to pursue metalation. They synthesized heterobimetallic complexes and used UV-visible and electrochemistry to characterize and sense cations (Fig 1.6).[59,60]

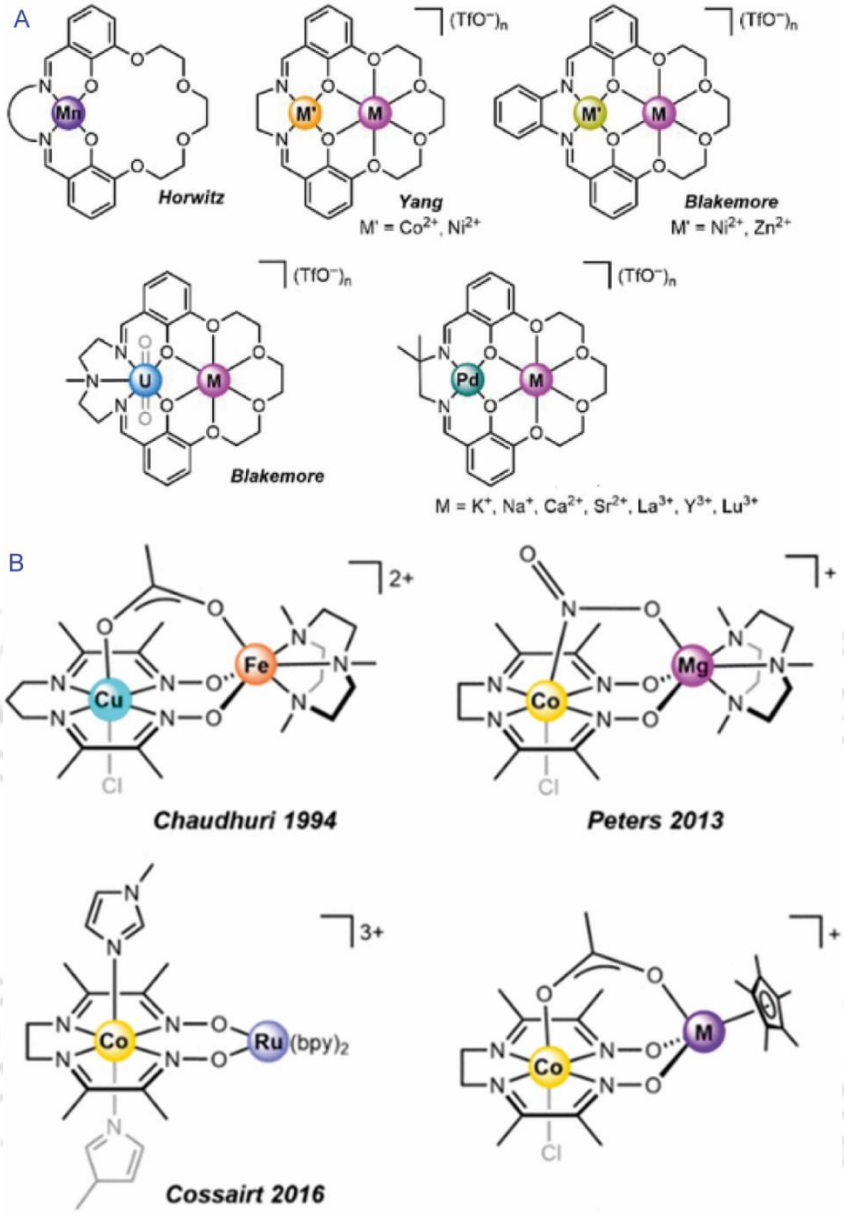

Fig 1.5. Heterobimetallic Complexes based on Diimine–Dioximato Ligands (A) and selected heterobimetallic complexes of Reinhoudt-type heteroditopic ligand frameworks (B)

Borovik and co-workers are also working on heterobimetallic complexes where they study the effects of redox-inactive metal ions on the activation of dioxygen [61]. Their resulting structure has relevance to the oxygen-evolving complex within photosystem II (Fig 1.6A). They also synthesized heterobimetallic complexes containing CoII/III and CaI ions[62], where they studied the assembly and properties of complexes' interaction with aqua and hydroxo ligands (Fig 1.6B).

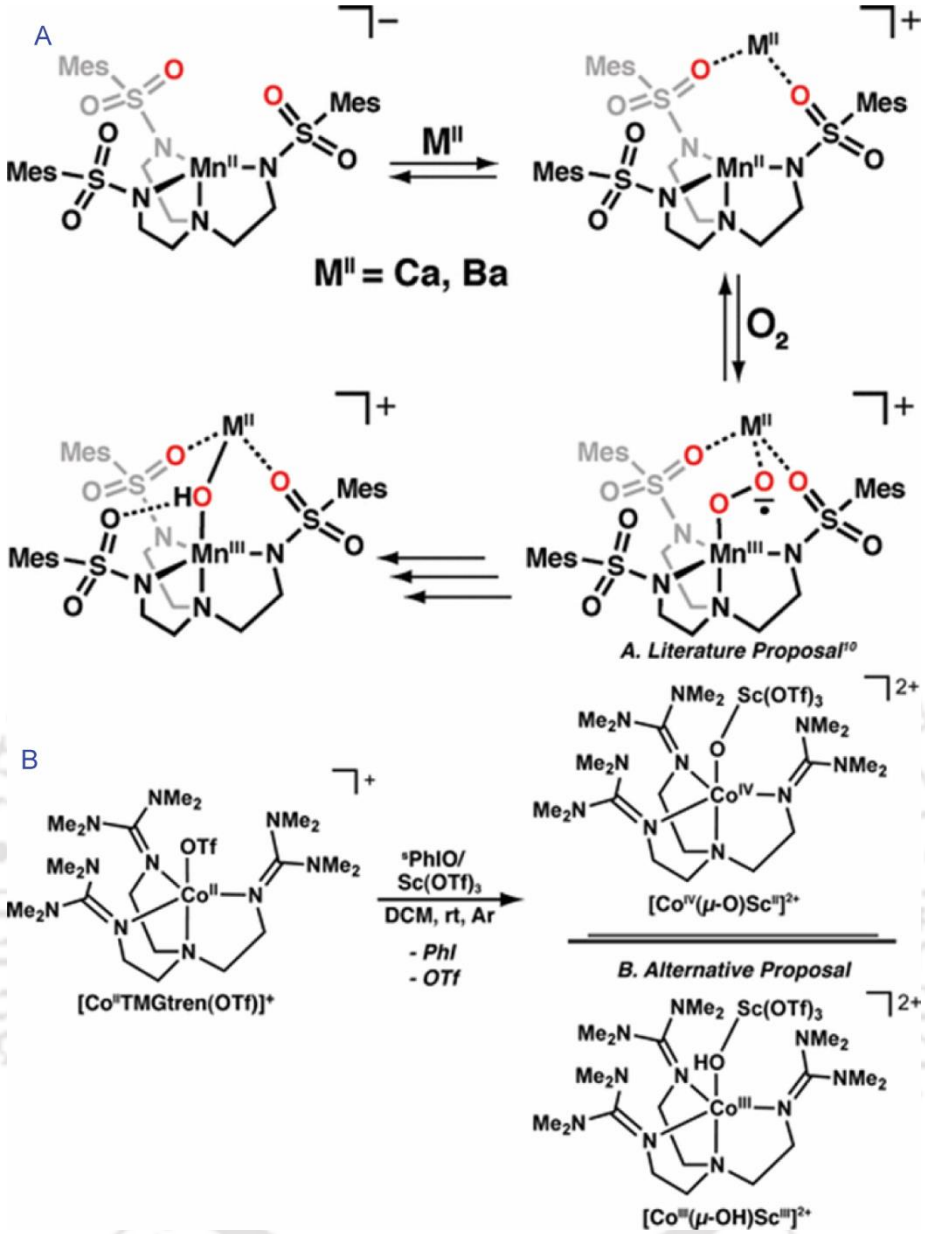

Fig 1.6. Proposed role of the redox-inactive metal ions in the activation of dioxygen (A) and Comparison of Possible Heterobimetallic Complex (B)

1.5. Metal-organic complex of reduced Schiff base ligands

Earlier, our group reported synthesizing and characterizing an octahedral Cu(II) complex with L-histidine-derived reduced Schiff base ligand, which traps four pyridines inside the capsular cavity (Fig 1.7A).[63] It is one example of a complex having chirality, H-bonding and labile metal centres within the same molecules.

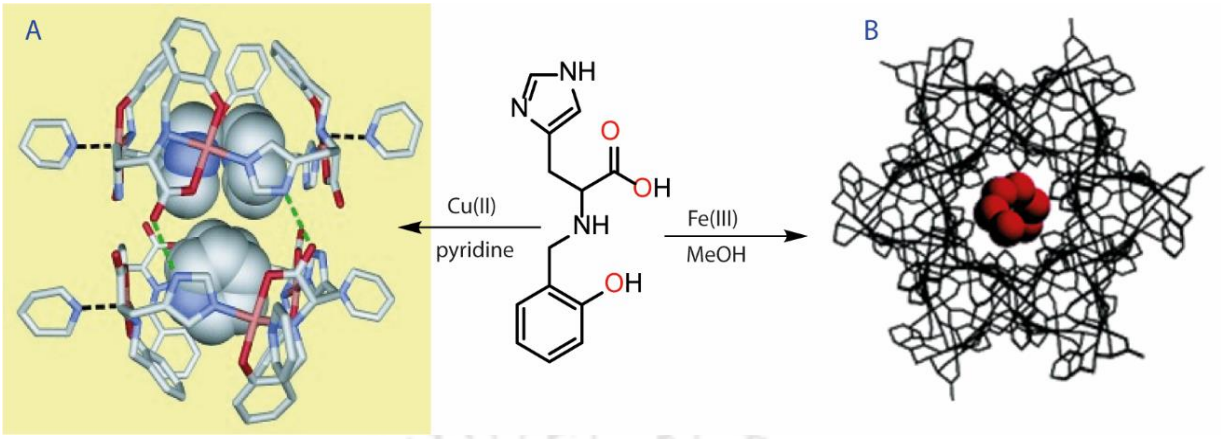

Scheme 1.7. Formation of octanuclear Cu(II) (A) and hydroxo bridge water removable channel of Fe(III) (B)

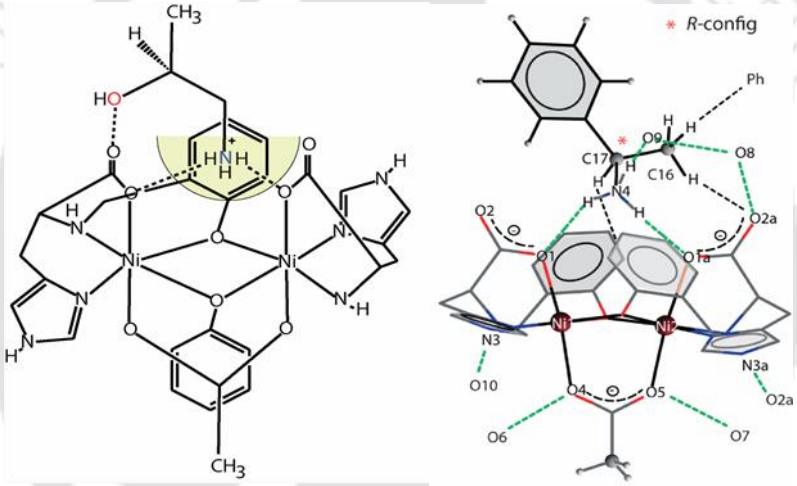

Fig 1.8. Dinuclear nickel complex as a host to recognise chiral guest molecules.

Using the same ligand, our group has also reported the enantiopure hydroxo-bridged binuclear iron(III) complex with empty one-dimensional helical channels, which can trap water molecules and by removing water molecules, we can insert iodine inside the channel (Fig 1.7B).[64] Using the same ligand our group also reported the chiral recognition by synthesizing dinuclear Nickle bridge complex as a host to recognise guest molecules such as chiral amines and chiral amino alcohol using three-point recognition method (Fig.1.8).[65,66]

Our group (M. Dubey, M.Ray) also reported the formation of a trinuclear assembly of L-leucine-derived ligand (Fig 1.9)[69].

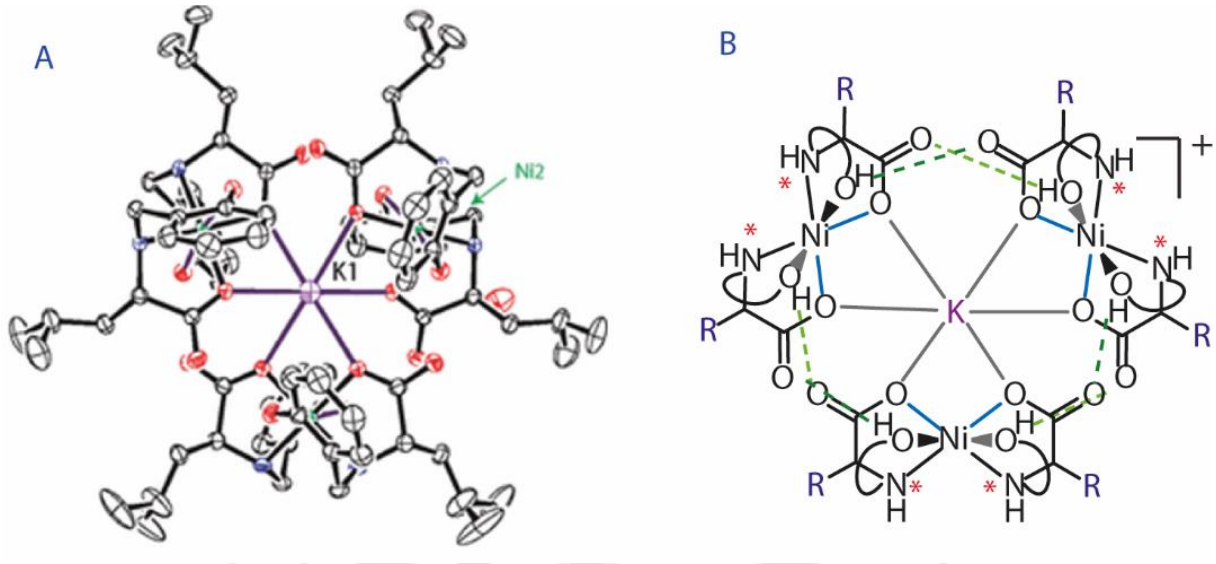

Fig 1.9. L-leucine derived ligand Ni(II) complex, trinuclear assembly around K^+

1.6. Conclusion from the literature survey and objective of the thesis

The use of a coordination complex as a ligand to bind another metal gives rise to multiple possibilities ranging from coordination polymer to clusters. Having two different metals bound through the same ligand adds numerous possibilities of magnetic and redox properties, in addition to architectural aspects. The literature survey revealed wide research interest in water-soluble coordination polymers, multinuclear assemblies, and a few examples where chirality is inducted in the clusters (Sections 1.2 to 1.4). Many of these examples used the alkali metal ion or Zn(II) as the second metal ion. Binding of alkali, alkaline earth, and Zn(II) are relevant to biology. However, binding alkali and alkaline earth metal ions to another complex and structurally characterizing the resultant complex is somewhat challenging. The binding is labile and predominantly ionic. Unlike transition metal ions, it hardly prefers a fixed geometry and usually prefers binding to oxygen donors. These factors lead to multiple configurations in solution, inhibiting the formation of single crystals. Crystal formation is also affected by the choice of solvent and reaction conditions. A literature survey also showed that the organic ligands used varied widely.

Our group was interested in synthesizing assemblies of chiral complexes to use as hosts for chiral recognition (Section 1.5). A few years back, they reported a trinuclear assembly with a central Na^+ or K^+ ion with an L-leucine amino acid-derived ligand. Architecturally it was interesting but the report was limited to L-leucine and not much work was done afterwards.[41,42]

Based on these facts, we decided to work on

1. Two different ligands, one with a hydrophilic arm (L-threonine) and the other with an aromatic arm (L-phenylalanine).

2. The similar assembly as L-leucine derivative and attempt to disassemble and reassemble the same.

3. Changing the first metal ion to check if anything other than the trinuclear assembly can be formed.

4. Changing the first metal to a diamagnetic metal and using 1H NMR tools on the resulting assembly to understand their identity in solution.

5. The binding of the resulting complexes with alkali and alkali metal ions of different sizes and charges.

6. Replacing the secondary cation with transition metal ions.

Through these, we hoped to synthesize new assemblies and different coordination polymers. By using two similar chiral ligands and their chiral complexes binding different second metal ions, we hoped to understand interconvertibility between these structures and to have a generalized way to make different architectures. The increase in charge on the metal would make it anionic to facilitate the binding of cations. We also hoped that the alcoholic side arm of L-threonine would increase the solubility of the complexes through H-bonding.

1.7. References

1 A. Sigel, *The alkali metal ions: their role for life*, Springer Berlin Heidelberg, New York, NY, 2015.

2 S. O. Kang, J. M. Llinares, V. W. Day and K. Bowman-James, *Chem. Soc. Rev.*, 2010, **39**, 3980.

3 G. González-Riopedre, M. R. Bermejo, M. I. Fernández-García, A. M. González-Noya, R. Pedrido, M. J. Rodríguez-Doutón and M. Maneiro, *Inorg. Chem.*, 2015, **54**, 2512–2521.

4 D. N. Huh, C. J. Windorff, J. W. Ziller and W. J. Evans, *Chem. Commun.*, 2018, **54**, 10272–10275.

5 E. V. Salerno, C. M. Foley, V. Marzaroli, B. L. Schneider, M. D. Sharin, J. W. Kampf, L. Marchiò, M. Zeller, R. Guillot, T. Mallah, M. Tegoni, V. L. Pecoraro and C. M. Zaleski, *Eur. J. Inorg. Chem.*, 2022, **2022**, e202200439.

6 I. Oral and V. Abetz, *Soft Matter*, 2022, **18**, 934–937.

7 A. J. Ryan, J. W. Ziller and W. J. Evans, *Chem. Sci.*, 2020, **11**, 2006–2014.

8 G. Mezei, C. M. Zaleski and V. L. Pecoraro, *Chem. Rev.*, 2007, **107**, 4933–5003.

9 J. Jankolovits, C. M. Andolina, J. W. Kampf, K. N. Raymond and V. L. Pecoraro, *Angew. Chem. Int. Ed.*, 2011, **50**, 9660–9664.

10 C. M. Zaleski, E. C. Depperman, J. W. Kampf, M. L. Kirk and V. L. Pecoraro, *Inorg. Chem.*, 2006, **45**, 10022–10024.

11 A. J. Stemmler, A. Barwinski, M. J. Baldwin, V. Young and V. L. Pecoraro, *J. Am. Chem. Soc.*, 1996, **118**, 11962–11963.

12 J. Jankolovits, C.-S. Lim, G. Mezei, J. W. Kampf and V. L. Pecoraro, *Inorg. Chem.*, 2012, **51**, 4527–4538.

13 S. Verma and R. Murugavel, *Inorg. Chem.*, 2022, **61**, 6807–6818.

14 S. Burazer, F. Morelle, Y. Filinchuk, R. Černý and J. Popović, *Inorg. Chem.*, 2019, **58**, 6927–6933.

15 Z.-W. Huang, K.-Q. Hu, L. Mei, C.-Z. Wang, Y.-M. Chen, W.-S. Wu, Z.-F. Chai and W.-Q. Shi, *Inorg. Chem.*, 2021, **60**, 651–659.

16 G. Ye, C. Chen, J. Lin, X. Peng, A. Kumar, D. Liu and J. Liu, *Dalton Trans.*, 2021, **50**, 17438–17454.

17 R. Vanaraj, R. Vinodh, T. Periyasamy, S. Madhappan, C. M. Babu, S. P. Asrafali, R. Haldhar, C. Jayprakash Raorane, H. Hwang, H.-J. Kim, M. Yi and S.-C. Kim, *Energy Fuels*, 2022, **36**, 4978–4991.

18 S. Shin, J. W. Gittins, C. J. Balhatchet, A. Walsh and A. C. Forse, *Adv. Funct. Mater.*, 2023, 2308497.

19 M. Liu, L. Zhang and T. Wang, *Chem. Rev.*, 2015, **115**, 7304–7397.

20 S. J. Lee and W. Lin, *Acc. Chem. Res.*, 2008, **41**, 521–537.

21 S. Cho, Y. Kim, S. Lee, H. Cho, J. Park, D. Hwan Hong, K. Kwon, H. Yoo, W. Choe and H. Ri Moon, *Eur. J. Inorg. Chem.*, 2022, **2022**, e202101045.

22 B. Liang, B. Li, Z. Li and B. Chen, *Chem. – Eur. J.*, 2021, **27**, 12940–12952.

23 V. Aggarwal, S. Solanki and B. D. Malhotra, *Chem. Sci.*, 2022, **13**, 8727–8743.

24 D. M. Steinert, S. Ernst, S. K. Henninger and C. Janiak, *Eur. J. Inorg. Chem.*, 2020, **2020**, 4502–4515.

25 P. Anithabanu and V. G. Vaidyanathan, *Int. J. Biol. Macromol.*, 2021, **190**, 56–60.

26 P. Vairaprakash, H. Ueki, K. Tashiro and O. M. Yaghi, *J. Am. Chem. Soc.*, 2011, **133**, 759–761.

27 M. Sánchez-Sánchez, N. Getachew, K. Díaz, M. Díaz-García, Y. Chebude and I. Díaz, *Green Chem.*, 2015, **17**, 1500–1509.

28 L. Ma, C. Abney and W. Lin, *Chem. Soc. Rev.*, 2009, **38**, 1248.

29 B. Chen, L. Wang, F. Zapata, G. Qian and E. B. Lobkovsky, *J. Am. Chem. Soc.*, 2008, **130**, 6718–6719.

30 O. R. Evans and W. Lin, *Acc. Chem. Res.*, 2002, **35**, 511–522.

31 S.-H. Cho, B. Ma, S. T. Nguyen, J. T. Hupp and T. E. Albrecht-Schmitt, *Chem Commun*, 2006, 2563–2565.

32 M. Fujita, S. Nagao and K. Ogura, *J. Am. Chem. Soc.*, 1995, **117**, 1649–1650.

33 M. Fujita, M. Tominaga, A. Hori and B. Therrien, *Acc. Chem. Res.*, 2005, **38**, 369–378.

34 P. Anithabanu and V. G. Vaidyanathan, *Int. J. Biol. Macromol.*, 2021, **190**, 56–60.

35 C. Tian and Q. Sun, *Chem. – Eur. J.*, 2023, **29**, e202300195.

36 E. G. Percástegui, T. K. Ronson and J. R. Nitschke, *Chem. Rev.*, 2020, **120**, 13480–13544.

37 P. Mal, D. Schultz, K. Beyeh, K. Rissanen and J. R. Nitschke, *Angew. Chem. Int. Ed.*, 2008, **47**, 8133–8133.

38 T. K. Ronson, C. Giri, N. Kodiah Beyeh, A. Minkkinen, F. Topić, J. J. Holstein, K. Rissanen and J. R. Nitschke, *Chem. – Eur. J.*, 2013, **19**, 3374–3382.

39 M. M. J. Smulders, S. Zarra and J. R. Nitschke, *J. Am. Chem. Soc.*, 2013, **135**, 7039–7046.

40 B. Masci and P. Thuéry, *CrystEngComm*, 2007, **9**, 582–590.

41 M. Dubey, R. R. Koner and M. Ray, *Inorg. Chem.*, 2009, **48**, 9294–9302.

42 M. Dubey and M. Ray, *CrystEngComm*, 2013, **15**, 9648.

43 J. J. Vittal, X. Wang and J. D. Ranford, *Inorg. Chem.*, 2003, **42**, 3390–3392.

44 Y. Yu. Karabach, A. M. Kirillov, M. F. C. G. Da Silva, M. N. Kopylovich and A. J. L. Pombeiro, *Cryst. Growth Des.*, 2006, **6**, 2200–2203.

45 Ł. Jaremko, A. M. Kirillov, P. Smoleński and A. J. L. Pombeiro, *Cryst. Growth Des.*, 2009, **9**, 3006–3010.

46 B. Phukan, S. Ghorai, K. Deka, P. Deb and C. Mukherjee, *Cryst. Growth Des.*, 2018, **18**, 531–539.

47 J. L. Stymiest, V. Bagutski, R. M. French and V. K. Aggarwal, *Nature*, 2008, **456**, 778–782.

48 W. Wang, Y.-X. Wang and H.-B. Yang, *Chem. Soc. Rev.*, 2016, **45**, 2656–2693.

49 T. R. Cook and P. J. Stang, *Chem. Rev.*, 2015, **115**, 7001–7045.

50 R. Chakrabarty, P. S. Mukherjee and P. J. Stang, *Chem. Rev.*, 2011, **111**, 6810–6918.

51 M. Frenkel-Pinter, M. Samanta, G. Ashkenasy and L. J. Leman, *Chem. Rev.*, 2020, **120**, 4707–4765.

52 J. T. Sczepanski and G. F. Joyce, *Nature*, 2014, **515**, 440–442.

53 J. Dong, C. Tan, K. Zhang, Y. Liu, P. J. Low, J. Jiang and Y. Cui, *J. Am. Chem. Soc.*, 2017, **139**, 1554–1564.

54 J. Dong, Y. Liu and Y. Cui, *Acc. Chem. Res.*, 2021, **54**, 194–206.

55 C. Tan, J. Jiao, Z. Li, Y. Liu, X. Han and Y. Cui, *Angew. Chem. Int. Ed.*, 2018, **57**, 2085–2090.

56 J. Jiao, C. Tan, Z. Li, Y. Liu, X. Han and Y. Cui, *J. Am. Chem. Soc.*, 2018, **140**, 2251–2259.

57 J. M. Falkowski, T. Sawano, T. Zhang, G. Tsun, Y. Chen, J. V. Lockard and W. Lin, *J. Am. Chem. Soc.*, 2014, **136**, 5213–5216.

58 W. Gong, Z. Chen, J. Dong, Y. Liu and Y. Cui, *Chem. Rev.*, 2022, **122**, 9078–9144.

59 R. R. Golwankar, A. Kumar, V. W. Day and J. D. Blakemore, *Chem. – Eur. J.*, 2022, **28**, e202200344.

60 A. Kumar, D. Lionetti, V. W. Day and J. D. Blakemore, *Chem. – Eur. J.*, 2018, **24**, 141–149.

61 Y. J. Park, J. W. Ziller and A. S. Borovik, *J. Am. Chem. Soc.*, 2011, **133**, 9258–9261.

62 D. C. Lacy, Y. J. Park, J. W. Ziller, J. Yano and A. S. Borovik, *J. Am. Chem. Soc.*, 2012, **134**, 17526–17535.

63 Md. A. Alam, M. Nethaji and M. Ray, *Angew. Chem. Int. Ed.*, 2003, **42**, 1940–1942.

64 Md. A. Alam, M. Nethaji and M. Ray, *Inorg. Chem.*, 2005, **44**, 1302–1308.

65 S. C. Sahoo and M. Ray, *Chem. - Eur. J.*, 2010, **16**, 5004–5007.

66 C. R. Das, S. C. Sahoo and M. Ray, *Cryst. Growth Des.*, 2014, **14**, 3958–3966.

67 X.-F. Ma, J.-L. Tian, W. Gu, S. Gao, S.-P. Yan and D.-Z. Liao, *Inorg. Chem. Commun.*, 2008, **11**, 256–259.

68 S. C. Sahoo and M. Ray, *Dalton Trans.*, 2009, 3230.

69 M. Dubey, R. R. Koner and M. Ray, *Inorg. Chem.*, 2009, **48**, 9294–9302.

भारतीय प्रौद्योगिकी संस्थान गुवाहाटी
Indian Institute of Technology Guwahati

Chapter II

Self-assembly-triggered *trans*-to-*cis* conversion of mononuclear Cu(II) via cyclic chiral tri-nuclear assembly

2.1. Introduction

Metal complexes of amino acid-derived reduced Schiff base ligands produce many interesting architectures, including chiral capsules, channels, and cavities.[1–5] Previously, one of our group members reported a set of self-assembled trinuclear assemblies with L-leucine-derived ligand, which have an aliphatic side chain. The assembly has three Ni(II) centres held together by a Na^+ ion and six hydrogen bonds at the centre. The assembly is labile and has three chiral clefts surrounded by an aliphatic amino acid side chain and two H-bond capable -NH groups.[1] Here, we tried to synthesize a similar trinuclear assembly using different amino acid-derived reduced Schiff base ligand.

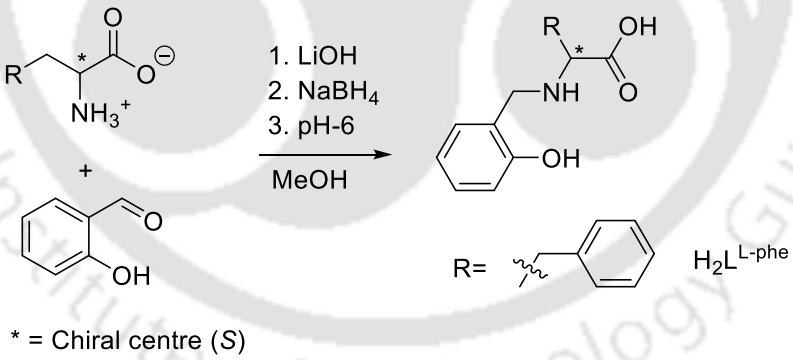

Scheme 2.1. Synthesis of the ligand.

We chose an L-phenylalanine-derived ligand with an aromatic side chain (Scheme 2.1). Using this ligand, we synthesized the monomeric Cu(II) bis complex and tested for the formation of trinuclear assembly (Scheme 2.2). We also check the *cis* and *trans* orientation of the ligand in the monomer Cu(II) bis complex. As previously reported, the *cis* orientation of carboxylates is required to bind with the cations to form the trinuclear assembly.[1] So, it would be interesting to know whether the *trans*-oriented bis complexes will undergo the trinuclear assembly. We also attempted to disassemble the assembly and tried to recover the *cis*-oriented monomeric

units of the assembly. By doing so, we can convert the *trans* to *cis* monomer effectively.[6,7] Interconversion of *cis-trans* metal complex is relatively rare and is most commonly found in azo-based complexes.[8–10] The *cis* and *trans* metal complexes often have different properties. For instance, cisplatin is often used for chemotherapy, but the transplatin is usually considered to have no medicinal effect.[11] It was the case that the *cis* geometry was for a long time considered as a prerequisite for anticancer activity[12], and therefore, the *trans*-configured complexes have attracted less attention from the researchers. The situation has changed, however, in recent years after several classes of *trans*-configured complexes have been reported to exhibit higher cytotoxicity than the corresponding *cis* isomers[13], with some of them exhibiting antitumor activity in vivo, with a lack of cross-resistance to cisplatin.[14,15] All of these examples are concerned with square-planar platinum complexes.[16–18] The *cis-trans* Copper complexes have also been synthesized, and their magnetic properties variation were studied. However, the *cis-trans* conversion concerns the weak labile axial ligand only.[7] Here we synthesized Cu(II) bis complex as a monomer and its assembly in a stepwise fashion, obtaining a trinuclear metallocrown,[19–22] which is a reminiscence of crown ethers.[23–26] We then disassembled the assembly and obtained bis assembly of different geometry. We also observed and studied the penta and hexa-coordination preferences of the Cu(II) monomer and its possible effect on the assembly formation.[27]

2.2. Experimental section

2.2.1. Materials and Methods

Solvents were obtained from commercial sources and used without further purifications unless otherwise stated. O-Salicylaldehyde was purchased from Aldrich Chemical and Co. L-phenylalanine was purchased from SPECTROCHEM Pvt. Ltd. Mumbai, India. Copper acetate and potassium nitrate were purchased from Merck and used as received. The IR spectra were recorded on a Nicolet FT-IR spectrophotometer with KBr discs in the 4000-400 cm^{-1} range. UV-visible spectra of the samples were measured with a PerkinElmer Lambda 365^{+} UV-vis spectrometer. UV-visible spectra of the solid samples were measured with a PerkinElmer Lambda 750 UV-vis spectrometer. NMR spectra were recorded on Bruker 500 MHz. ESI-mass spectra were recorded with a high-resolution mass spectrometer (Agilent 6546 LC/Q-TOF). Solid-state magnetic susceptibility of the complexes at room temperature was recorded using Sherwood Scientific Magnetic Balance MSB-1.[28] Diamagnetic corrections were calculated

using standard values.[29] Elemental analyses were done using a ThermoFisher Scientific Flash smart V CHNS/O analyzer.

2.3. Synthesis and Characterization

2.3.1. $H_2L^{L\text{-}phe}$. The amino acid L-phenylalanine (2.00 g, 12.1 mmol) and LiOH • H_2O (0.510 g, 12.1 mmol) were dissolved in 25 mL of methanol and stirred for 10 min, which gave a colourless solution. The methanolic solution of salicylaldehyde (1.48 g, 12.1 mmol) was added dropwise to the above solution. The solution turned yellow immediately. The solution was stirred for 2 h, and solid $NaBH_4$ (0.500 g, 13.2 mmol) was added portion-wise. The solution turned colourless within a few minutes. It was stirred for another 1 h, and the solvent was removed using a rotary evaporator. The solid obtained was dissolved in ~5 mL of water and acidified to pH 6-7 using dil HCl. White solid precipitated out. The solid was filtered, washed with water, and dried in a vacuum desiccator. Yield 2.16 g (85.1%). ^{1}H NMR was recorded as Lithium salt of the Ligand [$Li_2L^{L\text{-}phe}$], prepared by adding 2 Equiv of LiOH • H_2O in CD_3OD. ^{1}H NMR [$Li_2L^{L\text{-}phe}$] (CD_3OD), 500 MHz ppm) 2.68 (t, 1H, H^8, J =5 Hz), 3.12 (d, 1H, H^7, J =14 Hz), 3.21 (d, 1H, H^9, J =17 Hz), 3.36 (d, 1H, H^{9a}, J =17 Hz), 3.79 (d, 1H, H^{7a}, J =14 Hz), 6.30 (t, H, H^4, J =7.50 Hz), 6.60 (d, 1H, H^2, J =8.00 Hz), 6.71(d, 1H, H^5, J =7.50 Hz), 6.90 (t, 1H, H^3, J =8.00 Hz), 7.21 (m, 5H, $H^{11, 11a, 12, 12a, and\ 13}$). FTIR (KBr, cm^{-1}) ν (OH) 3034, ν $(COOH)_{asym}$ 1594 (s), 1461 (s), ν $(COOH)_{sym}$ 1386 (m). m/z (ESI-MS [$H_2L^{L\text{-}phe}$ +H]$^+$), calcd: 272.12, found 272.11.

2.3.2. Et_4NSCN • Et_4NCl (2 g, 12 mmol) and KSCN(1.17 g, 12 mmol) were mixed in 20 mL of dry MeOH and stirred for 12 h. The white, solid precipitate was filtered out using a G4 crucible. The solvent was removed using a rotary evaporator. The colourless needle-shaped crystals obtained were collected and dried under a vacuum desiccator. Yield: 2.11 g (92%). FTIR (KBr, cm^{-1}) ν (-SCN) 2058. m/z (ESI-MS [Et_4N]$^+$); calcd: 130.25 found 130.16

Note. For elemental analysis, the crystalline samples were powdered and dried under a vacuum desiccator for several days before analysis. Thus, the number and type of solvent molecules in the crystal structure and isolated product differ. We used the formula weight of the bulk for solution concentration and magnetic moment calculation.

2.3.3. $[Cu(HL^{L\text{-}phe})_2]$ (1). Ligand $H_2L^{L\text{-}phe}$ (0.200 g, 0.73 mmol) and $Cu(CH_3COO)_2$ • H_2O (0.072 g, 0.369 mmol) were dissolved in 25 mL of MeOH. The solution changed from blue to

green colour within 5 min. We stirred for 2 h. The green solid precipitated out. The solution was filtered, and the green solid was washed with MeOH and dried under a vacuum desiccator. Yield: 0.186 g (84%). Anal. Calcd for $[Cu(HL^{L\text{-}phe})_2](H_2O)$: C, 61.77, H, 5.50, N, 4.50. Found: C, 61.92, H, 5.28, N, 4.62. FTIR (KBR, cm^{-1}): ν (OH) 3214 (b), ν $(COOH)_{asym}$ 1616, (s) $(COOH)_{sym}$ 1460 (s). m/z (ESI-MS, $[Cu(HL^{L\text{-}phe})_2 + H]^+$); calcd: 604.16 found 604.17. μ_{eff} (powder, 298, K); 1.86 μB/Cu.

2.3.4. $Et_4N[Cu(HL^{L\text{-}phe})_2(SCN)]$ (2). $H_2L^{L\text{-}phe}$ (0.200 g, 0.73 mmol) and $Cu(CH_3COO)_2 \cdot H_2O$ (0.72 g, 0.369 mmol) were dissolved in 25 mL of MeOH and stirred for 10 mins. The solution turns green. We added tetraethylammonium thiocyanate(0.138 g, 0.73 mmol) and stirred for 2 h. We removed the solvent, and the green solid obtained was washed with ethyl acetate and dissolved in hot methanol for recrystallization. After 2 days, the diamond-shaped green crystals were obtained. We collected the crystal wash with ethyl acetate and dried it under a vacuum desiccator. Yield: 0.197 g (69.1%). Anal. Calcd for $Et_4N[Cu(HL^{L\text{-}phe})_2(SCN)]$: C, 62.13, H, 6.61, N, 7.069, S, 4.04. Found: C, 61.75, H, 6.17, N, 6.95, S, 6.01. FTIR (KBR, cm^{-1}): ν (SCN^-) 2079, ν $(COOH)_{asym}$ 1630(s), 1587 (s), ν $(COOH)_{sym}$ 1462 (s). m/z (ESI-MS, $[Cu(HL^{L\text{-}phe})_2 - H]^-$); calcd: 602.14 found 602.15. μ_{eff} (powder, 298, K); 1.92 μB/Cu.

2.3.5. $[K\{Cu(HL^{L\text{-}phe})_2\}_3]NO_3$ (A). Ligand $H_2L^{L\text{-}phe}$ (0.200 g, 0.73 mmol) was mixed with $Cu(CH_3COO)_2 \cdot H_2O$ (0.073 g, 0.365 mmol) in 20 mL of MeOH, which offered a green solution. After 20 min, KNO_3 (0.036 g, 0.36 mmol) was added. The colour of the solution changed from green to light blue. The solution was stirred for 2 h and was evaporated to dryness in a rotary evaporator. The resulting crude blue solid was recrystallized by dissolving in the minimum volume of MeOH, followed by the addition of CH_3CN. The diamond-shaped blue crystals were obtained after 2 days of slow evaporation. Crystals were dried under a vacuum desiccator. Yield: 0.154 g, (65.5%). Anal. Calcd for $[K\{Cu(HL^{L\text{-}phe})_2\}_3]NO_3$: C, 60.25, H, 5.05, N, 5.12. Found: C, 59.14, H, 4.98, N, 5.08, S, 6.01. FTIR (KBr, cm^{-1}): ν (OH) 3246 (b), ν $(COOH)_{asym}$ 1615 (s), ν $(COOH)_{sym}$ 1459 (m), ν (NO_3^-) 1384 (s). m/z (ESI-MS, $[K\{Cu(HL^{L\text{-}phe})_2\}_3]^+$); calcd: 1850.46 found 1850.43 μ_{eff} (powder, 293 K): 1.91 μ_B.

Alternatively, **A** can be prepared from **1**. We took the complex **1** (0.200 g, 0.33 mmol) in 20 mL of MeOH, which was not soluble. We added KNO_3 (0.033 g, 0.33 mmol) and stirred for 2 h. The solution turns clear blue. We removed the solvent, and the blue solid obtained was dissolved in a mixture of MeOH and DMF, layered with diethyl ether, and kept in the freezer

for crystallization. The diamond-shaped blue crystals were obtained after 3 days. The crystals were collected, washed with acetonitrile, and dried under a vacuum desiccator. Yield: 0.186 g (88%). FTIR (KBr, cm^{-1}): ν (OH) 3246 (b), ν $(COOH)_{asym}$ 1615 (s), ν $(COOH)_{sym}$ 1457 (m), ν (NO_3^-) 1384 (s). m/z (ESI-MS, $[K\{Cu(HL^{L\text{-}phe})_2\}_3]^+$); calcd: 1850.46 found 1850.43 μ_{eff} (powder, 293 K): 1.90 μ_B.

Alternatively, **A** can also be prepared from **2**. We mixed complex **2** (0.200 g, 0.25 mmol) in 20 mL of MeOH, which gave us the blue solution. We added KNO_3 (0.026 g, 0.33 mmol) and stirred for 2 h. The solution remains blue. We removed the solvent, and the blue solid obtained was dissolved in a mixture of MeOH and DMF, layered with diethyl ether, and kept in the freeze for crystallization. The diamond-shaped blue crystals were obtained after 3 days. We collected the crystals, washed them with acetonitrile, and dried them under a vacuum desiccator. Yield: 0.099 g (61.8 %). FTIR (KBr, cm^{-1}): ν (OH) 3245 (b), ν $(COOH)_{asym}$ 1615 (s), ν $(COOH)_{sym}$ 1458 (m), ν (NO_3^-) 1384 (s). m/z (ESI-MS, $[K\{Cu(HL^{L\text{-}phe})_2\}]^+$; calcd: 1850.41 found 1850.40 μ_{eff} (powder, 293 K): 1.95 μ_B.

2.3.6. $[Cu(HL^{L\text{-}phe})_2]$ (3). The Assembly **A** (0.2 g, 0.10 mmol) was dissolved in 10 mL of DMF. The solution turns blue, and we add 1,4,7,10,13,16-Hexaoxacyclooctadecane (0.055 g, 0.2 mmol), stir for 1 hr, and keep it for slow evaporation. The blue block shape crystals were obtained after 3 days. We collected the crystal, washed it with acetone, and dried it under a vacuum desiccator. Yield: 0.127 g (57 %). Anal. Calcd for $[Cu(HL^{L\text{-}phe})_2]$• DMF: C, 61.77, H, 5.50, N, 4.50. Found: C, 62.23, H, 5.57, N, 5.62. FTIR (KBR, cm^{-1}): ν (OH) 3214 (b), ν $(COOH)_{asym}$ 1616, (s) $(COOH)_{sym}$ 1460 (s). m/z (ESI-MS, $[[Cu(HL^{L\text{-}phe})_2]+H]^+$); calcd: 604.16 found 604.17. μ_{eff} (powder, 298, K); 1.95μB/Cu.

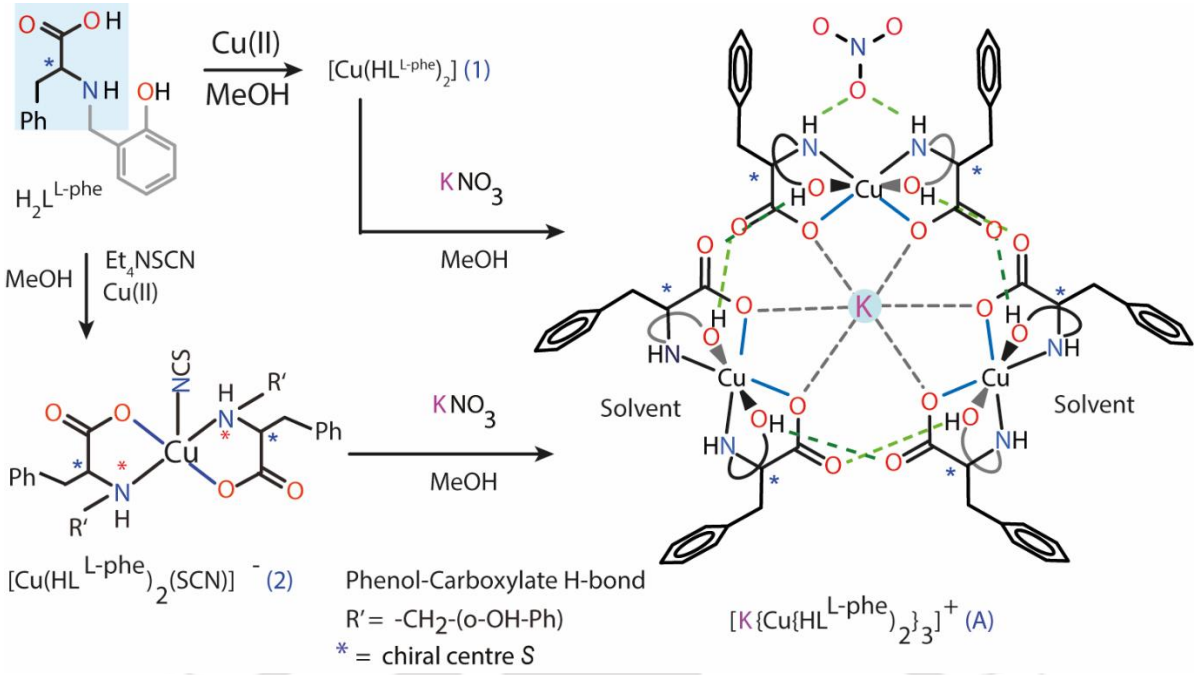

Scheme 2.2. Synthesis of Cu(II) bis complexes and their assembly formation.

2.4. X-ray Crystallography

The crystal of the complexes obtained during synthesis was used for X-ray analysis. The crystals were mounted on glass fibre. All geometric and intensity data for the crystal (**A**) was collected at room temperature using a Bruker SMART APEX CCD diffractometer equipped with a fine focus 1.75 kW sealed tube Mo-Kα (λ= 0.71073 Å) X-ray source, with increasing ω (width of 0.3º per frame) at a scan speed of either 3 or 5 s/frame. The SMART software was used for data acquisition and the SAINT software for data extraction. Absorption corrections were done using a multi-scan. For the crystals (**2** and **3**), the intensity data were collected at room temperature using a single Source Super Nova CCD System from Agilent Technologies equipped with a fine focus 1.75 kW sealed tube with Mo-Kα radiation. The data were reduced using CrysAlis RED.[30] The structure solution and refinement were performed on the WinGX environment using the SHELXS97 SHELXL97 programs.[31] All non-hydrogen atoms were refined anisotropically. The hydrogen atoms were located from the Fourier maps and refined isotropically wherever possible. Thus, some C-H bonds will not be ideal and may vary. Most hydrogen atoms attached to the solvent molecules could not be located or fixed, so the molecular weight may not match. ORTEP obtained selected crystallographic data summarized in Table 2.1. A perspective view of the complex was obtained by ORTEP.[32]

Table 2.1. Selected crystallographic data for the complexes[a].

Compound	**2**	**A**	**3**
Empirical formula	$C_{41}H_{52}CuN_4O_6S$	$C_{98}H_{96}Cu_3KN_7O_{25}$	$C_{38}H_{46}CuN_4O_8$
M	792.46	2001.53	750.34
Wavelength (Å)	0.71073	0.71073	0.71073
Crystal system	Triclinic	Orthorhombic	Orthorhombic
Space group	*P 1*	*C 2 2 2₁*	*P 2₁ 2₁ 2*
A, Å	8.8990(4)	30.6800(4)	16.152(2)
b, Å	9.5835(5)	13.6570(13)	20.912(2)
c, Å	12.1262(5)	23.7900(2)	5.5692(7)
α, deg	77.371	90.00	90.00
β, deg	84.750	90.00	90.00
γ, deg	88.364	90.00	90.00
V, Å^3	1004.87(8)	9968(18)	1881.1(4)
Z	1	4	2
ρ, g cm^{-3}	1.310	1.334	1.325
μ, mm^{-1}	0.646	0.751	0.636
Flack parameter	0.012(11)	0.005(6)	0.12(13)
Reflections collected	5718	12227	3671
Independent reflections	5465	8042	3072
Goodness of fit	0.975	1.032	1.108
Final *R* indices [*I* >2σ(*I*)]	*R*1 = 0.0389	*R*1 = 0.0598	*R*1 = 0.0964
	*wR*2 =0.1002	*wR*2 = 0.1034	*wR*2 = 0.2522
R indices (all data)	*R*1 = 0.0417	*R*1 = 0.1369	*R*1 = 0.1087
	*wR*2 =0.1041	*wR*2 = 0.1573	*wR*2 = 0.2700

[a]Refinement method: full-matrix least-squares on F^2

2.5. Result and discussion

We synthesized the reduced Schiff base ligand $H_2L^{L\text{-phe}}$ using amino acid L-phenylalanine and O-salicyaldehyde. We used LiOH to de-protonate the zwitterionic amino acid. *In situ,* the reduction of the Schiff base and subsequent pH adjustment resulted in the ligand (experimental section 2.3.1). The ligand is insoluble in most of the organic solvents. Therefore, we used LiOH to record ^{1}H NMR. The reaction between divalent Cu(II) acetate and ligand $H_2L^{L\text{-phe}}$ in MeOH at a 1:2 ratio yields the complex **1**. We used Cu(II) acetate to avoid the presence of alkali metal ions, which facilitates the formation of assembly. Attempts to get the solid-state structure of complex **1** fail as the crystals desolvate very quickly (experimental section 2.3.3). Complex **2** was synthesized using Cu(II) acetate to avoid the presence of alkali metal ions, which facilitates the formation of assembly. The reaction between divalent Cu(II) acetate, Et_4NSCN, and ligand $H_2L^{L\text{-phe}}$ in MeOH at a 1:2:2 ratio resulted in a blue solid. We crystallized from MeOH, yielding the block-shaped blue crystals of **2**. Complex **2** was structurally characterized. The complex **1** and **2** were characterized using elemental analysis, ESI-Mass spectra, FTIR spectra, and solid-state magnetism. The room temperature solid-state magnetic moments lie between 1.9 to 2.1 B.M, which are within the expected range of monomeric Cu(II) complexes.[33]

2.5.1. $Et_4N[Cu(HL^{L\text{-phe}})_2(SCN)]$ (2). Complex **2** was synthesized using Cu(II) acetate to avoid the presence of alkali metal ions, which facilitates the formation of assembly. The reaction between divalent Cu(II) acetate, Et_4NSCN, and ligand $H_2L^{L\text{-phe}}$ in MeOH at a 1:2:2 ratio resulted in a blue solid. We crystallized from MeOH, yielding the block-shaped blue crystals of **2**. Complex **2** was crystallized in space group *P*1. The structural parameters labelled molecular structure and selected bond lengths and angles are in Fig 2.1. The square pyramidal geometry around Cu(II) is due to the coordination of two mono-protonated $HL^{L\text{-phe}}$ ligands and thiocyanate coordinated axially via the nitrogen atom, and a tetrabutylammonium acts as the counter ions.[34] The two $HL^{L\text{-phe}}$ coordinated in a trans-N2O2 mode, and phenols remain uncoordinated to Cu(II). The deviation of bond angles from 90° and 180° indicates that the complex has a distorted square pyramidal geometry. The N1A-Cu-N1B deviated the most at 158.3° from 180°, and the Cu(II) is slightly above the plane with a distance of 0.34 Å. The thiocyanate binds with Cu(II) at an angle of approximately 100° from the plane, and the axial bond length of Cu-ND 2.163(4) Å is slightly longer than Cu-NA and Cu-NB as expected for the axial bond length.

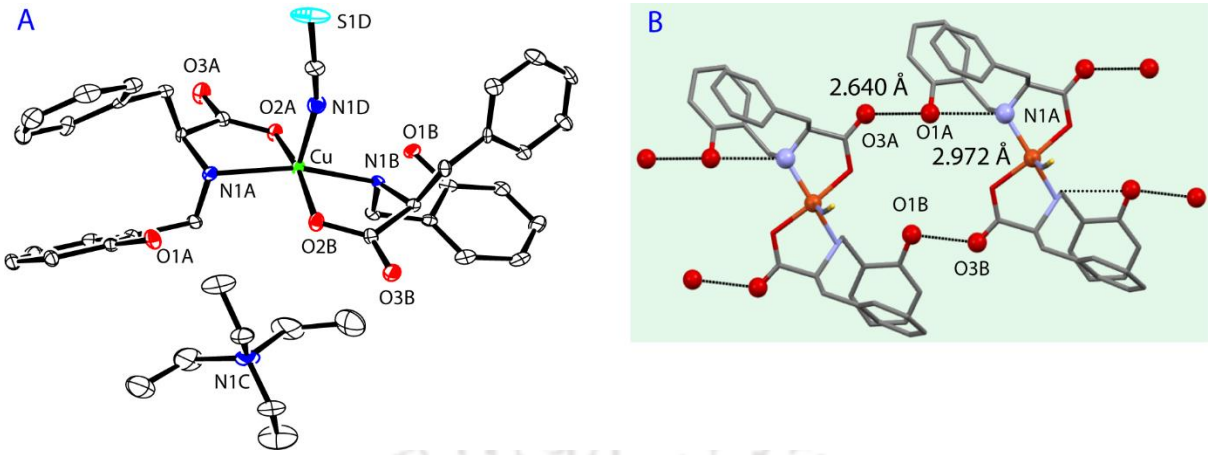

Fig 2.1. ORTEP diagram (A) with thermal ellipsoid set at 50 % probability and ball and stick model (B) showing the intermolecular and intramolecular hydrogen bonding pattern of **2**.

Selected bond distance (Å) and angles (°) of 2: Cu-O2A 1.963(3), Cu-O2B 1.975(3), Cu-N1A 2.010(4), Cu-N1B 2.018(4) Cu-N1D 2.163(4), O2A -Cu -O2B 161.48(12), N1A-Cu-N1B 158.36 (14), O2A -Cu-N1A 83.55(13), O2A-Cu-N1B 93.30(12), O2A-Cu-N1D 96.71(13), O2B-Cu -N1D 101.82(13).

H-bonds: N1A…O1A 2.972(4), O1A…O3A 2.640(4), O1B...O3B 2.640(4).

The in-plane distances are comparable to the corresponding distances in **3** and **A** (section 2.5.2, and 2.6.1). However, when compared to **3** and **A**, the axial bond length in **2** is considerably short and might be due to the pentacoordination around Cu(II) as opposed to hexa coordination. The chiral carbon C8A and C8B conformation are *S*, as the amino acid used in synthesis was an *S* isomer. In addition to the asymmetric carbon centre in the ligand, the coordination of amide N1A and N1B to the Cu(II) gives rise to an asymmetric secondary nitrogen atom with the *R* configuration. The phenol (O1A and O1B), uncoordinated carboxylate (O3A and O3B), and amine (N1A and N1B) are H-bonded in a linear three-centre two H-bond in a complementary fashion (Fig 2.1B), which leads to the formation of a one-dimensional chain of molecules this phenomenon is observed in the previously reported similar types of complex[1,5]. The H-bond between phenol and carboxylate is 2.64 Å. The complex is fairly soluble in MeOH. The addition of solid KNO_3 to a methanolic solution of **2** yielded crystals of **A**, which was confirmed from FTIR, ESI-Mass, visible spectra, and crystal parameter determinations. Notable in this transformation is the trans orientation of the in-plane ligands in **2** to the cis orientation in **A**, which is necessary for binding the alkali metal ion. This result substantiates

that carboxylate groups necessary for alkali metal binding were not predisposed in the Cu(II) monomers but were a result of alkali metal ion-influenced reorientation.

2.5.2. $[K\{Cu(HL^{L\text{-}thr})_2\}_3]NO_3$ (A). Assembly **A** can be synthesized directly using ligand copper acetate and KNO_3 at the ratio of 2:1:1, and it can also be synthesized stepwise from complexes **1** and **2** by adding KNO_3 (experimental section 2.3.5). Assembly **A** was characterized using elemental analysis, ESI-Mass, FTIR, and solid-state magnetism. The room temperature solid-state magnetic moments have a value of 1.95 B.M, which is within the expected range of monomeric Cu(II) complexes.[33] Assembly **A** crystallizes in the space group $C222_1$, where half of the assembly is identical, with the other half connected through symmetry (Fig 2.2). Thus, one Copper is on the crystallographic 2-fold axis, and another is on the general position. The asymmetric units also contain water, a MeOH molecule, and half of the nitrate molecules, acting as a counter ion. Some of the selected bond lengths are in Table 2.2.

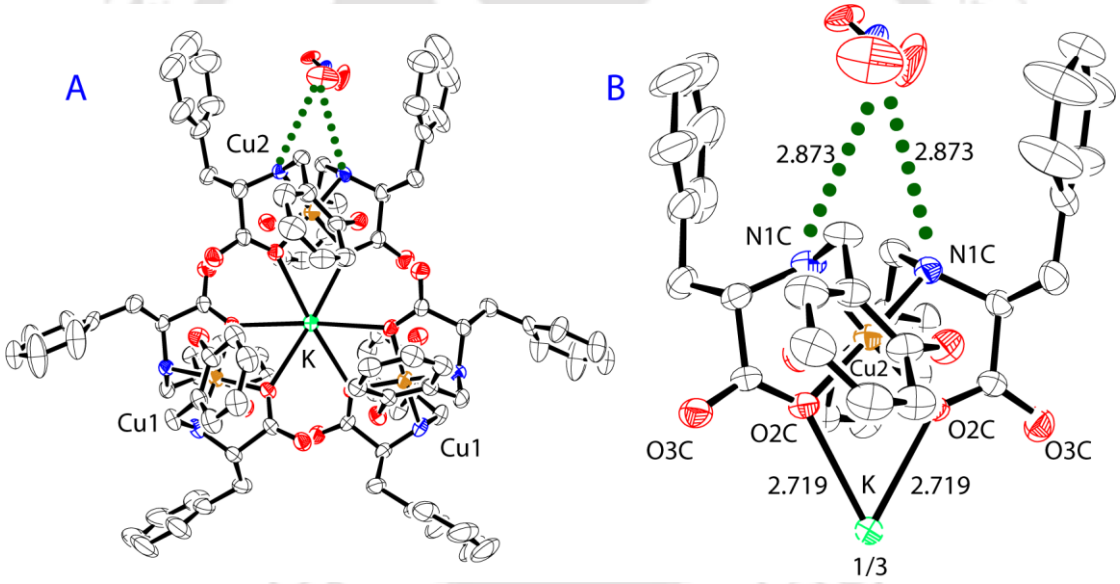

Fig 2.2. ORTEP diagram (A) with thermal ellipsoid set at 30 % probability and coordination around one Cu(II) unit (B) depicting the cation and anion binding sites of **A**

Selected bond angles (°) of **A**: O1A -Cu1-O1B 167.67(16), O1A-Cu1-O2A 88.03(18), O1A-Cu1-N1A 88.31(19), O1B-Cu1-O2A 83.53(19), O1B-Cu1-O2B 85.86(17), O2A-Cu1-N1B 172.2(2), O1C-Cu2-O2C 86.92(17), O1C-Cu2-N1C 87.64(18), O1C-Cu2-O1C_a 165.30(16), O1C-Cu2-N1C_a 101.90(18).

In assembly **A**, K^+ is hexa-coordinated by three $[Cu^{II}(HL^{L\text{-}phe})_2]$ units through the six carboxylate oxygens, where the carboxylates are in *cis* orientation in all three units (Fig 2.2A).

In each of the $[Cu^{II}(HL^{L\text{-}phe})_2]$, Cu(II) is hexacoordinated by two facial tridentate ligands. The carboxylate oxygens are simultaneously coordinated with Cu(II) and K^+ (Figure 2.2B). Each of the ligands in assembly **A1** has one acidic proton, which is H-bonded between phenolic oxygen (O1A) and carboxylate oxygen (O3C) from the neighbouring $[Cu^{II}(HL^{L\text{-}phe})_2]$ unit (Fig 2.3A). Thus, there are six such H-bonds in one molecule of $[K\{Cu(HL^{L\text{-}phe})_2\}_3]^+$. These H-bonds are on the short end of the 2.5−3.0 Å range usual for O···O H-bond distance[35].

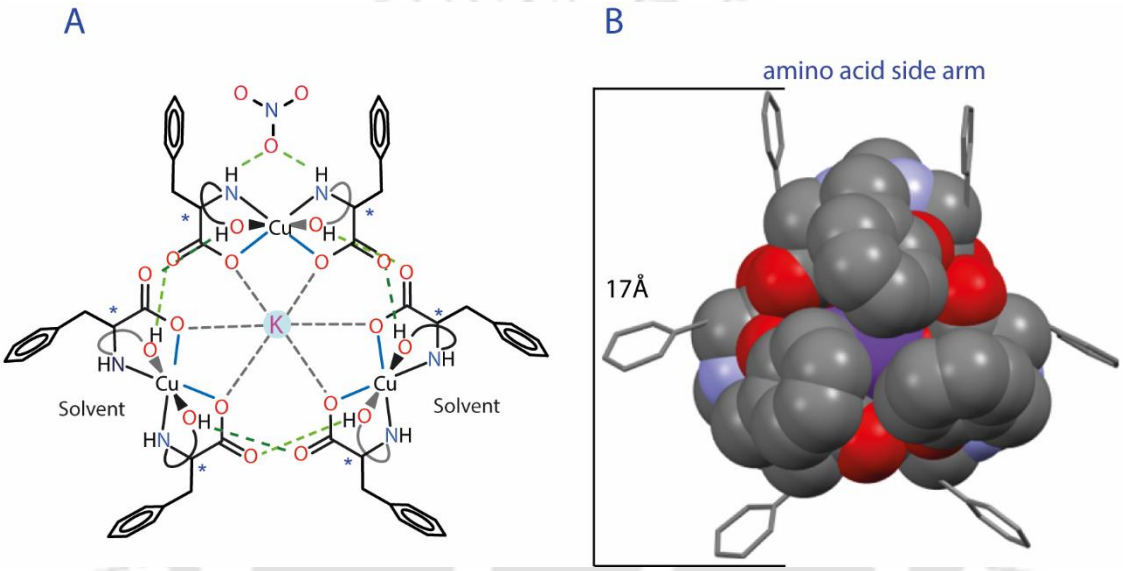

Fig 2.3. Sketch model (A) showing the cation and anion binding sites and the position of six hydrogen bonds and space-filled model (B) with amino acid side arm shown as stick model of **A**.

The aromatic rings of the ligands completely encapsulate the central potassium ion from both sides in a capsular shape with six amino acid residues extending on the surface (Fig 2.3B). While the *cis* orientation of carboxylates allowed the $[Cu^{II}(HL^{L\text{-}phe})_2]$ unit to bind K^+, a similar orientation of amines provided the H-bonding site for the anions, making the capsular assembly capable of binding both anion and cation of a salt within the same assembly in solid state (Fig 2.3A). The conformation at the chiral carbon of the ligand is *S*. In addition to the asymmetric carbon centre in the ligand, the coordination of amine N to the Cu(II) gives rise to an asymmetric secondary nitrogen atom which has the *R* configuration. This phenomenon of opposite conformation preference at chiral carbon and amine N has been observed in all the characterized complexes of this type of ligand[11,12], and the K-O bond length of ~2.7Å is

comparable to those found in the literature.[36] The Cu-NH and Cu-Ocarboxylate bond lengths of the monomer and its assembly are more or less equal. As expected for octahedral Cu complexes, The Cu-Ophenols bond length is longer due to Jahn Teller distortion. The oxo anions form bridges between two neighbouring assemblies through two H-bonds between amine NH and two different oxygen atoms of the oxo anion, creating an extensively H-bonded three-dimensional network. This might be the reason behind the poor solubility of the assemblies in common organic solvents. Assembly **A** is soluble in polar DMF and only partially soluble in MeOH and water (<50 mg in 10 mL of MeOH). The lattice also contains MeOH and water as crystallization solvents.

2.5.3. Solution identity of the assembly

The ESI-Mass spectra of all the complexes were recorded in DMF. The spectra of **1** and **A** were recorded as *m/z* (ESI-MS,$[M+H]^+$), and for **2,** it was recorded as *m/z* (ESI-MS,$[M-H]^-$). Monomer **1** shows the molecular ion peak at 604.16 with a matching isotopic abundance pattern (Fig 2.4) of $[Cu(HL^{L\text{-}phe})_2+H]^+$, indicating the presence of the bis complex in the solution. The monomer **2** shows the molecular ion peak at 602.14 with a matching isotopic abundance pattern (Fig 2.5) of $[Cu(HL^{L\text{-}phe})_2\text{-}H]^-$ indicates the dissociation of axially bound -SCN from the Cu(II) centre. The spectra of assembly **A** with the matching isotopic patterns of $[K\{Cu(HL^{L\text{-}thr})_2\}_3]^+$ at 1850.43 supports the presence of the assemblies in solution (Figure 2.6 and Table 2.3). Using the ESI-Mass spectrometry, we can characterize the monomers **1**, **2**, and assembly **A**. We can get evidence of the assembly stability in solution from the mass spectra.[37]

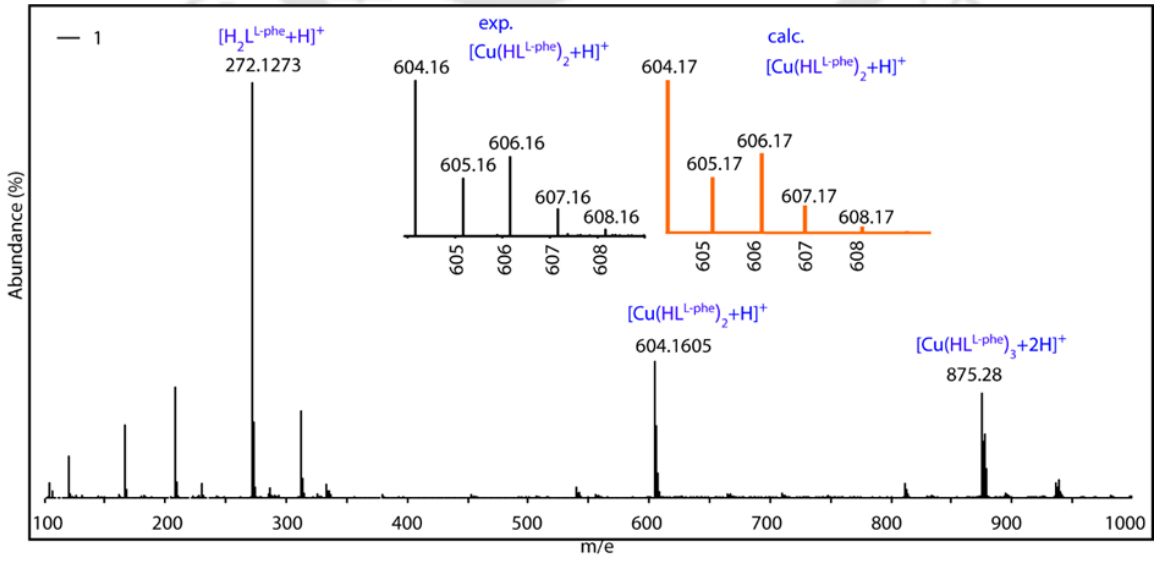

Figure 2.4. ESI-Mass spectra of **1** (+ve) in DMF

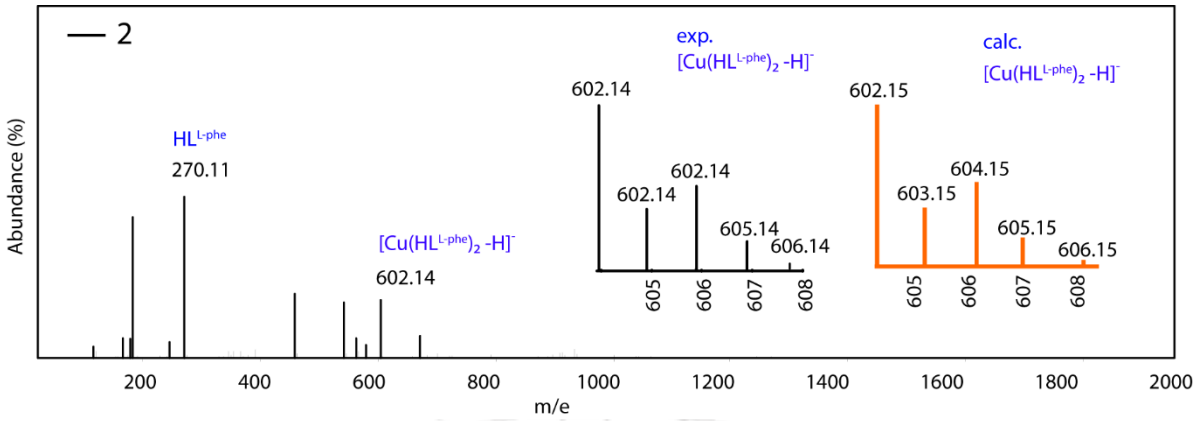

Figure 2.5. ESI-Mass spectra of **2** (-ve) in DMF

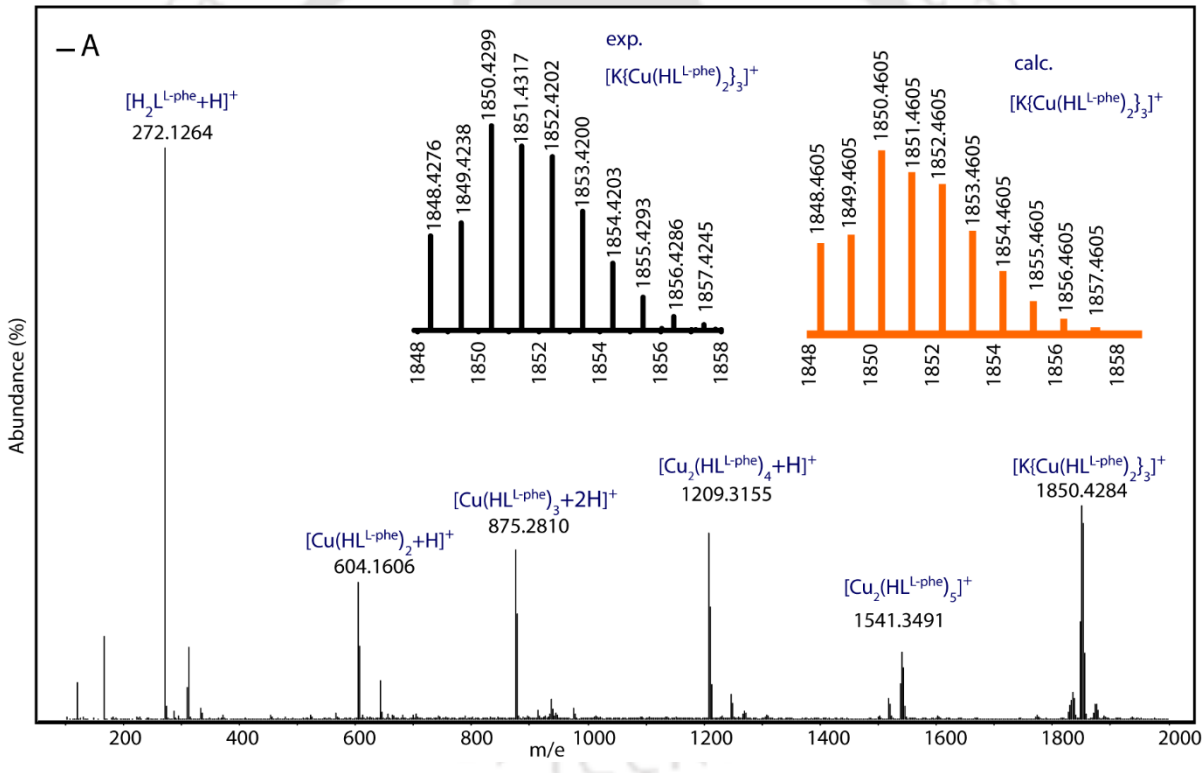

Fig 2.6. ESI-Mass spectra of **A**(+ve) in DMF

2.6. Disassembly of assembly A using [18] crown-6

From the solid-state structure, we know that monomer **2** has the *trans* carboxylates, and assembly **A** has the *cis* orientation, so we tried to recover the *cis*-oriented Cu(II) units of assembly **A** by adding 2 equiv of [18] crown-6 to the DMF solution of the assembly **A** (experimental section 2.3.6).

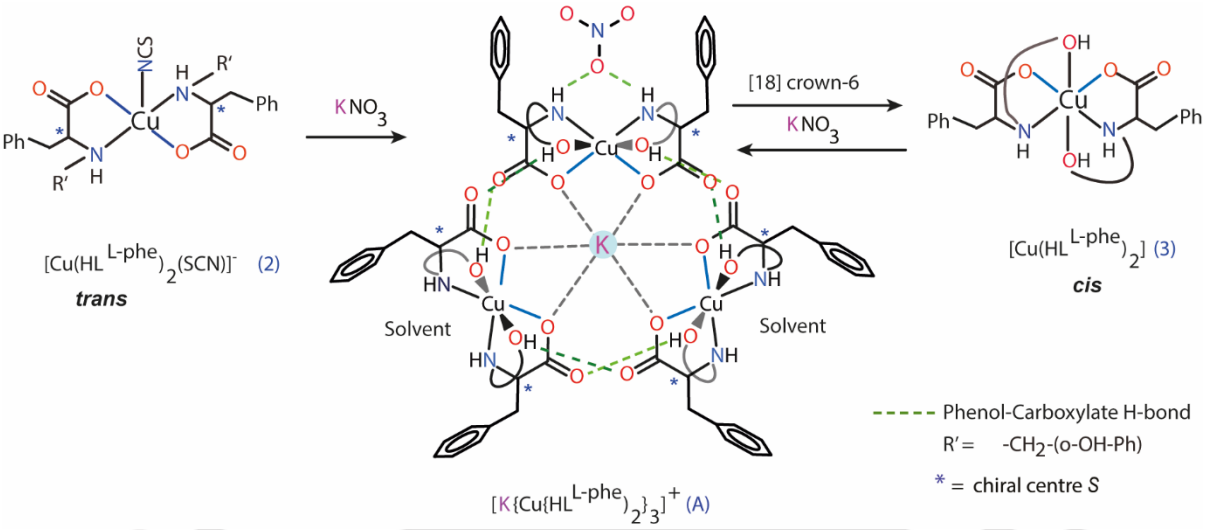

Scheme 3. Conversion of *trans* to *cis* carboxylates via cyclic chiral trinuclear assembly and disassembly of assembly **A**.

2.6.1. [Cu(HL$^{L\text{-phe}}$)$_2$] (3). Complex **3** was synthesized by dissolving the assembly **A** in DMF and adding [18] crown-6. Complex **3** crystallized in the chiral space group *P* 2_1 2_1 *2* with half of the molecules and a DMF in the asymmetric unit. The bond lengths, angles and labelled ORTEP diagram are in Fig 2.4. The complex consists of two mono-protonated HL$^{L\text{-phe}}$, octahedrally coordinated to a Cu(II) at the centre. The HL$^{L\text{-phe}}$ is coordinated as a tridentate facial ligand. The ligands in the complex have two chiral centres at C8 and N1 with *S* and *R* configurations, respectively. This phenomenon of opposite conformation preference at chiral carbon C8 and amine N1 has been observed in all the characterized complexes of this type of ligand.[5,38] The deviation of bond angles from ideal 90° and 180° indicates that the complex obtained a distorted octahedral geometry.[39] The bond angle O1-Cu-N1_a (106.02) deviated the most. As expected, the Cu-N1 bond length of 2.010(7) Å is slightly longer than Cu-O2 with a bond length of 1.944(6) Å. The axial Cu-O1 bond length is significantly longer, with a bond length of 2.709(6) Å due to Jahn-Teller distortion, as expected for octahedral copper complexes[40]. The two carboxylates in the complex are in cis orientation, forming a hydrophilic

region surrounded by the two phenyl and two phenolates' aromatic rings (Figure 2.7B), which can bind with the cation.[41] The notable observation is the hexa-coordination of Cu(II), which otherwise prefers to be pentacoordinate in almost all the complexes reported so far with similar ligands.[5,38,42,43] However, the Cu-Ophenols bond length of monomer **3** is relatively longer (2.709 Å) compared to its assembly complex **A,** which has a bond length of ~ 2.4 Å (Table 2.2).

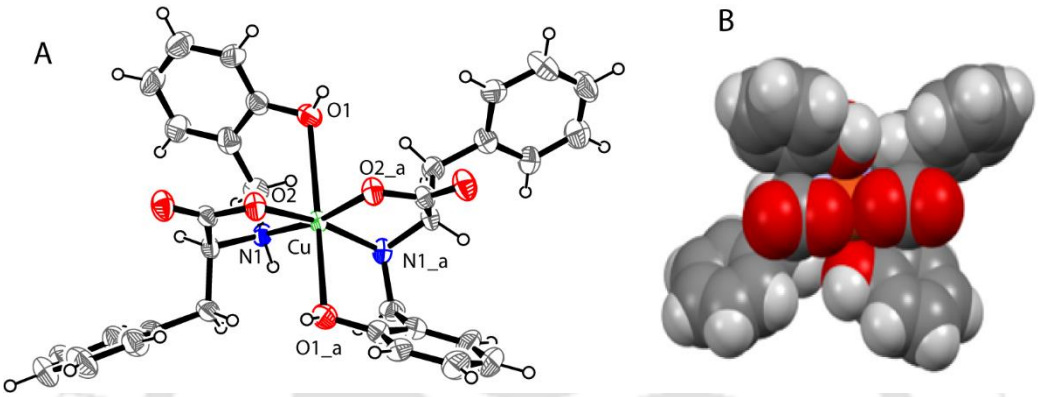

Fig 2.7. ORTEP diagram (**3**) with thermal ellipsoid set at 40 % probability and (B) space-filled model of **3**.

Selected bond distance (Å) and angles (°) of **3**: Cu-O1 2.709(6), Cu-O2 1.944(6), Cu-N1 2.010(7), O1-Cu -O2 85.8(2), O1-Cu-N1 85.1(2), O1-Cu-O1_a 163.2(2), O1-Cu-N1a 106.2(2), O2-Cu-N1_a 167.8(3).

H-bonds: O1…O4 2.654(12), N1…O2 2.962(9), O1…C9 2.654(12), O3…C19 2.654(12).

Table 2.2. Selected bond length (Å) of the complexes.

Compounds	Cu–Ocarboxy	Cu-Ophenol	Cu–Namine	K-Ocarboxy	OH....O
2	1.977(3), 1.963(3)		2.014(4), 2.009(4)		
A	1.968(5), 1.963(5), 1.958(5)	2.459(6), 2.465(6), 2.414(6)	2.019(6), 2.009(6), 2.000(6)	2.745(6), 2.724(5), 2.719(5)	2.624(8), 2.573(8), 2.570(8)
3	1.944(6)	2.709(6)	2.010(7)		

2.6.2. ESI-Mass spectrometry of monomer 3

The ESI Mass spectrum of complex **3** in DMF was recorded as *m/z* (ESI-MS,$[M+H]^+$. The monomer **3** also shows the molecular ion peak at 604.16 with a matching isotopic abundance pattern (Fig 2.7) of $[Cu(HL^{L\text{-}phe})_2+H]^+$. The isotopic pattern at 1850 corresponding to $[K\{Cu(HL^{L\text{-}thr})_2\}_3]^+$ was absent. This indicates the disassembly of the assembly. We also tested for the reassembly of monomer **3** back to assembly **A** by adding an excess of KNO_3 to the DMF solution of monomer **3** and recorded the ESI-Mass (Figure 2.7). We found that the spectrum resembles the spectrum of assembly **A**. Hence, monomer **3,** which has pre-exposed *cis*-oriented, readily reforms back to assembly **A** in the presence of K^+ ions.

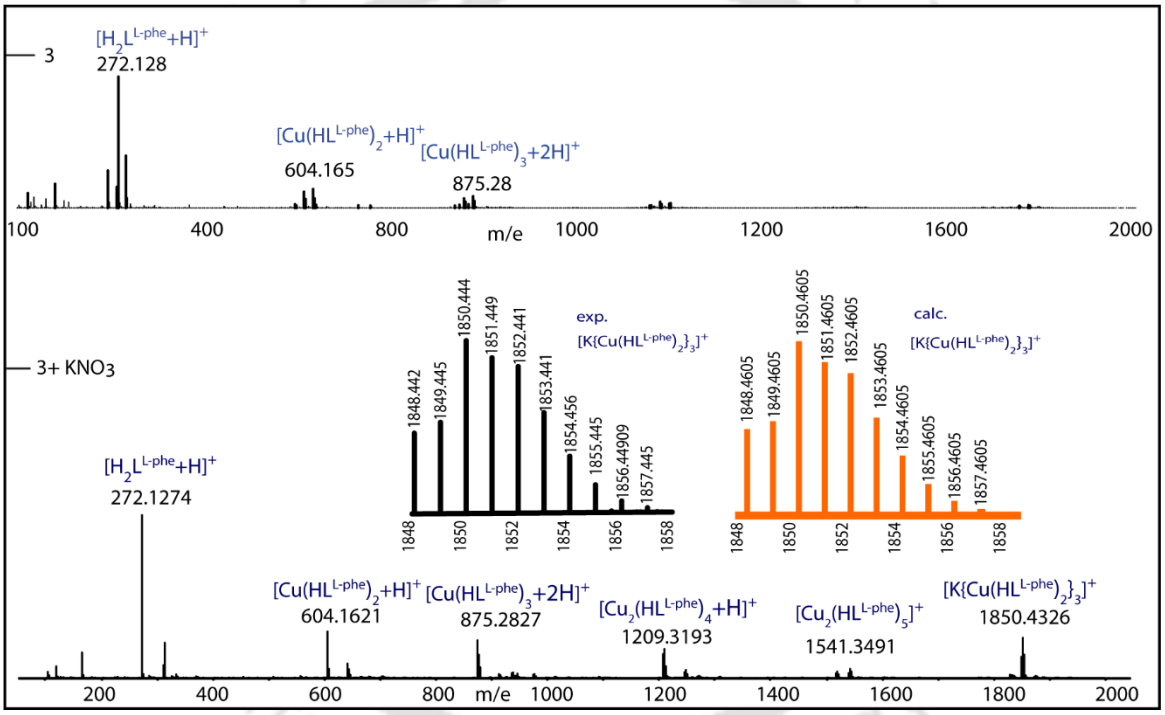

Figure 2.7. ESI-Mass spectra of **3** and **3**+KNO_3 in DMF.

Table 2.3. Mass spectral data.[a]

	calc. m/Z (relative intensity)[b]	exp. m/Z (relative intensity)[b]
1	604.17(100), 605.17(36)	604.17(100), 605.17(45)
	606.17(52), 607.17(17)	606.16(50), 606.17(20)
2	604.15(100), 605.15(45)	602.14(100), 603.14(33)
	606.15(50), 606.15(20)	604.12(53), 605.14(14)
A	1848.46(49), 1849.46(53)	1848.43(45), 1849.43(55)
	1850.46(100), 1851.46(87)	1850.43(100), 1851.43(85)
	1852.46(80), 1853.46(55)	1852.42(80), 1853.42(59)
	1854.46(33), 1855.46(16)	1854.42(30), 1855.43(15)
	1856.46(7), 1857.46(2)	1856.43(8), 1857.42(3)
3	604.16(100), 605.16(45)	604.16(100), 605.16(48)
	606.16(50), 606.16(20)	606.16(52), 606.16(16)

[a] in DMF, [b] isotopic mass distribution of molecular ion peak with relative intensity values in parenthesis. **1**=[Cu($HL^{L\text{-}phe}$)$_2$], **2**=[Cu($HL^{L\text{-}phe}$)$_2$], **A**=[K{Cu($HL^{L\text{-}phe}$)$_2$}$_3$]$^+$, **3**=[Cu($HL^{L\text{-}phe}$)$_2$]

2.7. Absorption spectroscopy

The UV-visible spectral characteristic data of the bis complexes and assembly are given in Table 2.4, and the spectral figure of appropriate complexes is shown in Fig 2.9. The absorption maxima between 350-400 nm are due to LMCT.[44,45] The absorption maxima between 600-700 nm are assigned for the d-d transition, usually for the Cu(II) complexes.[46,47] Monomer **2** with coordination number five has a d-d transition at 615 nm quite differs (Fig 2.9B) from monomer **1** as expected due to differences in the coordination number and the structural environment around the Cu(II) centre.[41,48] However, when we added extra KNO_3 to the monomers **1** and **2** solutions, the spectra were similar to assembly **A**, indicating the transformation of the hexa and penta coordinated monomer to assembly **A** (Fig 2.9 C-D). **Table 2.4.** Electronic spectral data.[a]

Complex	**1**	**2**	**A**	**3**
λ_{max}, (ε, $M^{-1}cm^{-1}$)	372(707)	398(70)	378(168)	374(229)
	665(134)	615(145)	645(130)	660(128)

[a] Scan range in DMF, 300-1100. ε values calculated using ~1 mM solutions.

1=[Cu($HL^{L\text{-}phe}$)$_2$], **2**=Et_4N[Cu($HL^{L\text{-}phe}$)$_2$(SCN)], **A**=[K{Cu($HL^{L\text{-}phe}$)$_2$}$_3$]NO_3, **3**=[Cu($HL^{L\text{-}phe}$)$_2$]

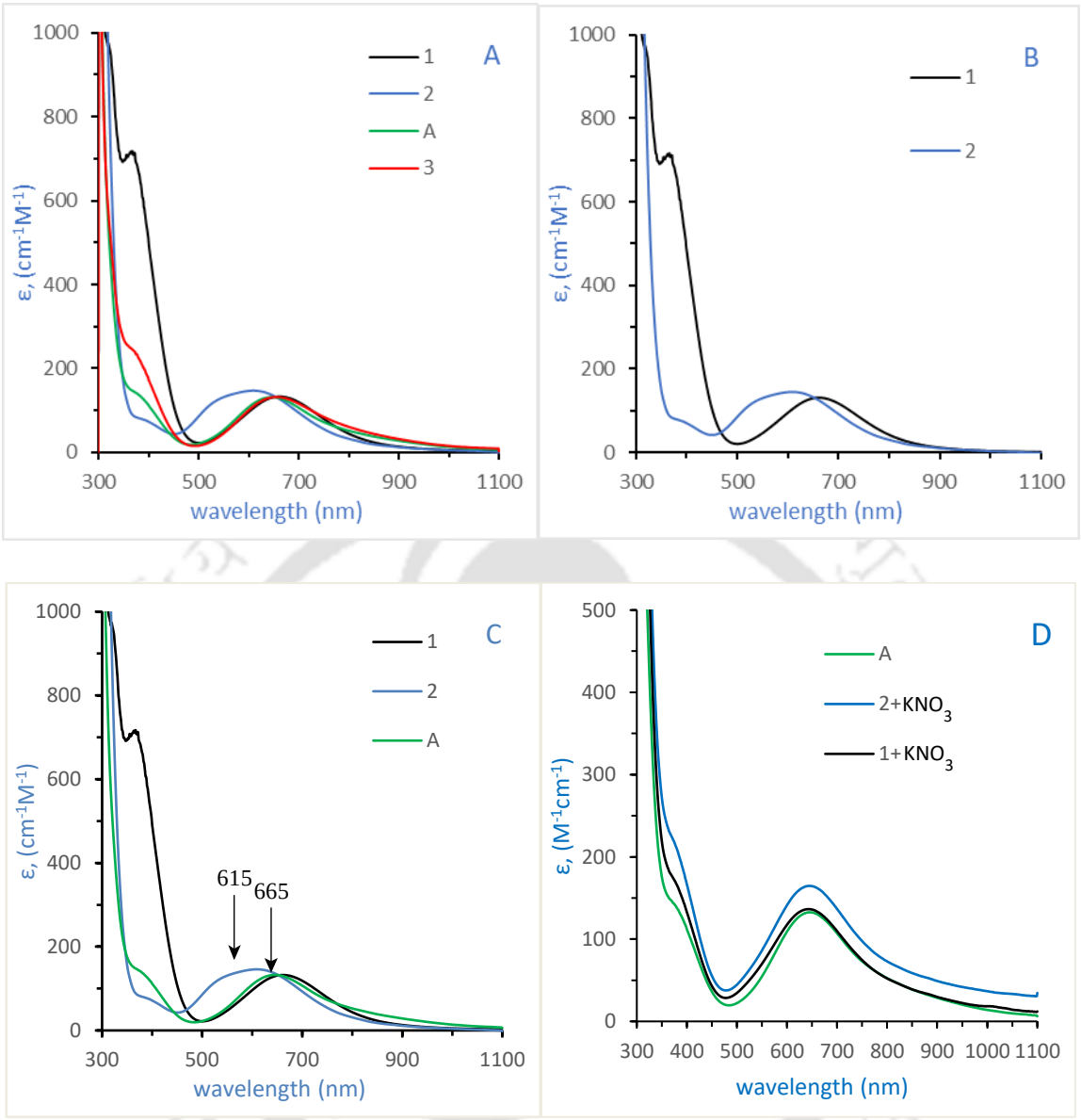

Fig 2.9. UV-Visible spectra of (A) monomers **1**, **2**, **3**, and their assembly **A,** (B) monomers **1** and **2,** (C) monomers **1**, **2**, and its assembly **A**, before and after the addition of KNO_3 (D) in DMF

Monomers **1** and **3** have a d-d transition at 665 nm and 660 nm, respectively (Fig 2.10A), while the trinuclear assembly **A** has a d-d transition at 645 nm, with a red shift of ~ 20 and 15 nm, respectively. We also recorded the spectra of **A** and re-recorded it after the addition of [18] crown-6 (Fig 2.10B). We notice the blueshift in the spectra (Fig 2.10B). This indicates two things. Firstly, it confirms the dissociation of assembly **A** to monomer **3** in the solution. Secondly, it gives us evidence that the binding of K^+ in **A** causes minor perturbation in the ligand strengths around the Cu(II). On the other hand, monomer **2** has a shift of ~50 nm to

lower energy from monomer **3**. As others have suggested, this shift in the spectra might be due to structural change rather than the effect of alkali metal ions.[1,37,49]

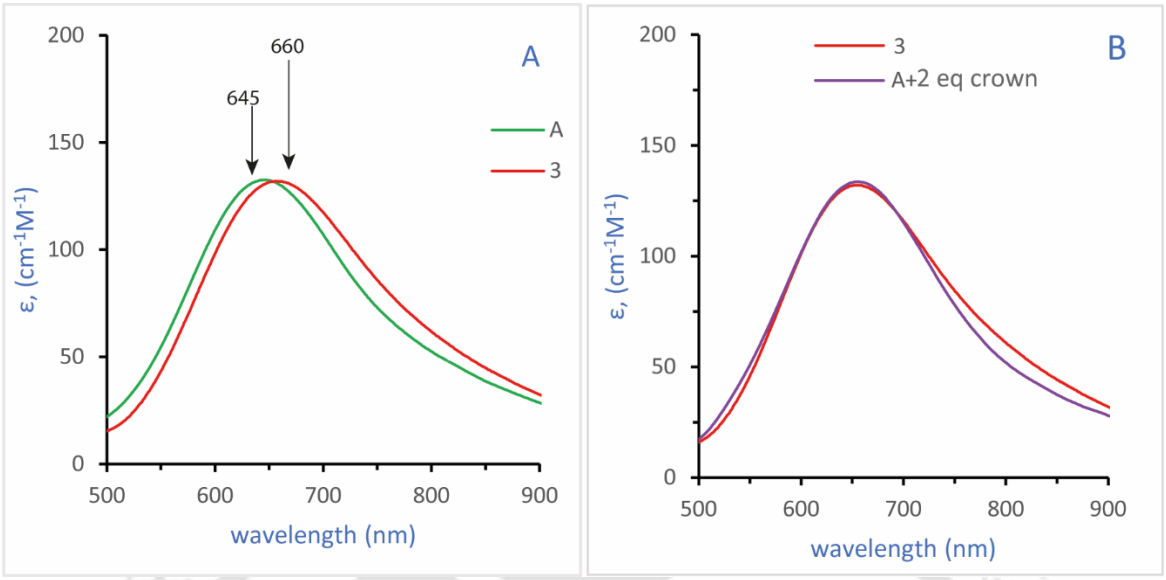

Fig 2.10. UV-visible spectra of assembly **A** and monomers **3** before (A) and after (B) the addition of [18] crown-6 in DMF.

2.8. Solid-state UV-visible spectra

The solid-state UV-visible of the complexes were recorded and compared to the solution state spectra. The solid-state d-d transition absorption maxima of monomers **2** (606 nm), **3** (640 nm), and assembly **A** (648 nm) are close to that of the solution-state spectra (Table 2.4). This indicates the retention of solid-state structure in solution. The assembly **A** absorption maxima value (648 nm) is also very close to that of monomer **3** (640 nm) as both have octahedral geometry. The similarity and close value of the absorption maxima value of monomer **3** and assembly **A** is evidence that the K^+ ion has little influence in the UV-visible spectra. In the case of monomer **1** (706 nm), the spectrum was significantly shifted (~40 nm) when compared to solution state (665 nm) UV-visible spectra**.** This indicates that the solution and solid-state structure differ for monomer **1**. We could not obtain the solid-state structure of monomer **1**. However, the d-d transition value (665 nm) of the solution state UV-visible spectrum is close to that of octahedral complex **3** and assembly **A**. This indicates that the monomer **1** in solution is likely an octahedral complex. The redshift of ~100 nm in solid-state spectra between monomers **2** and **3** can be attributed to the geometry and coordination changes around the Cu(II) centre.[27]

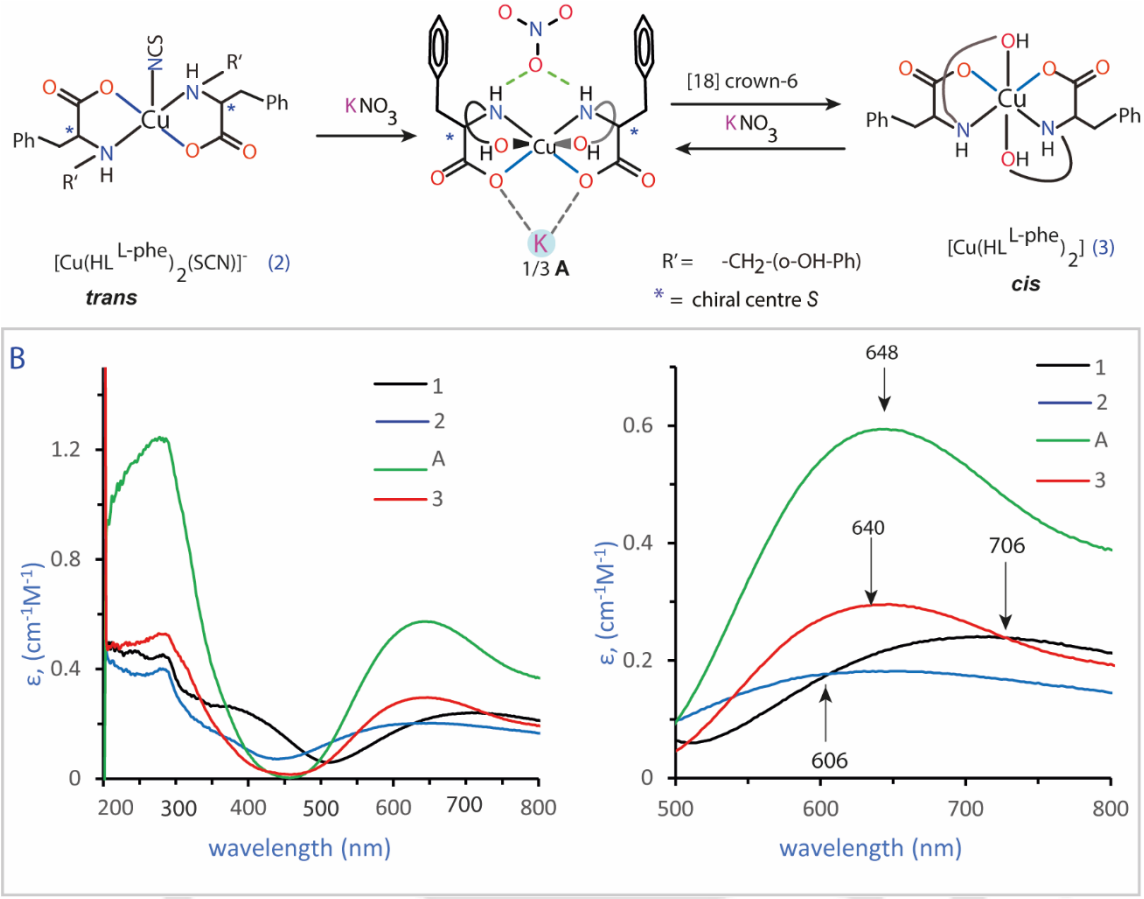

Figure 2.11. Sketch model of the solid-state structure of the complexes (A) and the solid-state UV-visible spectra of the complexes.

2.9. Conclusion

In this chapter, we synthesized the cyclic chiral trinuclear complexes using a ligand with an aromatic sidearm with Cu(II) and K^+ ions. We can also synthesize the assembly stepwise with five and six-coordinated Cu(II) bis complex as a monomer. The penta-coordinated Cu(II) bis complex with in-plane N_2O_2 fashion has a square pyramidal geometry and *trans*-oriented carboxylate. Still, it can form the assembly in the presence of the K^+ ion. This shows that both *trans*-oriented Cu(II) bis complexes can be used as a monomer to synthesize the trinuclear complex. The assembly has three monomer units encapsulating the K^+ ion through six oxygen donors, forming a cryptate-like adduct. The assembly is homochiral with three potential chiral recognition sites on the surface (three pairs of N-H between the amino acid sidearm. Upon addition of [18] crown-6, the assembly was disassembled into monomeric units, where the identity of the assembly's monomeric units' cis orientation and hexa coordination were intact, and we could isolate and characterize them. The disassembled *cis*-oriented hexa-coordinated monomer can still be used to reform the assembly in the presence of the K^+ ions. There is a redshift when we compare the UV-visible spectra of monomer **3** with that of assembly **A**. From this, we can detect the spectroscopically silent metal ion (When we used the word “silence”, we meant UV-silent" to imply that K^+ ion is silent in electronic spectra) by UV-visible spectra spectroscopy.

2.10. References

1 G. González-Riopedre, M. R. Bermejo, M. I. Fernández-García, A. M. González-Noya, R. Pedrido, M. J. Rodríguez-Doutón and M. Maneiro, *Inorg. Chem.*, 2015, **54**, 2512–2521.

2 R. Ganguly, B. Sreenivasulu and J. J. Vittal, *Coord. Chem. Rev.*, 2008, **252**, 1027–1050.

3 B. Sreenivasulu and J. J. Vittal, *Angew. Chem. Int. Ed.*, 2004, **43**, 5769–5772.

4 Md. A. Alam, M. Nethaji and M. Ray, *Angew. Chem. Int. Ed.*, 2003, **42**, 1940–1942.

5 Md. A. Alam, M. Nethaji and M. Ray, *Inorg. Chem.*, 2005, **44**, 1302–1308.

6 P. Zoufalý, A. Kliuikov, E. Čižmár, I. Císařová and R. Herchel, *Eur. J. Inorg. Chem.*, 2021, **2021**, 1190–1199.

7 A. Biswas, M. G. B. Drew, C. Diaz, A. Bauzá, A. Frontera and A. Ghosh, *Dalton Trans.*, 2012, **41**, 12200.

8 A. Gavriluta, G. E. Büchel, L. Freitag, G. Novitchi, J. B. Tommasino, E. Jeanneau, P.-S. Kuhn, L. González, V. B. Arion and D. Luneau, *Inorg. Chem.*, 2013, **52**, 6260–6272.

9 K. Ghosh, S. Banerjee and S. Chattopadhyay, *CrystEngComm*, 2019, **21**, 6026–6037.

10 Z. Wu, R. Xue, M. Xie, X. Wang, Z. Liu, M. Drechsler, J. Huang and Y. Yan, *J. Phys. Chem. Lett.*, 2018, **9**, 163–169.

11 T. Kishimoto, Y. Yoshikawa, K. Yoshikawa and S. Komeda, *Int. J. Mol. Sci.*, 2019, **21**, 34.

12 B. Rosenberg, L. Vancamp, J. E. Trosko and V. H. Mansour, *Nature*, 1969, **222**, 385–386.

13 Y. Yu. Scaffidi-Domianello, K. Meelich, M. A. Jakupec, V. B. Arion, V. Yu. Kukushkin, M. S. Galanski and B. K. Keppler, *Inorg. Chem.*, 2010, **49**, 5669–5678.

14 M. Coluccia, A. Nassi, A. Boccarelli, D. Giordano, N. Cardellicchio, D. Locker, M. Leng, M. Sivo, F. P. Intini and G. Natile, *J. Inorg. Biochem.*, 1999, **77**, 31–35.

15 C. Bartel, A. K. Bytzek, Y. Yu. Scaffidi-Domianello, G. Grabmann, M. A. Jakupec, C. G. Hartinger, M. S. Galanski and B. K. Keppler, *JBIC J. Biol. Inorg. Chem.*, 2012, **17**, 465–474.

16 S. Bernès, F. J. Meléndez and H. Torrens, *Acta Crystallogr. Sect. C Struct. Chem.*, 2016, **72**, 268–273.

17 C. Rivera, H. A. Bacilio-Beltrán, A. M. Puebla-Pérez, I. I. Rangel-Salas, J. G. Alvarado-Rodríguez, R. Flores-Moreno, G. Velázquez-Juárez, A. A. Peregrina-Lucano, E. Becerra-Martínez, J. Valdez-Ruvalcaba, J. E. Rubio and S. A. Cortés-Llamas, *New J. Chem.*, 2022, **46**, 14221–14226.

18 M. F. Galimova, T. A. Begaliev, E. M. Zueva, S. A. Kondrashova, S. K. Latypov, A. B. Dobrynin, I. E. Kolesnikov, R. R. Musin, E. I. Musina and A. A. Karasik, *Inorg. Chem.*, 2021, **60**, 6804–6812.

19 A. B. Chung, D. N. Huh, J. W. Ziller and W. J. Evans, *Inorg. Chem. Front.*, 2020, **7**, 4445–4451.

20 S. O. Kang, J. M. Llinares, V. W. Day and K. Bowman-James, *Chem. Soc. Rev.*, 2010, **39**, 3980.

21 I. R. Ariyarathna, *Inorg. Chem.*, 2022, **61**, 579–585.

22 D. N. Huh, C. J. Windorff, J. W. Ziller and W. J. Evans, *Chem. Commun.*, 2018, **54**, 10272–10275.

23 F. Nicoli, M. Baroncini, S. Silvi, J. Groppi and A. Credi, *Org. Chem. Front.*, 2021, **8**, 5531–5549.

24 S. V. Eliseeva, E. V. Salerno, B. A. Lopez Bermudez, S. Petoud and V. L. Pecoraro, *J. Am. Chem. Soc.*, 2020, **142**, 16173–16176.

25 C. J. Pedersen, *Angew. Chem. Int. Ed. Engl.*, 1988, **27**, 1021–1027.

26 J. W. Steed, *Coord. Chem. Rev.*, 2001, **215**, 171–221.

27 J. S. Pap, B. Kripli, V. Bányai, M. Giorgi, L. Korecz, T. Gajda, D. Árus, J. Kaizer and G. Speier, *Inorganica Chim. Acta*, 2011, **376**, 158–169.

28 D. F. Evans 1974 *J. Phys. E: Sci. Instrum.* 7 247

29 C. J. OConnor, Prog. Inorg. Chem., 1982, **29**, 203

30 CrysAlis CCD and CrysAlis RED. Oxford Diffraction Ltd, Yarnton, Oxfordshire, England. Oxford Diffraction, 2009

31 G. M. Sheldrick, Acta Crystallogr., Sect. A: Fundam. Crystallogr., 2008, A64, 112

32 M. N. Burnett and C. K. Johnson, ORTEP-III: Oak Ridge Thermal Ellipsoid Plot Program for Crystal Structure Illustrations, Oak Ridge National Laboratory Report ORNL-6895, 1996

33 W. J. Geary, *Coord. Chem. Rev.*, 1971, **7**, 81–122.

34 S. Volodarsky, I. Malahov, D. Bawari, M. Diab, N. Malik, B. Tumanskii and R. Dobrovetsky, *Chem. Sci.*, 2022, **13**, 5957–5963.

35 R. Miyake, S. Tashiro, M. Shiro, K. Tanaka and M. Shionoya, *J. Am. Chem. Soc.*, 2008, **130**, 5646–5647.

36 A. K. Patra, M. Ray and R. Mukherjee, *Polyhedron*, 2000, **19**, 1423–1428.

37 M. Dubey, R. R. Koner and M. Ray, *Inorg. Chem.*, 2009, **48**, 9294–9302.

38 S. C. Sahoo and M. Ray, *Dalton Trans.*, 2007, 5148.

39 I. Persson, P. Persson, M. Sandström and A.-S. Ullström, *J. Chem. Soc. Dalton Trans.*, 2002, 1256.

40 M. V. Veidis, G. H. Schreiber, T. E. Gough and G. J. Palenik, *J. Am. Chem. Soc.*, 1969, **91**, 1859–1860.

41 M. Andruh, *Dalton Trans.*, 2015, **44**, 16633–16653.

42 L. L. Koh, J. O. Ranford, W. T. Robinson, J. O. Svensson, A. L. C. Tan and D. Wu, *Inorg. Chem.*, 1996, **35**, 6466–6472.

43 S. Zehra, T. Roisnel and F. Arjmand, *ACS Omega*, 2019, **4**, 7691–7705.

44 Z. Wei, Y. Peng, D. L. Hughes, J. Zhao, L. Huang and X. Liu, *Polyhedron*, 2014, **69**, 181–187.

45 R. P. Singh, V. K. Maurya, B. Maiti, K. A. Siddiqui and L. B. Prasad, *J. Coord. Chem.*, 2018, **71**, 3008–3020.

46 M. Lutz, M. Haukka, T. A. Pakkanen and L. H. Gade, *Inorg. Chem.*, 2003, **42**, 2798–2804.

47 M. R. Wagner and F. A. Walker, *Inorg. Chem.*, 1983, **22**, 3021–3028.

48 Md. A. Alam, R. R. Koner, A. Das, M. Nethaji and M. Ray, *Cryst. Growth Des.*, 2007, **7**, 1818–1824.

49 R. R. Golwankar, A. Kumar, V. W. Day and J. D. Blakemore, *Chem. – Eur. J.*, 2022, **28**, e202200344.

भारतीय प्रौद्योगिकी संस्थान गुवाहाटी
Indian Institute of Technology Guwahati

Chapter III

Redesigning of the cyclic chiral trinuclear by changing amino acid sidearm, using inert Co(III) complex, and cation of different sizes and charges

3.1. Introduction

In the previous chapter, we synthesized the Cu(II) monomer bis complex and its trinuclear assembly of the phenylalanine-derived reduced Schiff base, which has an aromatic sidearm (Scheme 2.1). However, the complexes are insoluble in most of the solvents. Therefore, in this chapter, we synthesized the L-serine-derived reduced Schiff base, which has a hydrophilic side arm (Scheme 3.1). We intend to synthesize a similar trinuclear assembly using the newly synthesized ligand.[1] We tried to replace the Cu(II) with the Co(III) metal ion. Our choice of metal ion is such that the Co(III) complexes are likely to be diamagnetic such that we can use ^{1}H NMR spectroscopy to understand the interactions in the solution,[2] and we also plan to replace the central metal K^+ ion with metal ions of different charges and sizes[3] and compare it with the previously synthesized complexes[4].

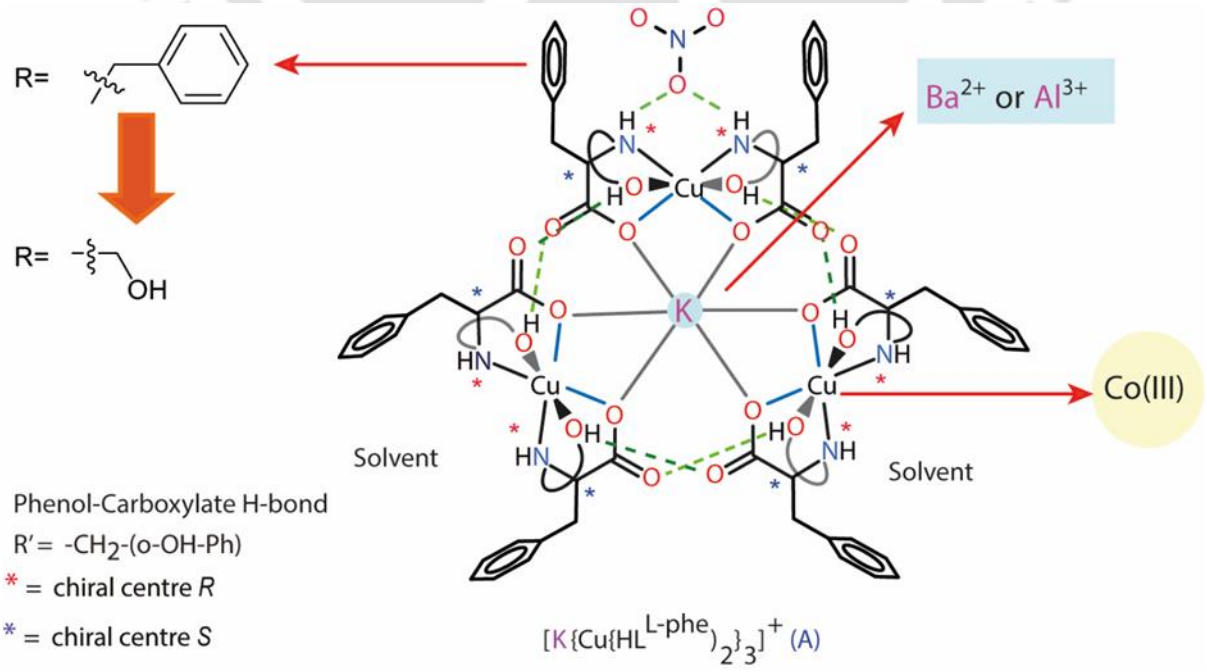

Scheme 3.1. Proposed sketch model of cyclic trinuclear.

3.2. Experimental section

Solvents were obtained from commercial sources and used without further purifications unless otherwise stated. O-Salicylaldehyde was purchased from Aldrich Chemical and Co. L-serine was purchased from SPECTROCHEM Pvt. Ltd. Mumbai, India. The instrument used was the same as discussed in Chapter 2.

3.3. Synthesis and Characterisation

3.3.1. $H_2L^{L\text{-}ser}$. L-serine (2.00 g, 19.0 mmol) and LiOH• H_2O (0.79 g, 19.0 mmol) were dissolved in 20 mL of methanol and stirred for 10 min. The methanolic solution of salicylaldehyde (2.31 g, 19.0 mmol) was added dropwise. The solution turned yellow on addition. The solution was stirred for 2 h. Solid $NaBH_4$ (0.70 g, 19.0 mmol) was added portion-wise. The solution turned colourless within a few minutes. It was stirred for another 1 h. The solvent was removed. The solid obtained was dissolved in ~5 mL of and acidified to pH 6-7 using dil HCL. White solid precipitated out. The solid was filtered using a G4 crucible and washed with ethyl acetate. The white solid was dried under a vacuum desiccator. Yield 2.25 g (85.1%). ^{1}H NMR was recorded as Lithium salt of the Ligand [$Li_2L^{L\text{-}ser}$], prepared by adding 2 Equiv of LiOH.H_2O in DMSO-d6. ^{1}H NMR [$Li_2L^{L\text{-}ser}$] (DMSO-d6, 500 MHz ppm) 6.98 (m, 1H, H^5), 6.98 (m, 1H, H^3), 6.51(t, 1H, H^4, *J* =7.5 Hz), 6.14 (d, 1H, H^2, *J* =8 Hz), 3.80 (d, 1H, H^7, *J* =16 Hz), 3.44 (m, 1H, H^9 *J*= 12 Hz), 3.57 (m, 1H, H^{7a}, *J* =16 Hz), 3.44 (m, 1H, H^{9a}, *J* =12 Hz), 2.95 (m, 1H, H^8, *J*=6.5 Hz). m/z (ESI-MS $[M\text{-}H]^-$, $[H_2L^{L\text{-}ser}\text{ -}H]^-$); calcd: 210.07, found 210.07.

3.3.2. $[K(Co(L^{L\text{-}ser})_2]$ (1). $H_2L^{L\text{-}ser}$ (0.200 g, 0.95 mmol) and KOH (0.106 g, 1.90 mmol) were mixed in 10 mL of MeOH, which gave a clear solution after 10 mins. We added a methanolic solution of $Co(ClO_4)_2$• $6H_2O$ (172 mg, 0.48 mmol) to the above-clear solution, which gave a brown solution. We stirred for 3 hrs. The solution turns green. The solvent was removed using a rotary evaporator. The brown solid obtained was washed with ethyl acetate and dissolved in 10 mL of MeOH, layered with diethyl ether, and kept in the freeze. The block-shaped green crystals were obtained after 2 days. Isolated crystals were washed with MeOH and dried under a vacuum desiccator. Yield: 0.145 g (65 %). ^{1}H NMR of [$K(Co(L^{L\text{-}ser})_2$] (DMSO-d_6, 500 MHz. ppm) 7.04 (d, 2H, H^5, *J* =8 Hz), 6.90 (m, 2H, H^2, *J*=7 Hz), 6.90 (m, 2H, H^4, *J*= 7Hz), 6.80 (s, 2H, H^{NH}), 6.35 (t, 2H, H^3, *J* =7 Hz), 5.83 (s, 2H, H^{OH}), 3.87 (m, 2H, H^9, *J*=13.5 Hz), 3.87 (m,

2H, H^7, *J*=15 Hz), 3.74 (m, 2H, H^{9a}, *J* =13.5 Hz), 3.05 (m, 2H, H^{7a}, *J* =15 Hz), 3.05(m, 6H, H^8, *J*=9 Hz).).). m/z (ESI-MS, $[M-H]^-$,$[Co(L^{L\text{-}ser})_2]^-$); calcd:477.07, found 477.07

3.3.3. $[Ba\{(Co(L^{L\text{-}ser})_2\}_2]$ (2). The complex (**1**) (0.200 g, 0.39 mmol) and BaCl2• $2H_2O$ (0.097 g, 0.39 mmol) was dissolved in a round bottom flask and dissolved in 15 mL of Milli-Q water, giving a green solution. We stirred for 2 hrs, and the solution was kept for slow evaporation. The needle-shaped red crystal was obtained after three days. The crystals collected were not stable enough to obtained crystal structure. The crystals were washed with acetone, and dried under a vacuum desiccator. Yield: 0.170 g (75.%). ^1H NMR of $[Ba\{Co(L^{L\text{-}thr]})_2\}(H_2O)_4]$ (DMSO-d_6, 500 MHz. ppm) 7.54 (s, 2H, H^{NH}), 7.27 (m, 2H, H^5), 6.695(m, 2H, H^4), 7.27 (m, 2H, H^2), 6.69 (t, 2H, H^3, *J*=8 Hz), 6.24 (s, 2H, H^{OH}), 3.96 (m, 2H, H^9, *J* =11 Hz), 3.96 (d, 2H, H^7, *J*=16 Hz), 3.95 (m, 2H, H^{9a}, *J* =11 Hz), 3.26 (d, 2H, H^{7a}, *J* =16 Hz), 3.17 (d, 2H, H^8, *J*=4 Hz).

Note: Section 3.3.4. was not synthesized. We added Al^{3+} salt to complex **1** and ^1H NMR was recorded

3.3.4. $[K(Co(L^{L\text{-}ser})_2]$+Al(NO3)3. ^1H NMR (DMSO-d_6, 500 MHz. ppm) 7.23 (d, 2H, H^5, *J* =8 Hz), 7.10 (s, 2H, H^{NH}), 7.01(d, 2H, H^2, *J*=8 Hz), 6.98 (t, 2H, H^4, *J*=16Hz), 6.49 (t, 2H, H^3, *J* =7 Hz), 6.09 (s, 2H, H^{OH}), 3.94 (m, 2H, H^9, *J*=8 Hz), 3.83 (m, 2H, H^7, *J*=12 Hz), 3.71 (m, 2H, H^{9a}, *J* =8 Hz), 3.10 (m, 2H, H^{7a}, *J* =12 Hz), 3.08(m, 6H, H^8, *J*=16 Hz).

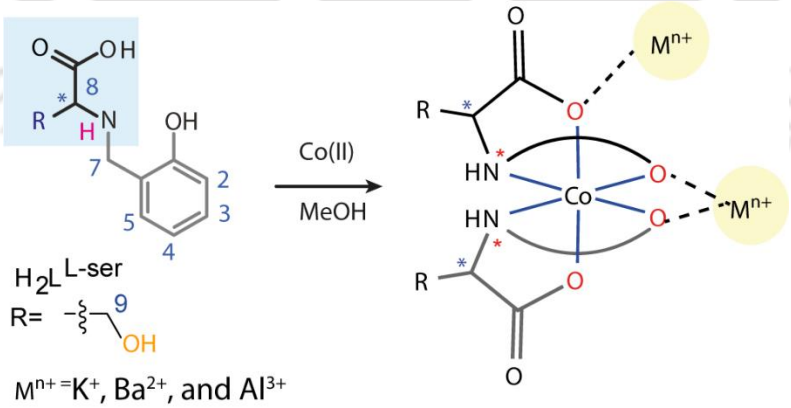

Scheme 3.2. Sketch model of the Co(III) complex polymeric chain formation with cations

3.4. X-ray Crystallography

Crystals of complexe **1** obtained during synthesis were used for X-ray analysis. The crystals were mounted on glass fibre. All geometric and intensity data for the crystal of complex **2** were collected at room temperature using a Bruker SMART APEX CCD diffractometer equipped

with a fine focus 1.75 kW sealed tube Mo-Kα (λ= 0.71073 Å) X-ray source, with increasing ω (width of 0.3º per frame) at a scan speed of either 3 or 5 s/frame. For the crystal of complex **1** the intensity data were collected at room temperature using a single Source Super Nova CCD System from Agilent Technologies equipped with a fine focus 1.75 kW sealed tube with Mo-Kα radiation. The instrument parameters were the same as described in Chapter 2. Selected crystallographic data are summarised in Table 3.1.

Table 3.1. Selected crystallographic data[a] of **1**

Compound	**1**
Empirical formula	$C_{20}H_{24}CoKN_2O_9$
M	534.44
Wavelength (Å)	
Crystal system	monoclinic
Space group	*P* 2_1
A, Å	12.4208(11)
b, Å	7.9265(6)
c, Å	12.9988(11)
α, deg	90.00
β, deg	116.231(2)
γ, deg	90.00
V, Å^3	1147.98(17)
Z	2
ρ, g cm^{-3}	1.546
μ, mm^{-1}	0.982
Flack parameter	0.04(2)
Reflections collected	5938
Independent reflections	3925
Goodness of fit	1.014
Final *R* indices [$I > 2\sigma(I)$]	*R*1 = 0.0432 *wR*2 = 0.0749
R indices (all data)	*R1* = 0.0976 *wR*2 = 0.0876

[a]Refinement method: full-matrix least-squares on F^2.

3.5. Result and discussion

We synthesized the reduced Schiff base ligand $H_2L^{L\text{-ser}}$ using amino acid L-serine and O-salicylaldehyde. We used LiOH to de-protonate the zwitterionic amino acid. *In situ,* the reduction of the Schiff base and subsequent pH adjustment resulted in the ligand (experimental section 3.3.1). The ligand is insoluble in most organic solvents. Therefore, we used LiOH to record ^{1}H NMR. Complex **1** was synthesized by reacting divalent Co(II), KOH, and ligand $H_2L^{L\text{-ser}}$ in MeOH at a 1:4:2 ratio. We used the diffusion method for the crystallization of complexes **1**. Complex **1** and **2** were characterized using elemental analysis, 1H NMR, 2D-NMR, ESI-Mass, and FTIR.

3.5.1. [K(Co($L^{L\text{-ser}}$)$_2$] (1). Complex **1** crystallized in the chiral space group *P2$_1$*. The asymmetric unit contains Co(III) bis complexes coordinated to K^+ through the two phenolates and one of the carboxylates.

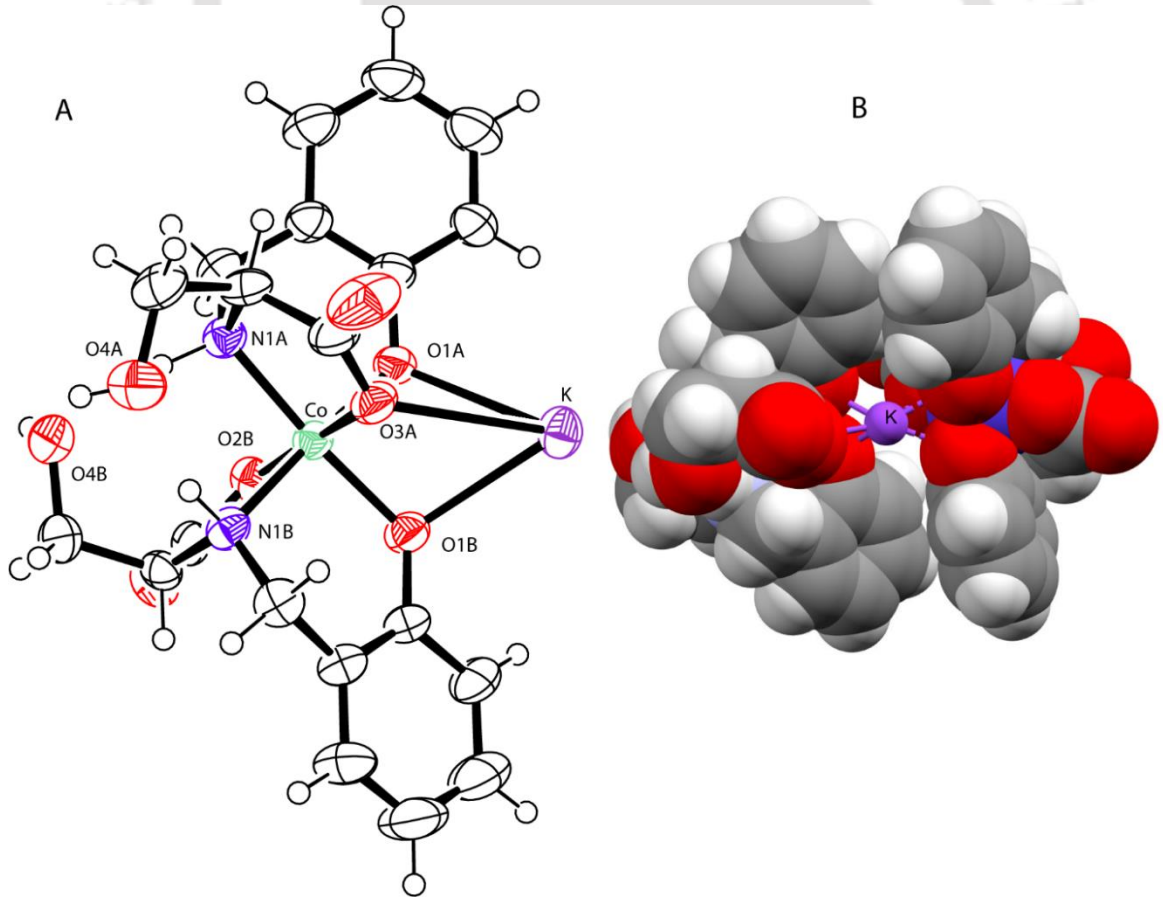

Figure 3.1. (A) ORTEP diagram of **1** with thermal ellipsoids set to 50 % probability level, and (B) spaced filled model of **1** depicting how the two Co(III) bis complexes sandwiched the K^+ ion.

The bond lengths, angles and labelled molecular structure are in Table 3.2 and Fig 3.1, respectively. The complex consists of doubly-deprotonated $L^{L\text{-ser}}$, octahedrally coordinated to a Co(III) at the centre. The $L^{L\text{-ser}}$ is coordinated as a tridentate *facial* ligand. The ligands in the complex have three chiral centres at C8A, C9A, and N1a with *S*, *R*, and *R* configurations, respectively. This phenomenon of opposite conformation preference at chiral carbon C8A and amine N1A has been observed in all the characterized complexes. The deviation of bond angles from ideal 90° and 180° indicates that the complex obtained a distorted octahedral geometry (Table 3.2). As expected, the Co-NH bond length of ~1.95 Å is slightly longer than Co-Op, with a bond length of ~1.900 Å. The Co(III) bis complex is coordinated to the K^+ ion through the two phenolates (O1A, O1B) and one of the carboxylates (O3A). The K^+ ion is connected to two such bis complexes. Thereby, the two Co(III) bis complexes sandwich the K^+ ion, as shown in Fig 3.1. One of the carboxylates (O4A) is in short contact with the neighbouring K^+ thereby forming a 2D polymeric chain. Some of the selected bond lengths and angles are given in table 3.2. The non-covalent interactions are given in table 3.3.

Table 3.2. Selected bond lengths and angles of complex **1**.

Complex	Co-Op	Co-Oc	Co-NH	K-Op	K-Oc	Op-Co-Op	Op-Co-Oc	Op-Co-NH
1	1.900(4)	1.886(3)	1.948(4)	2.920(4)	2.893(3)	82.67(16)	90.89(15)	93.79(16)
	1.904(4)	1.901(3)	1.964(4)	2.689(4)	2.810(4)		91.16(15)	175.40(2)

Op=phenolate, Oc=carboxylate, and NH=amine

Table 3.3. Non-covalent interactions in **1**.

D-H…A	D-H (Å)	H…A(Å)	D…A(Å)	DHA (°)
N1A- H1A…O2A	0.9800	2.4800	2.879(5)	104.00
N1A- H1A…O2B	0.9800	1.9100	2.863(3)	162.00
N1B-H1B…O2A	0.9800	2.0600	3.022(7)	165.00
N1B-H1B …O2B	0.9800	2.5800	2.939(6)	102.00
O2A-O2B…O1C	0.8200	2.3100	2.722(6)	112.00
O2B-H2B…O4A	0.8200	1.8200	2.621(6)	164.00
O1C-H1CB…O4B	0.8500	1.9300	2.722(6)	173.00

3.6. ESI-Mass spectrometry of the complexes

The spectra of **1** and **2** were recorded as *m/z* (ESI-MS,[M-H]$^-$). We found that the mass spectrum of complex **1** shows a molecular ion peak at 477.072 with a matching isotopic abundance pattern (Fig 3.2) of $[Co(L^{L\text{-}ser})_2]^-$. Similarly, complex **2** shows the molecular ion peak at 477.071 with a matching isotopic abundance pattern (Fig 3.3) of $[Co(L^{L\text{-}ser})_2]^-$. We could not get evidence of K^+ ion or Ba^{2+} ion binding with the complex in the solution at least in ESI-Mass.

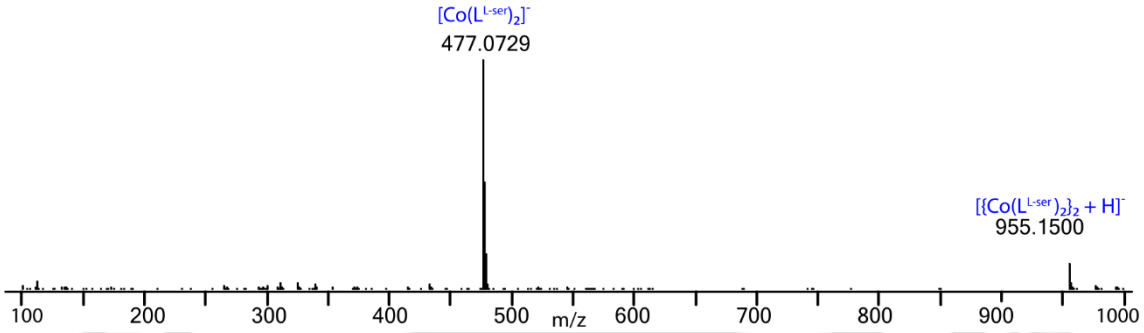

Figure 3.2. ESI-Mass spectra **1** (-ve) in DMF

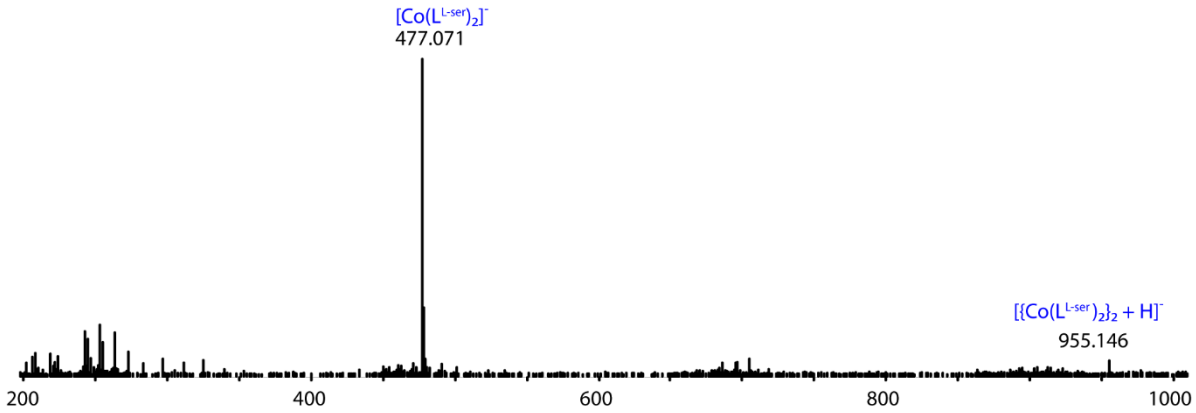

Figure 3.3. ESI-Mass spectra **2** (-ve) in DMF

Table 3.4. Mass spectral data.

	calc. m/Z (relative intensity)[b]	exp. m/Z (relative intensity)[b]
1	477.070(100), 478.070(23)	477.072(100), 478.072(28)
	479.070(4)	479.072(4)
2	477.070(100), 478.070(23)	477.071(100), 478.071(26)

479.070(4)	479.072(5)

[b] isotopic mass distribution of molecular ion peak with relative intensity values in parenthesis

3.7. NMR spectroscopy

The ^{1}H and ^{13}C NMR spectra of the ligand and all the complexes are well-defined, and their signals can be easily assigned according to their structures. Table 3.5 summarizes the NMR data for these complexes. ^{1}H NMR of the ligand $H_2L^{L\text{-ser}}$ and all its complexes was recorded in DMSO-d_6 at 500 MHz. Since some of the proton positions overlapped, we used the 2D ^{1}H NMR spectroscopic technique to assign all the respective protons' possible peak positions. The ^{1}H NMR of all the complexes **1**, **2**, and **3** are sharp and well-resolved resonance spectra, indicating the formation of complexes that are likely low-spin diamagnetic complexes. The assignment of protons and Carbon was additionally corroborated with the 2D-COSY spectra and HSQC spectra as some protons' positions overlapped. Here, we observe and assign the -OH and -NH peaks in the complex spectra, which are absent in the ligand spectra.

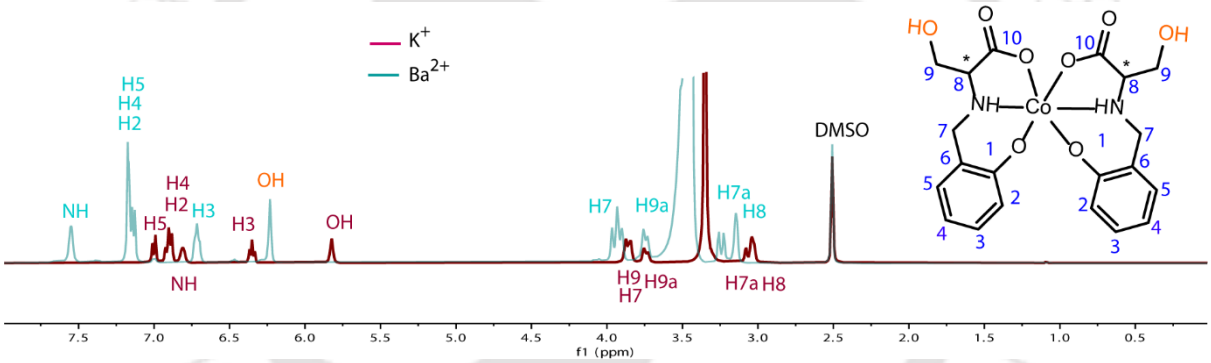

Figure 3.4. Combine ^{1}H NMR spectra of complex **1** and **2**

We compared the spectra of complexes **1** and **2**. We first compared the aromatic phenol protons labelled as 2, 3, 4, and 5 (Fig 3.4 and Table 3. 5). We found that all the complex **2** protons have a downfield shift, primarily the aromatic phenol protons shifted significantly. This is due to the higher charge of the secondary cation Ba^{2+} binding with the Co(III) bis complex, as the phenoxide electron charge density presumably decreases upon the coordination of the Ba^{2+} ion when compared to the K^{+} ion. Subsequently, we also check the protons around the coordination sites namely 7, 8, 9, and NH. We expect complex **2** to have a downfield shift for the same reason of cation binding, maybe not to the same extent as those aromatic phenolate protons, as the effect of secondary metal ions will be modest in the case of coordination sites protons. The higher charge secondary cations binding is one of the reasons for the sudden high downfield

shift (0.74 ppm) of NH and -OH (0.23 ppm) peaks, however, we can't rule out the possibility of Ba^{2+} interaction with the -NH and -OH groups due to its known higher coordination numbers. To understand further, we record the ^{1}H NMR spectra of complex **1** after adding solid $Al(NO_3)_3$ in the NMR tube. We observed that the addition of Al^{3+} does not produce a downfield shift as expected (Table 3.5).

Table 3.5. ^{1}H NMR peak position of the complexes

	phenol region				Coordination sites						
	H2	H3	H4	H5	H7	H7a	H8	H9	H9a	NH	OH
1	6.90	6.35	6.90	7.04	3.87	3.05	3.05	3.87	3.74	6.80	5.83
2	7.22	6.69	7.22	7.22	3.96	3.22	3.17	3.96	3.75	7.54	6.16
1-2	-0.33	-0.34	-0.33	-0.22	-0.09	-0.17	-0.12	-0.09	-0.01	-0.74	-0.33
Al^{3+}	7.01	6.49	6.98	7.23	3.83	3.10	3.08	3.94	3.71	7.14	6.09
1-(1+Al^{3+})	-0.11	-0.14	-0.09	-0.19	0.04	-0.05	-0.03	-0.07	0.03	-0.34	-0.23

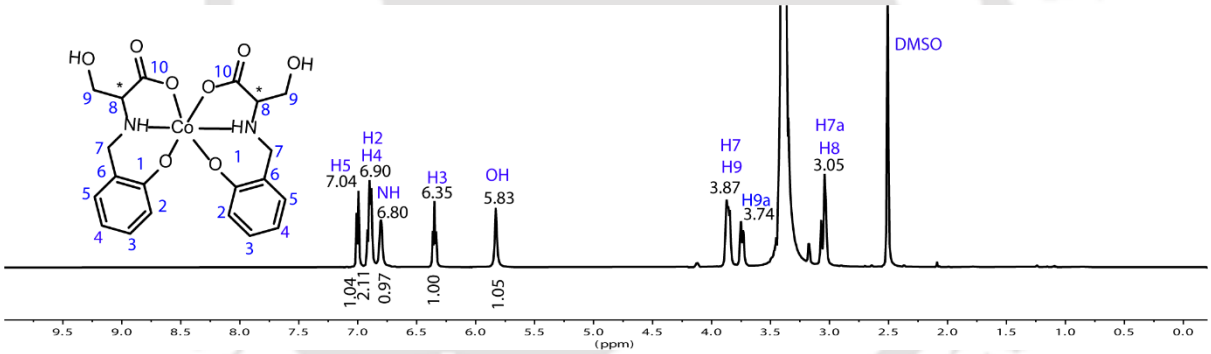

Figure 3.5. ^{1}H NMR spectra of complex **1**

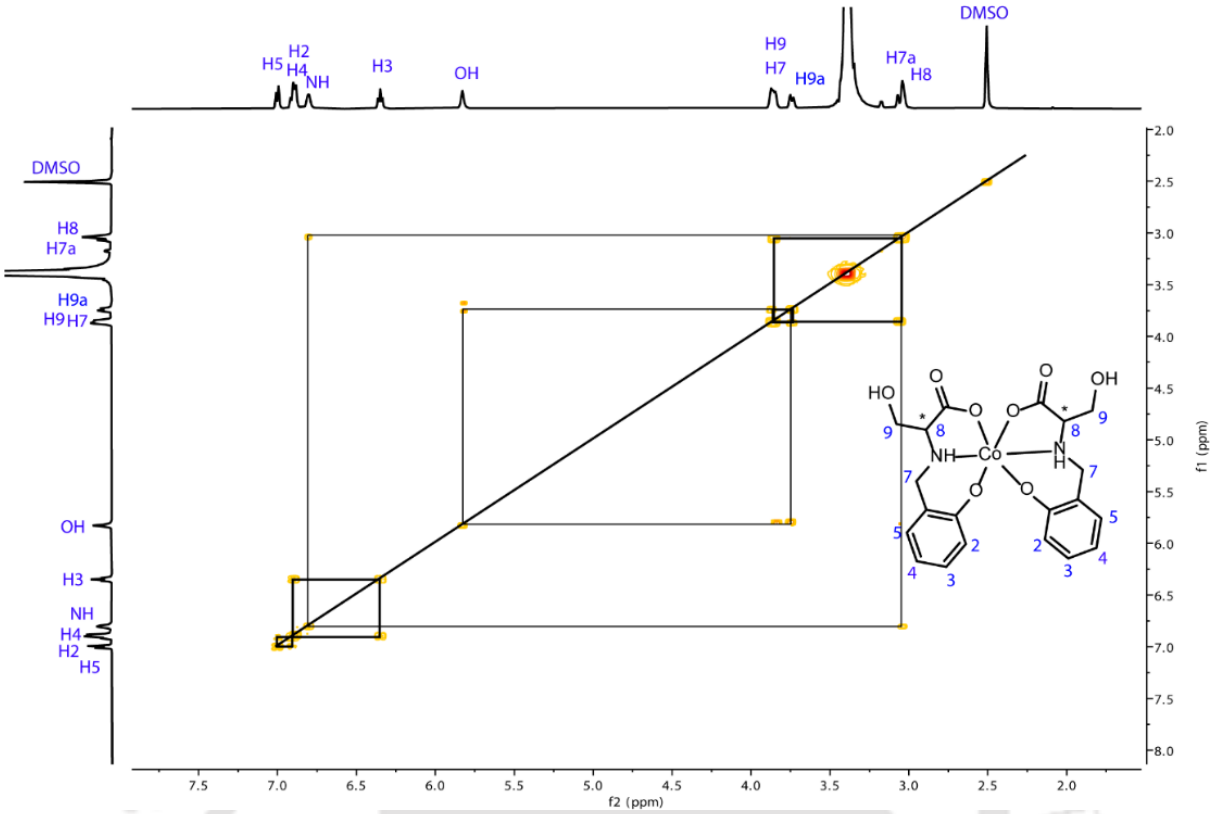

Figure 3.6. COSY spectra of complex **1**

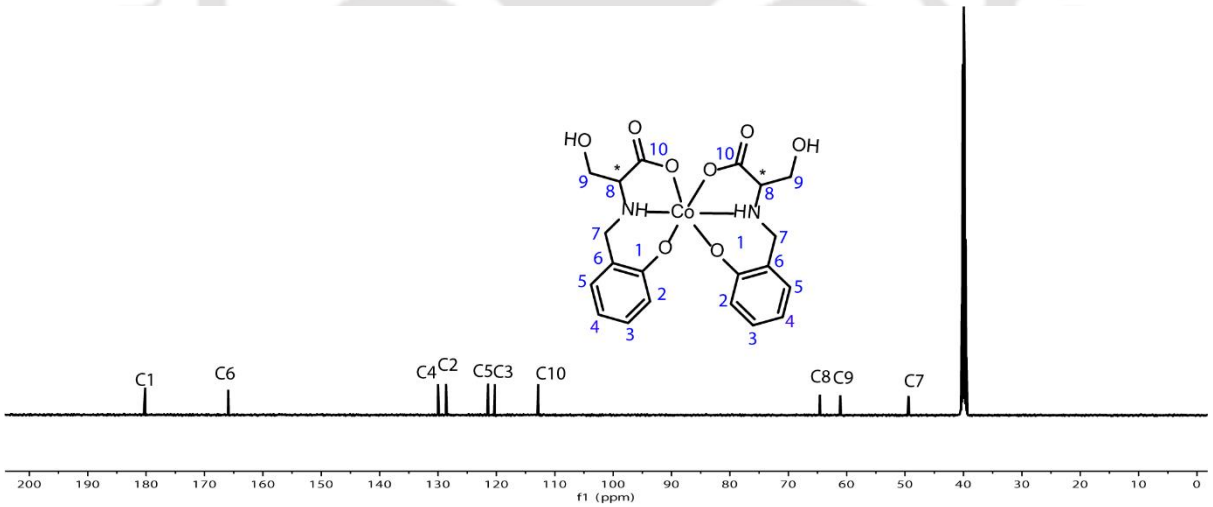

Figure 3.7. ^{13}C spectra of complex **1**

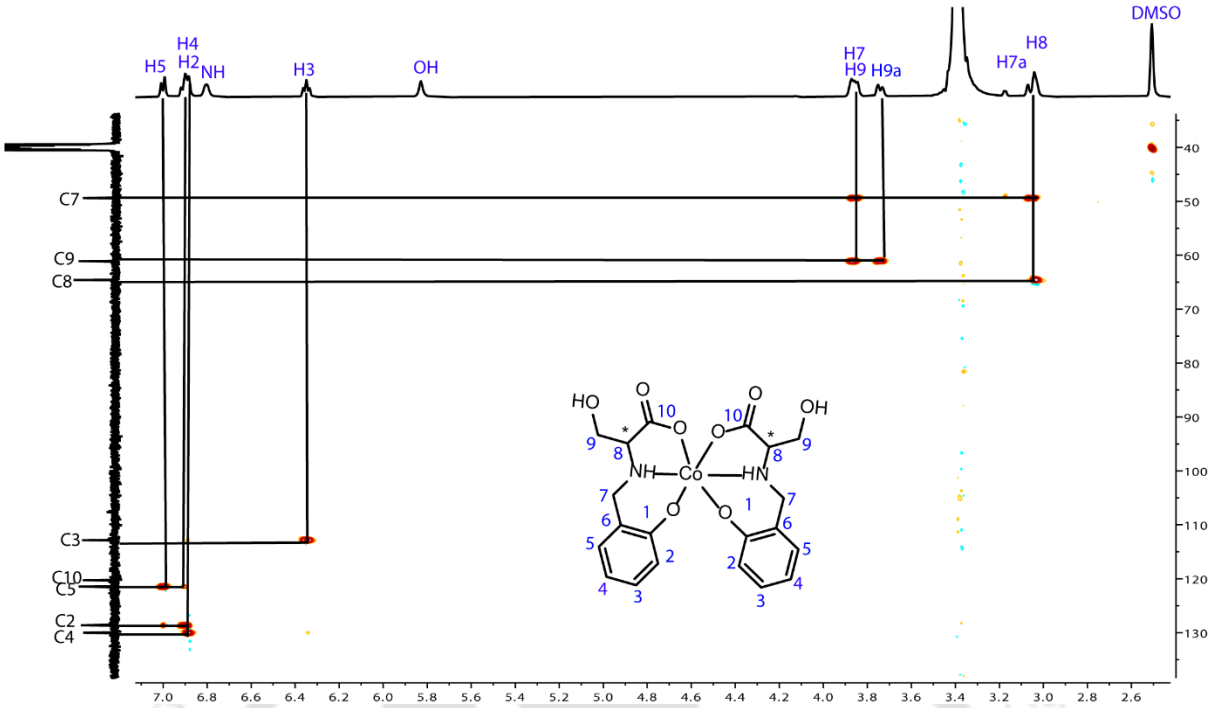

Figure 3.8. HSQC spectra of complex **1**

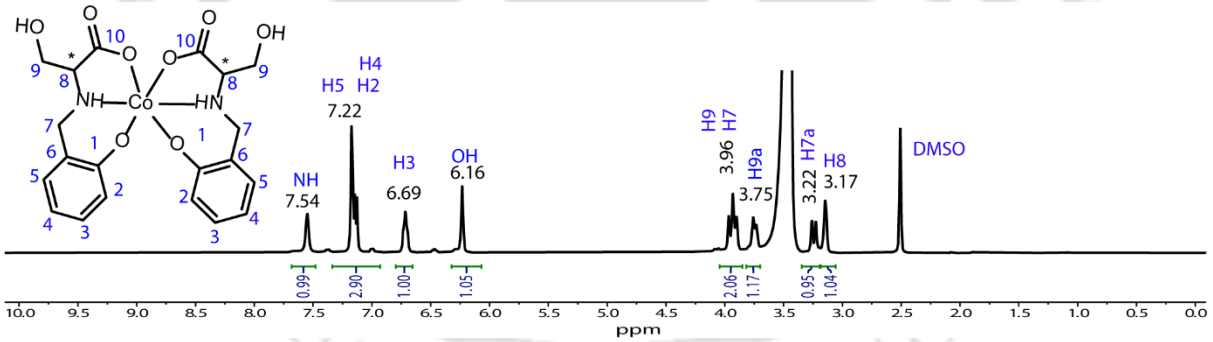

Figure 3.9. ^{1}H NMR of complex **2**

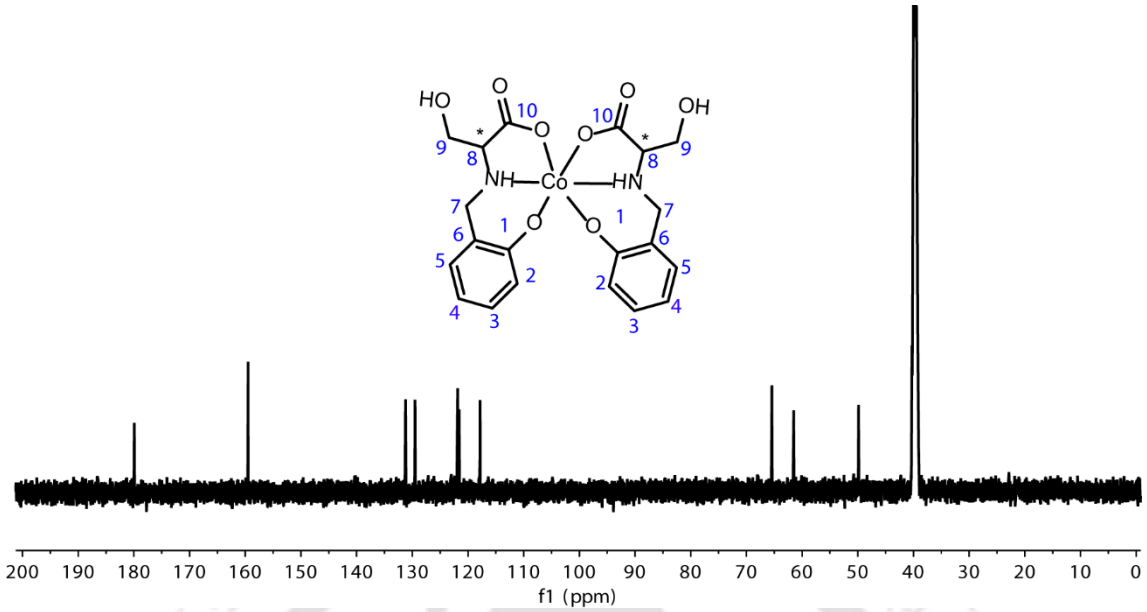

Figure 3.10. ^{13}C spectra of complex **2**

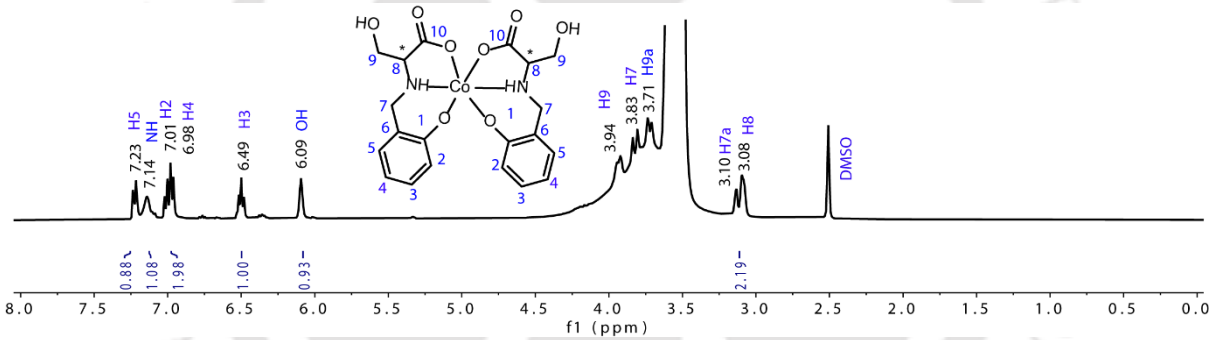

Figure 3.11. ^{1}H NMR of complex **1**+**Al**$^{3+}$

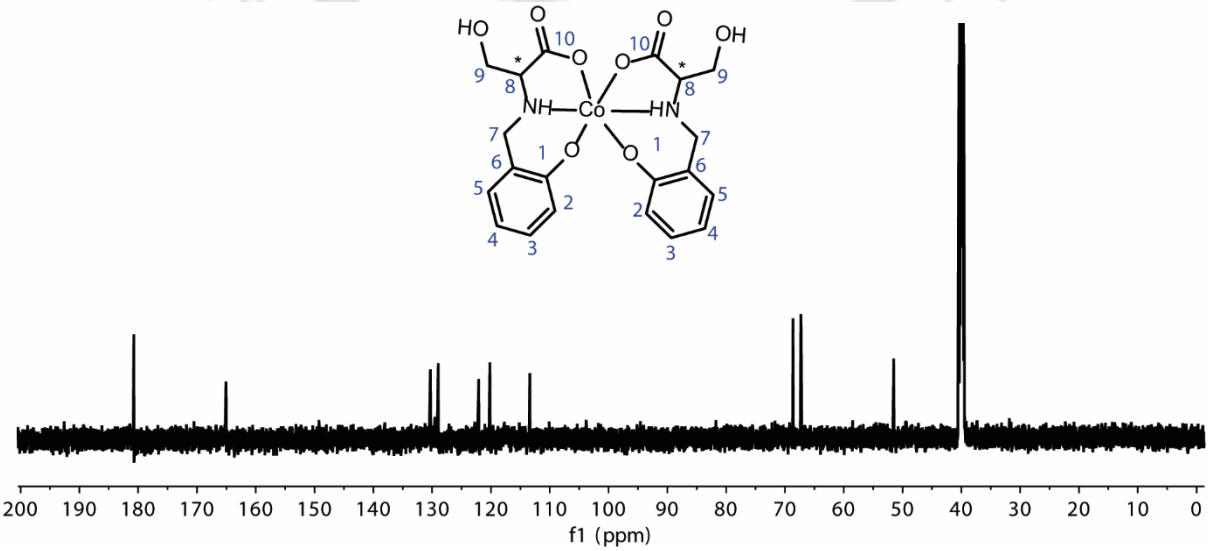

Figure 3.12. ^{13}C spectra of complex **1**+**Al**$^{3+}$

3.8. UV-visible spectroscopy

The UV-vis spectra of all the complexes are carried out in a DMF medium at room temperature. The electronic spectrum of each complex consists of a band at around ~350 nm. (ε = ~800). These bands are assigned as ligand-to-metal charge transfer transitions. In any low-spin Co(III) complex, two spins allowed d–d transitions. $^1A_{1g} \rightarrow {}^1T_{1g}$ and $^1A_{1g} \rightarrow {}^1T_{2g}$ are expected.[5,6] The band around 550 to 750 nm in the absorption spectrum of each complex may be attributed to one of these two expected transitions. The spin-allowed transition is obscured by a strong LMCT transition ~350 nm.[7]

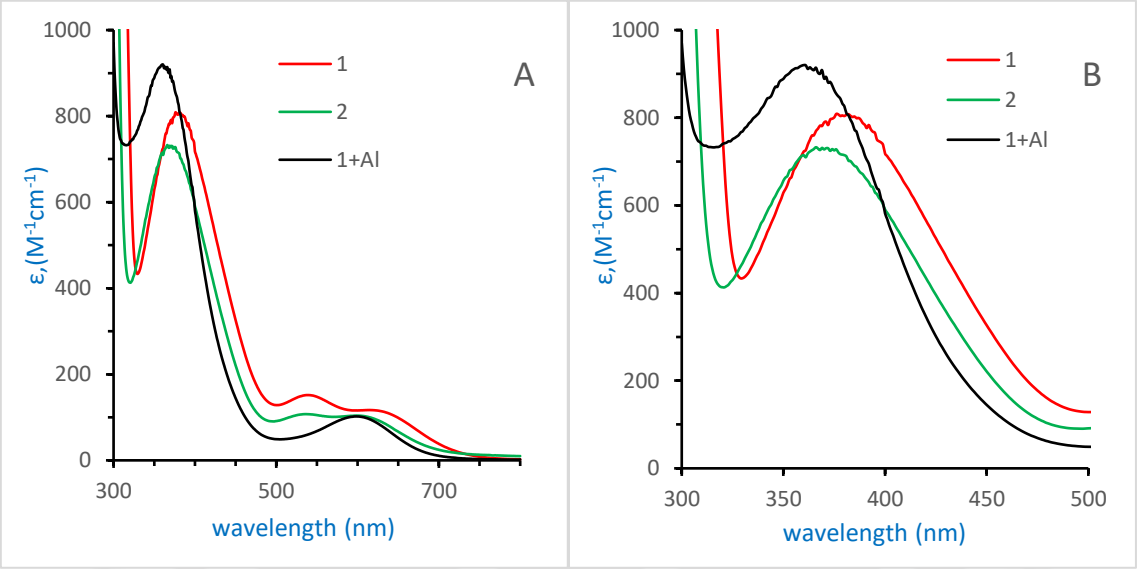

Figure 3.13. UV-visible spectra of complexes **1** and **2** and **1**+Al^{3+}

The electronic spectra are jointly presented in Fig 3.13. We studied the dependence of the λ_{max} values (i.e., charge transfer energies) on charge/ionic size for the heterobimetallic [Co(III), M]. The shift of the charge transfer energy to higher values (~10 nm) as we move from **1** to **2** can be ascribed to stabilizing the occupied orbitals on the metal. The stabilization of the metal-centred HOMO is achieved by the interaction of the Lewis acidic secondary metals with the bridging phenolate donors that are bound to the Co(III) centre.[8] The effect of the redox-inactive cations on the ligand-centred LUMO orbitals, however, must be more modest in comparison to the shifts induced at the Co(III) centre, with the net result of the widening of the HOMO-LUMO gap that drives the shifts in the charge transfer band energies.[9] As the anticipated change in donor power of the phenoxide ligands could be modelled as a shift in oxygen-centred charge density, it is unsurprising that the preferred descriptor for the changes in the UV-visible spectra is the polarising power of the incorporated secondary metal ions. We expect to have a

significant blue shift if Al^{3+} binds. Therefore, we add $Al(NO_3)_3$ in the solution of **1** and the d-d transition further shifted to higher energy.

Table 3.6. Electronic spectral data.[a]

Complex	**1**	**2**	**1+Al^{3+}**
λ_{max}, (ε, $M^{-1}cm^{-1}$)	386(798)	373(724)	364(910)
	625(95)	613(96)	600(101)

[a] Scan range in DMF, 200-800. ε values calculated using ~1 mM solutions.

3.9. Conclusion

In this chapter, we synthesized the proposed cyclic trinuclear by using an L-serine-derived ligand and Co(III) metal ions. We obtained Co(III) bis complex which has a different structural motif compared to Cu(II) bis complex. The Co(III) monomer obtained a facial octahedral geometry with the two phenolates in the *cis* orientation, which readily binds with K^+ to form a linear polymeric chain instead of a cyclic trinuclear. From the resultant linear polymeric chain, we replace K^+ with cations of higher charge and size Ba^{2+}. The complexes are diamagnetic. Hence we use ^1H NMR for characterization and rationalize and understand the effect of secondary cation polarising power-induced downfield shift. However, the ^1H NMR spectra of the complex upon the addition of Al^{3+} do not show a downfield shift as expected. We tried to understand and explain in chapters IV and V.

3.10. References

1 M. Dubey, R. R. Koner and M. Ray, *Inorg. Chem.*, 2009, **48**, 9294–9302.

2 D. C. Lacy, Y. J. Park, J. W. Ziller, J. Yano and A. S. Borovik, *J. Am. Chem. Soc.*, 2012, **134**, 17526–17535.

3 R. R. Golwankar, A. Kumar, V. W. Day and J. D. Blakemore, *Chem. – Eur. J.*, 2022, **28**, e202200344.

4 M. Dubey, R. R. Koner and M. Ray, *Inorg. Chem.*, 2009, **48**, 9294–9302.

5 A. Banerjee, D. Das, P. P. Ray, S. Banerjee and S. Chattopadhyay, *Dalton Trans.*, 2021, **50**, 1721–1732.

6 S. Chattopadhyay, G. Bocelli, A. Musatti and A. Ghosh, *Inorg. Chem. Commun.*, 2006, **9**, 1053–1057.

7 C.-Y. Su, S. Liao, M. Wanner, J. Fiedler, C. Zhang, B.-S. Kang and W. Kaim, *Dalton Trans.*, 2003, 189–202.

8 R. R. Golwankar, A. Kumar, V. W. Day and J. D. Blakemore, *Chem. – Eur. J.*, 2022, **28**, e202200344.

9 A. Kumar, D. Lionetti, V. W. Day and J. D. Blakemore, *Chem. – Eur. J.*, 2018, **24**, 141–149.

भारतीय प्रौद्योगिकी संस्थान गुवाहाटी
Indian Institute of Technology Guwahati

Chapter IV

Water-soluble chiral coordination polymers of Li^+, Na^+, K^+, and Ba^{2+} with an anionic Fe(III) complex of L-threonine derivative and significant red shift of visible spectra with Al^{3+} salt

4.1. Introduction

Coordination polymers with porous structures or Metal-organic framework (MOF) can trap molecules or reagents within them, and they are helpful in multiple areas of chemistry.[1–10] Being a coordination polymer, many with aromatic organic ligands, most are insoluble and cannot be recrystallized. Thus, it can either not release the trapped molecule or be reassembled with fresh inclusions. This resulted in the exploration of water-soluble MOFs.[11-16] Another interesting direction is synthesizing coordination-driven self-assembly of metal−organic complexes (MOCs), which retain their multinuclear structures in solution.[15,17-22] In this regard, Zn(II) and alkali ions bridging between smaller units in both types of materials seem feasible.[16, 23-25] Thus, a complex that can bind alkali metal ions to form a network can be a starting point. If it forms a three-dimensional network, it might be able to generate porous structures necessary for trapping reagents. The aqueous solubility can occur either because of the bridge's dissolution or the bridge's hydrophilicity. The Ni(II) and Cu(II) complexes of reduced Schiff bases of salicylaldehyde and amino acids have shown a tendency to bind alkali metal ions[21,22] reminiscent of cryptands[23–26] or metallacrown[27–29] through the carboxylates and phenolates.[22] However, the shape of the complex used previously promoted trinuclear assembly but not a network.[30,32] Here, we choose to work with Fe(III) and L-threonine-based ligand to change the shape of the complex and make it anionic to facilitate the binding of alkali or alkaline earth ions as countercations. We also hoped that the alcoholic side arm of L-threonine would increase the solubility of the complexes.

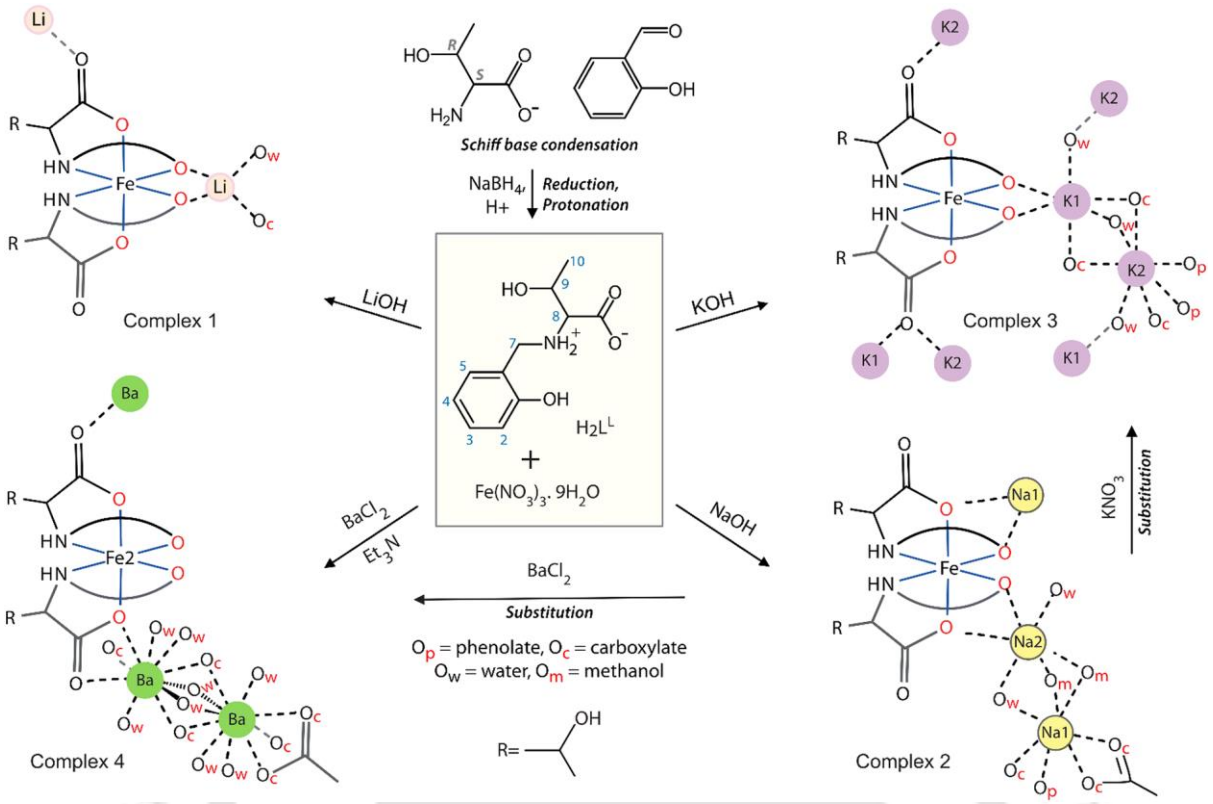

Scheme 4.1. syntheses of the complexes

4.2. Experimental

4.2.1. Materials and methods

Salicylaldehyde was purchased from Aldrich Chemical Co. L-threonine, LiOH• H_2O, and $NaBH_4$ from Sisco Research Laboratories Pvt. Ltd. (SRL), India, and used as received. Solvents were obtained from commercial sources and used without further purifications unless otherwise stated. MilliQ purified the water used. The FTIR spectra were recorded on a Perkin-Elmer Spectrum-One FT-IR spectrophotometer with KBr discs in the range 4000-400 cm^{-1}. UV-vis spectra were recorded on PerkinElmer Lambda 365^{+} UV-vis spectrophotometer.NMR (^{1}H, ^{13}C, and COSY) spectra were recorded on Bruker 500 MHz spectrometers using d_6-DMSO (Sigma Aldrich Chemical Co.) as the solvent and Me_4Si as an internal standard. Chemical shifts (δ) and the spin-spin coupling constant (*J*) are reported in ppm and in Hz, respectively. Electrospray Ionization mass (ESI-MS) spectra were recorded on an Agilent 6520 Q-TOF LC/MS mass spectrometer. Solid-state magnetic susceptibility of the complexes at room temperature was recorded using Sherwood Scientific Magnetic Balance MSB-1.[34] Diamagnetic corrections were calculated using standard values.[35] Elemental analyses were done using a ThermoFisher Scientific Flash smart V CHNS/O analyzer.

4.3. Syntheses

4.3.1. $H_2L^{L\text{-}thr}$. The amino acid L-threonine (2.00 g, 16.8 mmol) and LiOH• H_2O (0.71 g, 16.8 mmol) was dissolved in 25 mL of methanol and stirred for 10 min, which gave a colourless solution. The methanolic solution of salicylaldehyde (2.05 g, 16.8 mmol) was added dropwise to the above solution. The solution turned yellow immediately. The solution was stirred for 2 h, and solid $NaBH_4$ (0.8 g, 21.1 mmol) was added portion-wise. The solution turned colourless within a few minutes. It was stirred for another 1 h, and the solvent was removed using a rotary evaporator. The solid obtained was dissolved in ~5 mL of water and acidified to pH 6-7 using dil HCl. The water was removed using a rotary evaporator. The sticky solid was dissolved in MeOH and kept for crystallization. Block-shaped crystals were obtained after three days. The white crystals obtained were washed using acetone, collected, and dried under a vacuum desiccator. Yield 2.64 g (69.8%). ^{1}H NMR [$H_2L^{L\text{-}thr}$] (DMSO-d_6, 500 MHz ppm) 1.18 (d, 3H, H^{10}, J=10 Hz), 3.06 (m, 1H, H^8, J=5 Hz), 3.90 (m, 1H, H^9, J=10 Hz), 4.05 (d, 1H, H^{7a}, J =15 Hz), 4.05 (d, 1H, H^7, J =15 Hz), 6.78 (t, H, H^4 J= 7.5 Hz), 6.80 (t, H, H^2 J= 7.5 Hz), 6.91 (d, 1H, H^3, J =8 Hz), 7.25 (d, 1H, H^5, J =7.5 Hz). FTIR (KBr, cm^{-1}) ν $(COOH)_{asym}$ 1615 (s), 1492 (s), ν $(COOH)_{sym}$ 1407 (m). m/z (ESI-MS $[H_2L^{L\text{-}thr}+H]^+$); calcd: 226.10 found 226.10.

4.3.2. [Li{Fe($L^{L\text{-}thr}$)$_2$}(H_2O)]• H_2O (1). The Ligand $H_2L^{L\text{-}thr}$ (0.200 g, 0.88 mmol) and LiOH • H_2O (0.74 g, 1.76 mmol) were mixed in 25 mL of MeOH, which gave a clear solution. After stirring for 5 min, we added $Fe(NO_3)_3$• $9H_2O$ (0.180 g, 0.44 mmol) and stirred for another 2 h. The solvent was removed using a rotary evaporator. The red solid obtained was collected and washed with ethyl acetate. The solid was dissolved in MeOH and kept for crystallization. After 2 days, the needle-shaped red crystals were obtained. The crystals were collected and washed with ethyl acetate and kept them in a vacuum desiccator. Yield: 0.169 g (69.8%). FTIR (KBr, cm^{-1}): ν $(COOH)_{asym}$ 1626 (s), 1484 (m), $(COOH)_{sym}$ 1454 (s). (ESI-MS): m/z $[Fe(L^{L\text{-}thr})_2]^-$; calcd: 502.105 found 502.104, $[Li\{Fe(L^{L\text{-}thr})_2\}$ -H$]^-$; calcd: 514.105 found 514.104. μ_{eff} (powder, 298, K); 5.89 μB/Fe. Anal. Calcd for [Li{Fe($L^{L\text{-}thr}$)$_2$}(H_2O)]: C, 50.11, H, 5.35, N, 5.31. Found: C, 50.01, H, 5.28, N, 5.34.

Note. For elemental analysis, the crystalline samples were powdered and dried under a vacuum desiccator for several days before analysis. Thus, the number and type of solvent molecules in

the crystal structure and isolated product differ. We used the formula weight of the bulk for solution concentration and magnetic moment calculation.

4.3.3. $[Na_2\{Fe(L^{L\text{-}thr})_2\}_2(MeOH)_2(H_2O)_2]\bullet$ 3MeOH (2). It was synthesized by mixing $H_2L^{L\text{-}thr}$ (0.200 g, 0.88 mmol) and solid NaOH (0.07 g, 1.76 mmol) in 25 mL of MeOH, which gave a clear solution. After stirring for 5 min, we added $Fe(NO_3)_3\bullet 9H_2O$ (0.180 g, 0.44 mmol) and stirred for another 2 h. The solvent was removed using a rotary evaporator. The red solid obtained was collected and washed with ethyl acetate. The solid was dissolved in MeOH and kept it for crystallization. After 2 days, the needle-shaped red crystals were obtained. The crystals were collected, washed with ethyl acetate, and kept in a vacuum desiccator. Yield: 0.118 g, (51.7%). FTIR (KBr, cm^{-1}): ν $(COOH)_{asym}$ 1626 (s), 1484 (m), $(COOH)_{sym}$ 1453 (s). (ESI-MS): m/z, $[Fe(L^{L\text{-}thr})_2]^-$); calcd: 502.105 found 502.105. 6.04 μB/Fe. Anal. Calcd for $[Na_2Fe_2(L^{L\text{-}thr})_4(H_2O)_4MeOH]$: C, 46.81, H, 5.59, N, 4.85. Found: C, 46.76, H, 5.69, N, 4.80.

Alternatively, we took **1** (0.2 g, 0.43 mmol) and $NaNO_3$ (0.037 g, 0.43 mmol) in a round bottom flask and dissolved them in 15 mL of Milli-Q water, which gave a red solution. We stirred for 2 hrs, and the solution was kept for slow evaporation. After 2 days, needle-shaped crystals were obtained. We collected the crystal wash with acetone and dried it under a vacuum desiccator. Yield: 0.182 g (79.8%). FTIR is identical to the product from the first method.

4.3.4. $[K_2\{Fe(L^{L\text{-}thr})_2\}_2(H_2O)_2]\bullet$ MeOH (3). We took the complex **2** (0.2 g, 0.43 mmol) and KNO_3 (0.044 g, 0.43 mmol) in a round bottom flask and dissolved them in 15 mL of Milli-Q water, which gave a red solution. We stirred for 2 hrs, and the solution was kept for slow evaporation. After 2 days, needle-shaped crystals were obtained. We collected the crystal wash with acetone and dried it under a vacuum desiccator. Yield: 0.168 g (91.3%). FTIR (KBr, cm-1): ν $(COOH)_{asym}$ 1626 (s), 1484 (m), (COOH)sym 1455 (s). (ESI-MS): m/z $[Fe(L^{L\text{-}thr})_2]$-; calcd: 502.105 found 502.103, μ_{eff} (powder, 298, K); 5.92 μB/Fe. Anal. Calcd for $[K_2Fe_2(L^{L\text{-}thr})_4(H_2O)_2MeOH]$: C, 46.96, H, 5.25, N, 4.87. Found: C, 46.89, H, 5.22, N, 4.60.

Alternatively, $H_2L^{L\text{-}thr}$ (0.2 g, 0.88 mmol) and KOH (0.10 g, 1.76 mmol) were dissolved in 15 mL of MeOH, which gave a clear solution. Fe(NO3)3• 9H2O (0.180 g, 0.44 mmol) was added to the above solution. The solution turned red immediately. We stirred for 3 hrs, and the red solid precipitated out. The red solid was filtered using a G4 crucible and washed with acetonitrile. The red solid was dissolved in 8 mL of Milli-Q water and kept for slow evaporation. After 2 days, needle-shaped crystals were obtained. We collected the crystal wash

with acetone and dried it under a vacuum desiccator. Yield: 0.129 g (50.5%). FTIR is identical to the product from the first method.

4.3.5. $[Ba_2\{Fe(L^{L\text{-}thr})_2\}_3(H_2O)_{10}]Cl\bullet MeOH\bullet 3H_2O$ (4). We took complex **2** (0.2 g, 0.43 mmol) and $BaCl_2\bullet 2H_2O$ (0.10 g, 0.43 mmol) in a round bottom flask and dissolved in 15 mL of Milli-Q water, giving a red solution. We stirred for 2 hrs, and the solution was kept for slow evaporation. The block-shaped red crystal was obtained After three days. The crystals were collected, washed with acetone, and dried under a vacuum desiccator. Yield: 0.174 g (75.9%). FTIR (KBr, cm^{-1}): ν $(COOH)_{asym}$ 1608(s), 1480 (m), $(COOH)_{sym}$ 1451 (s). (ESI-MS): m/z $[Fe(L^{L\text{-}thr})_2]^-$; calcd: 502.105 found 502.104 μ_{eff} (powder, 298, K); 5.90 μB/Fe. Anal. Calcd for $[Ba_2Fe_3(L^{L\text{-}thr})_6(H_2O)_{10}Cl]$: C, 39.65, H, 5.07, N, 4.14. Found: C, 39.58, H, 4.72, N, 4.47.

Alternatively, Ligand $H_2L^{L\text{-}thr}$ (0.200 g, 0.88 mmol) and $Et_3NH\bullet H_2O$ (0.177 g, 1.76 mmol) were mixed in 25 mL of MeOH, which gave a clear solution. After stirring for 5 min, we added $Fe(NO_3)_3\bullet$ 9H2O (0.180 g, 0.44 mmol) and stirred for another 2 h and $BaCl_2.2H_2O$ (0.214 g, 0.88 mmol) was added to the above solution. We stirred for 3 hrs, and the red solid precipitated out. We filtered the red solid using a G4 crucible and washed it with acetone, and we dissolved the red solid in 5 mL of Milli-Q water for crystallization. The block-shaped red crystal was obtained After 3 days. The crystal was collected, washed with acetone, and dried under a vacuum desiccator. Yield: 0.166 g (67.9). FTIR is identical to the product from the first method.

4.4. X-ray Crystallography

The crystal of the complexes obtained during synthesis was used for X-ray analysis. The crystals were mounted on glass fibre. All geometric and intensity data for crystals **1**, **3**, and **4** were collected at room temperature using a Bruker SMART APEX CCD diffractometer equipped with a fine focus 1.75 kW sealed tube Mo-Kα (λ= 0.71073 Å) X-ray source, with increasing ω (width of 0.3º per frame) at a scan speed of either 3 or 5 s/frame. The SMART software was used for data acquisition and the SAINT software for data extraction. Absorption corrections were done using a multi-scan. For crystal **2,** the intensity data were collected at room temperature using a single Source Super Nova CCD System from Agilent Technologies equipped with a fine focus 1.75 kW sealed tube with Mo-Kα radiation. The data were reduced using CrysAlis RED.[30] The structure solution and refinement were performed on the WinGX environment using the SHELXS97 SHELXL97 programs.[31] All non-hydrogen atoms were refined anisotropically. The hydrogen atoms were located from the Fourier maps and refined

isotropically wherever possible. Thus, some C-H bonds will not be ideal and may vary. Most hydrogen atoms attached to the solvent molecules could not be located or fixed, so the molecular weight may not match. ORTEP obtained selected crystallographic data summarized in Table 4.1. A perspective view of the complex was obtained by ORTEP.[32]

Table 4.1. Crystal Data of the complexes.[a]

Compounds	**1**	**2**	**3**	**4**
Empirical formula	$C_{22}H_{26}FeLiN_2O_{10}$	$C_{49}H_{72}Fe_2N_4Na_2O_{23}$	$C_{45}H_{49}Fe_2K_2N_4O_{19}$	$C_{68}H_{78}Ba_2Cl\ Fe_3\ N_6O_{40}$
M	541.24	1242.78	1139.79	2097.04
Wavelength (Å)	0.71073	0.71073	0.71073	0.71073
Crystal system	orthorhombic	orthorhombic	monoclinic	monoclinic
Space group	*P* 2_1 2_1 2_1	*P* 2_1 2_1 2_1	*P* 2_1	*C* 2
a, Å	7.6475(5)	14.0394(4)	7.8208(11)	27.067(7)
b, Å	17.5134(11)	17.8936(5)	17.044(2)	13.513(3)
c, Å	19.0088(12)	23.9512(7	19.280(3)	12.427(2)
α, deg	90.00	90.00	90.00	90.00
β, deg	90.00	90.00	94.509(4)	101.042(11)
γ, deg	90.00	90.00	90.00	90.00
V, Å^3	2545.9(3)	6016.9(3)	2562.0(6)	4461.1(17)
Z	4	4	2	2
ρ, g cm^{-3}	1.412	1.372	1.477	1.543
μ, mm^{-1}	0.648	0.575	0.806	1.465
FLACK para		-0.048(48)	0.077(23)	0.117(10)
Reflections collected	5231	12145	6273	2783
Independent reflections	4955	9946	5952	2721
GOF	1.116	0.857	1.162	1.117
Final *R* indices [*I* >2σ(*I*)]	*R*1 = 0.0289	*R*1 = 0.0441	*R1* = 0.0340	*R*1 = 0.0488
	*wR*2 = 0.0760	*wR*2 = 0.1111	*wR*2 = 0.0891	*wR*2 = 0.1402
R indices (all data)	*R*1 = 0.0317	*R*1 = 0.0597	*R*1 = 0.0396	*R1* = 0.0508
	*wR*2 = 0.0782	*wR*2 = 0.1254	*wR*2 =0.1014	*wR*2 = 0.1453

[a]Refinement method: full-matrix least-squares on F^2.

4.5. Results and discussion

4.5.1. Syntheses and characterization

The synthesis of the ligand, a reduced Schiff Base of salicylaldehyde and L-threonine, is similar to analogous amino acid-based ligands reported earlier.[30-32,39,40] The only difference is that the current ligand is more soluble in water and does not precipitate from water. A recrystallization from the methanol was necessary. The identity of the ligand was confirmed by its ^{1}H NMR, ESI-Mass and FTIR spectra (experimental section). Complex **1** was synthesized directly from the ligand, iron(III) salt, and LiOH in Methanol. LiOH acts as a base deprotonating ligand and a counter ion. Complexes **2** to **4** were synthesized directly using corresponding bases or a combination of base and barium salt (Scheme I). Alternatively, **3** and **4** could be synthesized by metathesis of **2** with potassium or barium salts, respectively. Synthesis works equally well either in water or Methanol (Experimental Section). All four complexes are red in colour due to the formation of the iron(III) complex. The FTIR spectra of the complexes (Fig. S5 - S8) are sharp and nearly identical because of their similarity in structure. They show strong and sharp asymmetric carboxylate stretches 1600-1628cm^{-1}, the same region where reported complexes with similar ligands (1580-1630 cm^{-1}) were observed. All four complexes are soluble in water and methanol and could be recrystallized in crystalline form from either of the solvents. The crystals were dried inside a vacuum desiccator for several days before analysis and bulk measurements. The elemental analysis results are in the experimental section. The number of solvents in the bulk and crystal structure differs. The formula from the analysis was used for experiments on the bulk. The solid-state room temperature magnetic moments of **1**-**4** are close to the ideal 5.92 BM value expected for the high-spin Fe(III) complex.[41]

4.5.2. Crystal structures

All the complexes are structurally characterized, and the structural parameters are in Table 3.1. Selected bond lengths and angles are compared in Table 3.2. Needle-shaped red crystals of **1** was obtained from Methanol. The structure was solved in the $P2_12_12_1$ space group. The ORTEP diagram and selected bond length and angles are in Figure 4.1 and Table 4.1 and 4.2. The asymmetric unit comprises one octahedral *bis*-iron(III) complex, one lithium counter ion, and two water molecules. The octahedral iron(III) complex is coordinated by two $(L^{l\text{-}thr})^{2-}$ ligands, each acting as a facial tridentate ligand. Each ligand has three chiral centres at C8A, C9A, and N1a with *S*, *R*, and *R* configurations, respectively.

Table 4.2. Selected bond distances (Å) and angles (°).[a]

	1	**2**[b]		**3**[b]		**4**[b]	
		Fe1	*Fe2*	*Fe1*	*Fe2*	*Fe1*	*Fe2*
Fe-O_p	1.916(2), 1.932(2)	1.927(3), 1.902(3)	1.903(3), 1.927(4)	1.904(5), 1.908(5)	1.910(4), 1.914(5)	1.899(16), 1.899(16)	1.907(15), 1.907(15)
Fe-O_c	2.016(2), 2.012(2)	2.034(3), 2.012(3)	1.991(3), 2.004(3)	2.024(6), 2.019(4)	2.015(5), 2.024(5)	2.046(16), 2.046(16)	2.023(16), 2.023(16)
Fe-N_a	2.169(2), 2.192(2)	2.191(4), 2.221(4)	2.194(4), 2.210(4)	2.162(5), 2.216(6)	2.168(5), 2.203(6)	2.195(17), 2.195(17)	2.200(14), 2.200(14)
O_c-Fe-O_c	160.14(9)	168.71(13)	170.01(13)	163.9(2)	163.9(2)	167.5(7)	166.6(7)
O_p-Fe-O_p	86.04(9)	93.60(13)	96.50(13)	95.1(2)	96.3(2)	97.5(7)	97.9(7)
N_a-Fe-N_a	92.87(9)	87.42(13)	86.04(13)	87.7(2)	88.1(2)	85.6(6)	84.4(6)
M-O_p	1.999(6), 2.026(6)		2.398(4)	2.679(6), 2.717(6)	2.697(5), 2.692(6)		
M-O_c	1.922(2)	2.555(3), 2.398(4)	2.332(4)	2.805(6), 2.665(6)[c], 2.849(6)[c]	2.665(6)[c], 2.849(6)[c]	3.052(15)[c], 2.936(19), 3.027(15)	3.052(15)[c], 2.936(19), 3.027(15)
M-O_{water}	1.897(6)	2.451(3)[c]	2.451(3)[c] 2.365(5)	2.803(6), 2.719(6)[c]	2.840(6), 2.719(6)[c]	2.819(16)[c], 2.75(2), 2.89(2)	2.819(16)[c], 2.75(2), 2.89(2)
M-$O_{methanol}$		2.409(6)[c], 2.419(4)[c]	2.409(6)c, 2.419(4)c				
M…M	-	3.320[d]		3.939[d]		4.283[d]	

[a] Subscript *p* and *c* on the oxygen atom and *a* in the N atom denote phenolate, carboxylate, and amine respectively. [b] *Fe1* and *Fe2* denote two non-identical Fe units in structures of **2** - **4**. [c] Bridging oxygen atoms. [d] Calculated using Mercury software.

This phenomenon of opposite conformation preference at chiral carbon C8A and amine N1A has been observed in all the characterized complexes of this type of ligand.[30-32,39,40] The deviation of bond angles from ideal 90° and 180° (Table 4.2) indicates that the geometry is slightly distorted. Especially, the axial $Fe_{carboxylate}$-Fe-$O_{carboxylate}$ angle at 160.14(9)° (O2a-Fe-O2b in Fig. 4.1) is significantly distorted from ideal 180°. The Fe-N_{amine} bond lengths (FeN1a, 2.169(2) Å) is longer than ether Fe-$O_{carboxylate}$ (Fe-O2b, 2.012(2) Å) or Fe-$O_{phenolate}$ (Fe-O1b 1.932(2) Å). The order and lengths are similar to the reported iron(III) complex with L-histidine analogue ligand (Fe-N_{amine}, ~2.20 Å, Fe-$O_{carboxylate}$ ~1.99 Å and Fe-$O_{phenolate}$ ~1.94 Å).[39,40,42] Incidentally. There are only two iron(III) structures reported[39,42] with amino acid-based reduced Schiff base ligands even through numerous structures exist with other metal ions. The counter ion Li^+ binds with the cis-oriented phenolates in a tetrahedral fashion where a water molecule and the carboxylate of the neighbouring bis complex complete the tetrahedral geometry. The intermolecular binding of Li^+ results in a one-dimensional chain along the *a*-axis of the crystal. The water (O10) coordinated to Li^+, one lattice water(O20), carboxylate oxygen (O3b), and one of the threonine oxygens (O4b) formed an intermolecular H-bonded network that stitches the linear chains together. The carboxylate O2b and the other oxygen (O4a) also form an intermolecular H-bond (length). Thus, crystals of **1** has a one-dimensional chain formed by the coordination of Li^+ to two neighbouring octahedral iron(III) complex (Fig 4.2A).

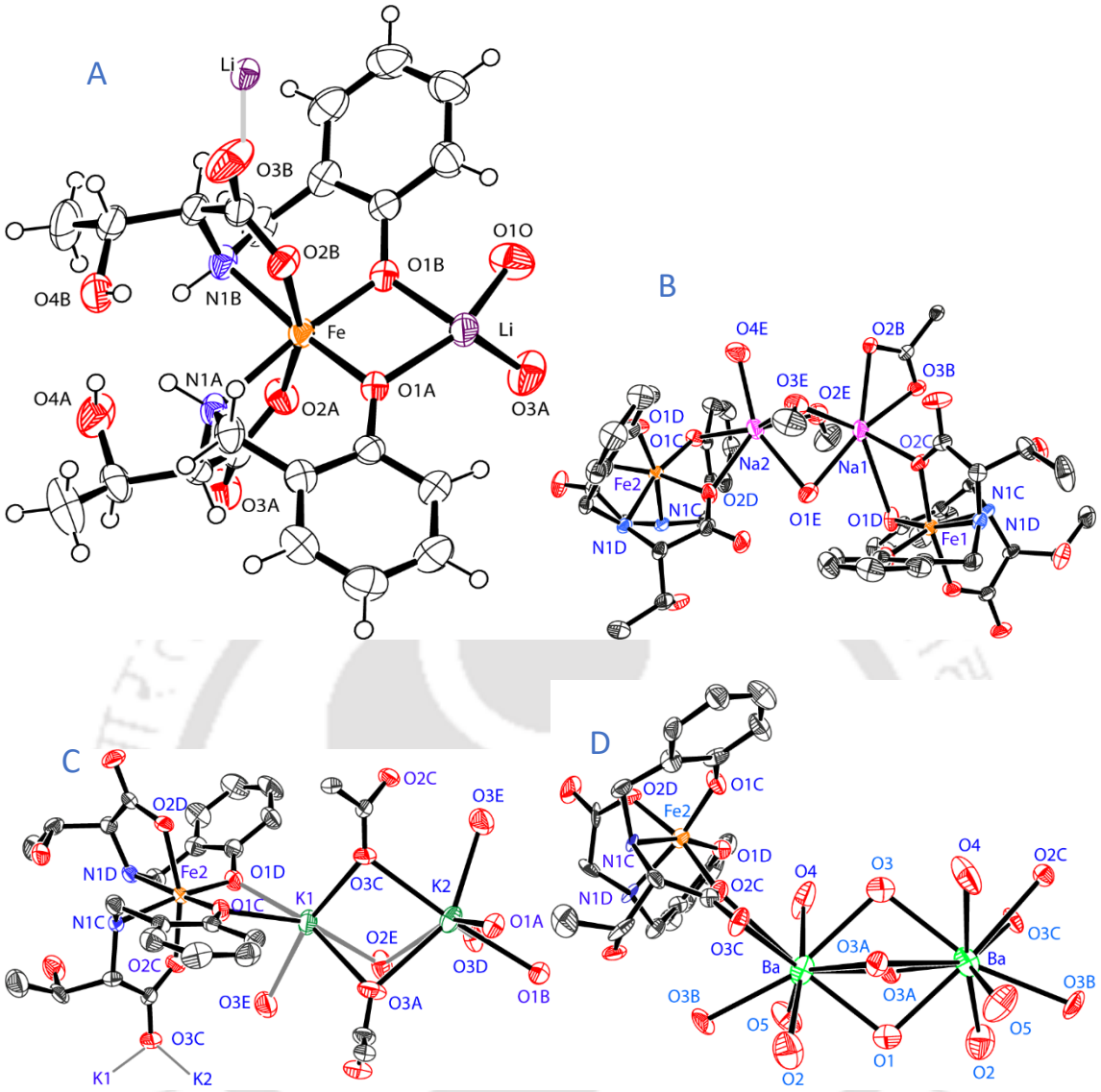

Figure 4.1. ORTEP diagram of Complex **1**, **2**, **3**, and **4** with thermal ellipsoid set at 50 % probability

Complex **2** crystallized in the chiral space group *P* 2_1 2_1 2_1. The asymmetric unit contains two Fe(III) bis complexes, two Na^+, one water, and five MeOH molecules. The geometry and bond parameters of the iron(III) complex are nearly identical to the *bis*-complex unit on **1** (Table 4.2). The sodium ions are coordinated to phenolate and carboxylate oxygens of iron(III) complex on one side. Conversely, two non-equivalent sodium ions are connected through bridges formed by two methanol and one water. Bridged structures for sodium ions have been seen before[43] but are not common in hetero bimetallic complexes like the present system. The coordination environment around the two Na^+ differs (Fig. 4.1B). The Na1 is hepta coordinated by three bridging solvent oxygen, a bidentate carboxylate (Na1-O2b/O3b, 2.555(3)m /2.398(4)

Å), a monodentate carboxylate (Na1-O2C, 2.332(4) Å), and a long phenolate (Na1-O1d, 2.942 Å). Other than the three bridging solvents, the Na2 is hexa coordinated by two cis-oriented phenolates (2.450(4) & 2.398(4) Å, and one terminal water molecule (Na2-O4e, 2.365(5) Å. The Na…Na distance 3.320 Å (Table 4.2) is on the shorter size compared to the range of 3.10–3.62 Å observed for others.[44-48] Na-O distances vary between 2.3 to 2.6 Å (Table 3.2) are usual for such bonds[44-48] but shorter than the range of 2.55-2.64 Å observed in sterically constrained trinuclear complexes[30,32] with the L-leucine analogue of the present ligand. The shorter Na-O lengths suggest less steric strain on the sodium ions.

The bridged structure and Na1's coordination to the iron(III) *bis* complex (Scheme I) resulted in a zig-zag chain along the *a*-axis (Fig 3.2B). As is common for the complexes with this type of ligand[30-32,39,40], numerous H-bonds formed due to the participation of non-coordinated Methanol, carboxylate, and threonine oxygen. However, most of these H-bonds remain within the chains. The interactions between the individual chains are mostly very weak C-H..p type interactions.[49]

Complex **3** crystallized in the $P2_1$ space group. The asymmetric unit contains $[K_2\{Fe(L^{L\text{-}thr})_2\}_2(H_2O)_2]$. MeOH. The K1 is bound to two phenolates (O1c, O1d) of a Fe(III) bis complex, while the K2 is bound to two iron(III) bis complex through phenolate (O1A, O1b) as well as carboxylate (O3d) atoms (Fig 3.1C). The iron(III) bis complex is structurally identical to that in complexes **1** and **2** with little difference (Table 3.2). The potassium ions are connected through bridges, similar to sodium ions in Complex **2** (Fig. 4.1C). The K-phenolate/carboxylate distances are longer than corresponding Na distances in **2** by about 0.3 – 0.5 Å expected due to the larger ionic radius of K (Table 4.2). The ionic radius difference between hexacoordinated Na and K is 0.36 Å.[42] These distances are within reasonable limits of what others have observed.[30-33,51,52] The K…K distance at 3.939 Å is longer than that of Na…Na in **2** (3.320 Å). The distance is shorter than the distances (4.39-4.77 Å) found for other solvent or chloro-bridged binuclear K complexes.[53-60] The shorter lengths suggest less steric strain on the potassium ions. The other significant difference with **1** is that the binding of K2 to multiple Fe(III) bis complex gave rise to a corrugated sheet-like 2D network (Fig. 4.2C).

Complex **4** crystallized in the *C*2 space group. The asymmetric unit contains half of the $[Ba_2\{Fe(L^{L\text{-}thr})_2\}_3(H_2O)_{10}]Cl.MeOH.3H_2O$ unit, which is symmetrical with the other half. Barium ions form a bridged structure similar to that in **2** and **3** (Fig. 4.1D), but the change in charge balance due to dipositive barium instead of Na^+/K^+ caused several changes. To

compensate extra charge, Ba:iron(III) complex is now 2:3, and a chloride counter ion completes the charge neutrality. The two non-identical Fe(III) *bis* complex units labelled Fe1 and Fe2 are nearly identical to similar units in **1**-**3** (Table 3.2). The Ba^{2+} coordinates to carboxylate oxygens (O2c & O3c) of the Fe2 unit in a syn-syn asymmetric fashion. The iron unit Fe1 participated in the bridge through carboxylate oxygen (O3a). Unlike in structures **2** and **3**, Ba^{2+} did not bind to any phenolate oxygens. Each of the Ba^{2+} is coordinated to eight oxygen atoms with bond lengths ranging from 2.7 to 3.0 Å. The Ba…Ba distance at 4.283 Å is on the higher side of the range 3.76 – 5.50 Å found in a few other structurally characterized complexes.[53-60] The higher coordination number of Ba^{2+} is common. The coordination network is extended in three dimensions, with a one-dimensional channel formed along the *c*-axis. The chloride ion and solvent molecules sit in the middle of the channel (Fig 4.2D).

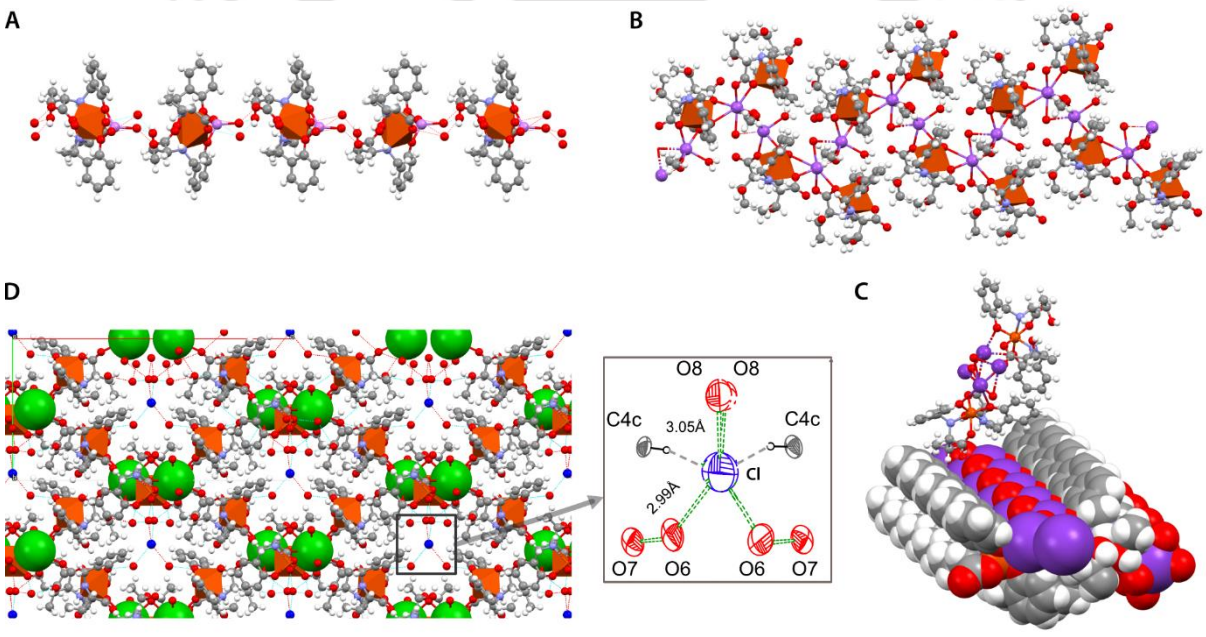

Figure 4.2. (A) linear chain of **1**, (B) Zig-Zag pattern of **2**, (C) Space-filled model showing the separation of hydrophilic from the hydrophobic part in 3, (D) and 3-D pattern of **4** trapping of Chloride ion inside the channel

Overall, structures of **1**-**4** show several trends. Except for the smallest Li^{+} (ionic radius, 0.59 Å), the other three ions form similar bridged structures (Fig. 3.1). Number of bridges and coordination number varies depending on the cation with the highest coordination number and bridge forms with the largest ion (Ba^{2+} ionic radius 1.56 Å).[19] The M-O lengths increase with corresponding ionic radius (Na^{+}, 1.02 and K^{+}, 1.38 Å)[19] Except in **4**, both carboxylate and phenolate oxygens coordinate with the cations. The smallest Li^{+} binds with phenolate **1,** and

the largest Ba^{2+} binds with carboxylate in **4**. Examples of phenolate binding to Ba^{2+} are known[61,62,] so the present observation could be due to the fitting of ions within the crystal lattice. The iron(III) bis complex remains nearly identical in all four complexes. The change in cation brought forth changes in the network, which varied from a one-dimensional chain to a three-dimensional network with channel formation. This opens up further possibilities for forming a coordination network by the use of different cation and bis complexes of amino acids other than threonine.

3.6. Charge transfer transitions in the solution and ESI-Mass

Despite having the coordination network, all four complexes are soluble in water as well as in Methanol. All show phenolate to iron(III) charge transfer transitions (LMCT) between 470 to 480 nm, and other ligand-based charge transfer transitions centred around 270 and 315 nm (Table 4). This is similar to the other two reported iron(III) complexes using L-histidine ligand analogous to the present ligand.[39,42] No further reports of iron(III) complex with reduced Schiff-base ligand of amino acid and salicylaldehyde are known.[23] Having a relatively strong visible band can be helpful. If the metal cations are bound to the phenolate or any other place of the iron(III) complex, the LMCT transition may shift depending on the cation's polarizing power.[24]

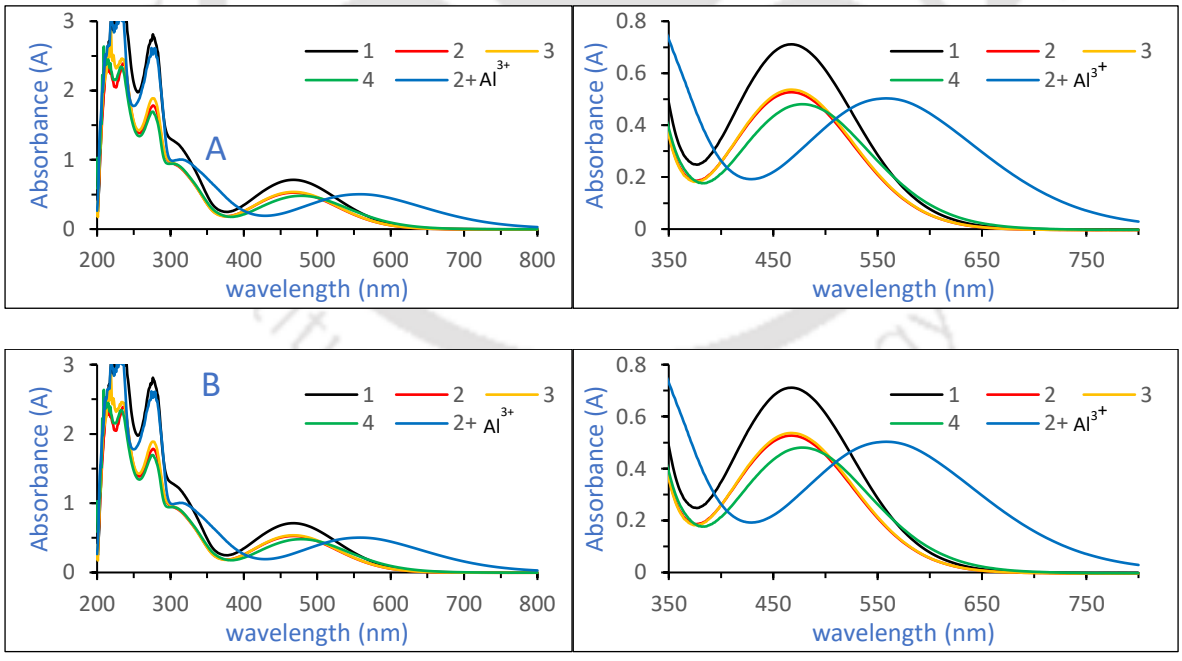

Figure 4.3. UV-visible spectra of the complexes (A) in MeOH and (B) Water

Irrespective of the solvents used, the LMCT band of **1-3** does not show any shift, but in **4,** it shifts by 7-10 nm (Table 4.3). The shift is small but reproducible (Fig 4.3). A shift of 15nm in Co(III) *d-d* transitions by changing mono to di-cation was observed by Reath et al. in a crown-ether derived system.[66] On the other hand, they did not report a significant shift in LMCT of Fe(III) complex substituting K^+ with Ba^{2+}.[67] In the reported complexes, both transition metal and alkaline or alkaline earth metal ions are bound within the same complex. In the reported examples, the effect of the second metal should occur because the crown ether part of their ligand is likely to hold the alkali or alkaline earth ions more securely. The effect did occur in their electrochemical results but not so much in the electronic spectrum.[66-70] Thus, the alkali metal ions' polarizing power may be insufficient for an observable shift, except Ba^{2+} and **1-3** are fully dissociated in the solution.

Table 4.3 Electronic spectral data.[a]

Complex		λ/nm (e/cm^{-1}M^{-1})
1	MeOH	276(7414), 323(3137), 474(1862)
	Water	277(7282), 315(2944), 472(1846)
2	MeOH	279(10231), 317(4913), 471(3121)
	Water	279(9682), 316(4358), 472(2543)
3	MeOH	277(10684), 316(4933), 471(3116)
	Water	279(9948), 317(4588), 472(2530)
4	Methanol	275(13041), 311(7176), 482(3739)
	Water	277(12094), 310(6322), 479(3258)
2+ Al^{3+}[b]	Methanol	316(7572), 561(3618)
	Water	316(7572), 561(3612)
2+ H^+[c]	Methanol	319 (6011), 564 (3190)

[b] 3.5 mol equivalent $Al(NO_3)_3.9H_2O$ added. [c] 0.8 equivalent $HClO_4$ in Methanol added. ε values in Al^{3+} and H^+ experiments were calculated using the concentration[a] (0.048 mol) value of **2**.

3.7. The shift in charge transfer band with Al^{3+} salt

As Ba^{2+} showed a small shift, we tested with Al^{3+} by adding aluminium salt to **2**. Besides the higher charge, aluminium ion detection in water by visual change has been of interest.[71-75] and one report detected Al^{3+} by the change in emission of an iridium(III) host metal complex due to the binding of aluminium.[76] In all, binding of Al^{3+} has been proposed based on indirect evidence, as x-ray structures with bound Al^{3+} are hard to come by. We added a 3.5-mole

equivalent of aluminium nitrate salt per iron(III) equivalent. The colour of the solution shifts dramatically from red-brown to purple (Fig 4.4).

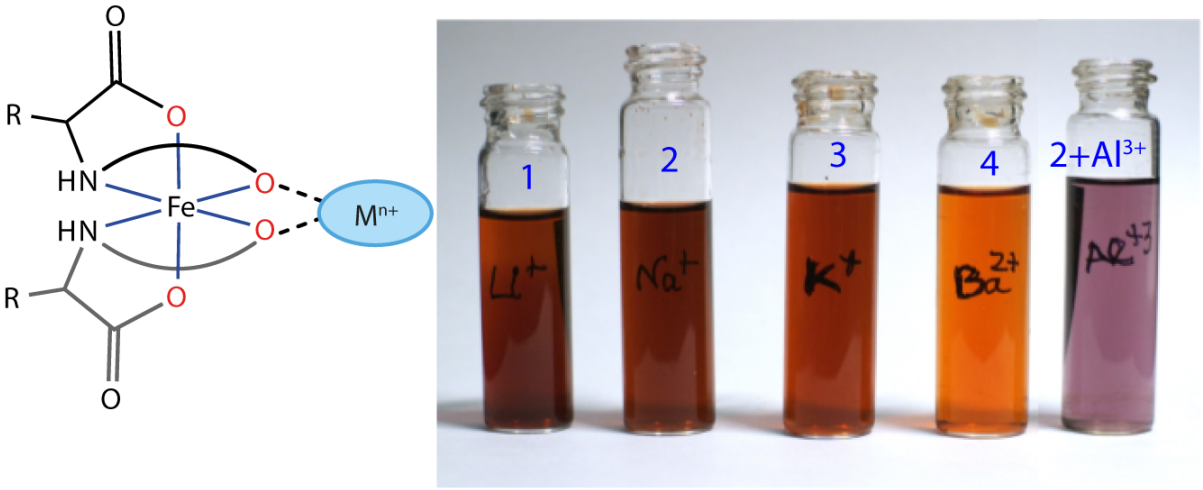

Figure 4.4. Visual colour changes of the complex in MeOH

The shift is almost 80nm (Table 4.3). Successively, on a preparative scale, we could isolate the solid but were unable to get a pure sample or a single crystal. The ESI-Mass spectrogram of the solid in Methanol was not very helpful. It showed both mass of $\{Fe(L^{L\text{-}thr})_2\}^-$ and $\{Al(L^{L\text{-}thr})_2\}^-$(Fig 4.7). One of the major peaks at 889.208 and its isotopic pattern closely matched $\{Al_2Fe(L^{L\text{-}thr})_3(OH)(MeO)_3\}^-$ (Calculated mass 889.213) based on mass and isotopic pattern. Given the labile nature of the complex, the observation of $\{Al(L^{L\text{-}thr})_2\}^-$ could be due to its formation in the charged chamber of the Mass spectrometer. The ESI-Mass (-ve) spectra of **1** and **4** (Fig 4.6) also show the isotopic pattern of $\{Fe(L^{L\text{-}thr})_2\}^-$.Thus, without a structure or other supporting evidence, the binding of aluminium cannot be confirmed. Another possibility is that the aluminium salts in water or polar solvents can hydrolyze and generate acid. The effect of acid could be checked easily. We repeated the titration experiment with a dilute perchloric acid solution (Fig 4.5A). Acid titration clearly showed the same colour change occurred with acid (Fig 4.5B). The colour change was clearly due to partial protonation of the complex. Further addition of acid leads to decolorizing of the solution as ligand gets protonated and dissociated. It also highlights the problem of testing metal ion detection experiments with hydrolyzable salts of weak bases and assuming the binding of aluminium without additional evidence. We have not come across any report where tests were done with acid or highlighted the problem of hydrolysis.

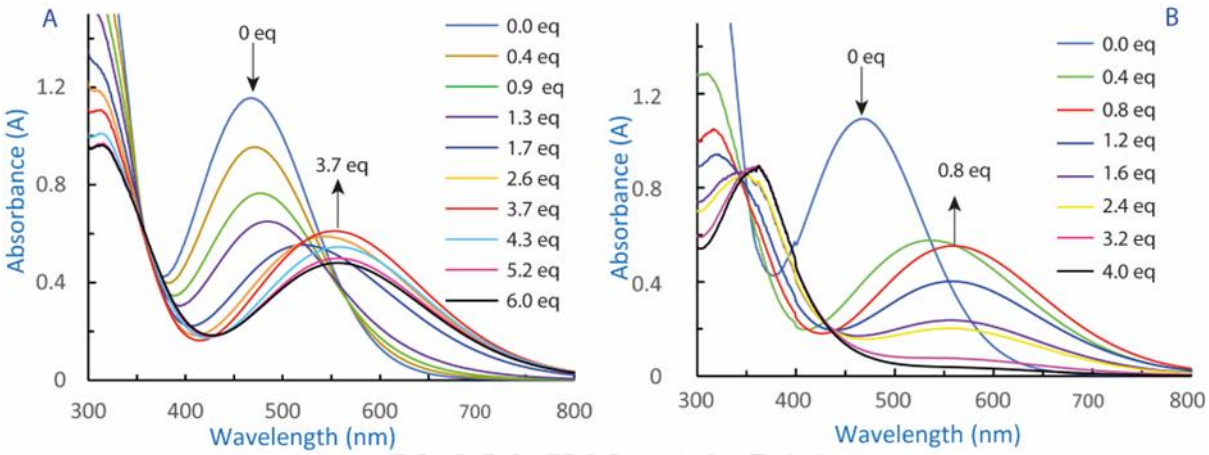

Figure 4.5. UV-visible titration of **2** with $Al(NO_3)_3$ (A) and $HClO_4$ (B)

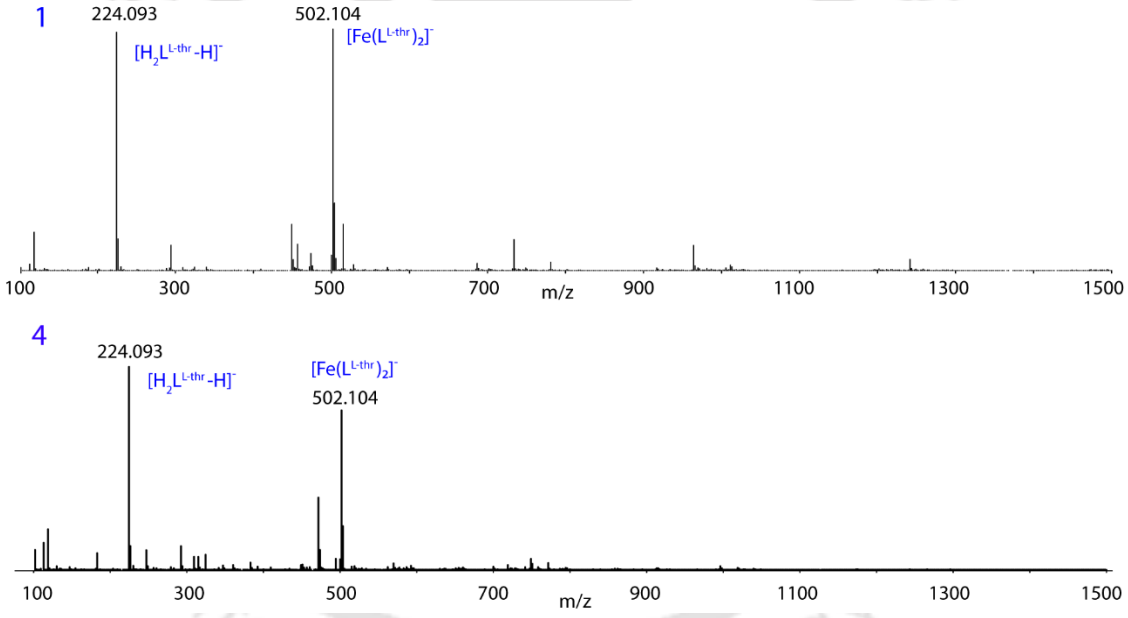

Figure 4.6. ESI-Mass (-Ve) of **1** and **4** in MeOH

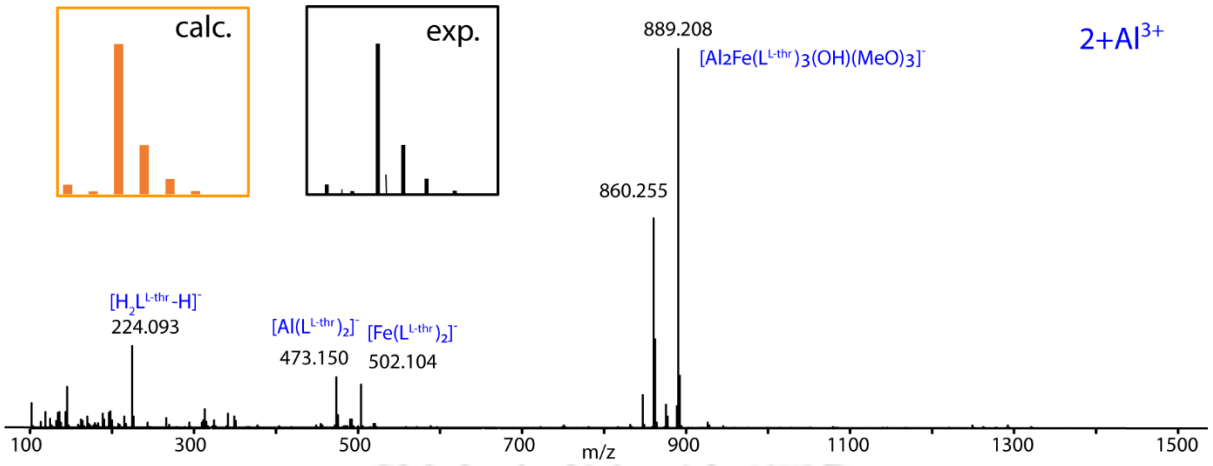

Figure 4.7. ESI-Mass (-Ve) of **2**+Al^{3+} in MeOH

3.8. Conclusions

Earlier, our interest was forming larger chiral assemblies from rigid metal complexes of relatively flexible amino acid-derived ligands.[30-33,39,40] Other forms of assemblies, such as coordination networks, were mostly ignored because of their poor solubility in most common solvents, which limits experiments with guest molecules.[31] However, we did find that Cu(II) and Ni(II) complexes can act as ligands to alkali metal ions. Still, the structural motif of the complex was not suitable for network formation.[30,32] Here, we build a new coordinatively saturated Iron(III) complex with an extra negative charge. It has multiple phenolates and carboxylates on different faces of the octahedron to promote multidirectional network formation. The threonine was chosen to increase the solubility. The $[Fe(L^{L\text{-}thr})_2]^-$ unit in all four complexes remains almost the same (Table 4.2). The alkali and alkaline earth metal ions bind to phenolate, carboxylate, or through both (Scheme I). Network formation is entirely due to the secondary metal cations (Figure 4.2). The smallest Li^+ in **1** simply connects two $[Fe(L^{L\text{-}thr})_2]^-$ forming a one-dimensional infinite chain along *a*- axis (Figure 4.2A). As the cation size increased, the **2-4** preferred to form solvent-bridged dimeric units, which connect the $[Fe(L^{L\text{-}thr})_2]^-$ units (Scheme 4.1 and Figure 4.3). The Ba^{2+}, being the largest, showed an increased coordination number (Scheme I). Interestingly, the use of chloride salt led to the trapping of chloride within a three-dimensional pocket in **4**. Chloride is surrounded by water oxygen atoms, which are H-bonded to the network. Solubility in water and the presence of phenolate to iron(III) charge transfer band allowed us to investigate if the secondary metal ions remain bound to the phenolate in solution and, if they do, whether they affect the charge transfer band.

The ESI-mass spectra (Fig 4.6) were not very helpful due to the labile nature of the complexes. All showed $[Fe(L^{L\text{-}thr})_2]^-$ units, but many of the higher mass peaks could not be put into a formula with confidence. They could very well be produced during the ionization process. The charge transfer band shows only about 10 nm from **3** to **4** but a negligible shift between the first three complexes. Reath et al., in a Fe(III) complex with attached crown ether bound to secondary metal ions, did not report a significant shift in LMCT of the Fe(III) complex substituting K^+ with Ba^{2+}.[67] Some parts of the networks in **1-4** may be retained in the solution, with the rest dissociated in the solution. However, as the recrystallization brought back the original structure, the usefulness of these networks is still valid. Testing with metal ions with a charge higher than Ba^{2+} led to an unexpected finding. The addition of Al^{3+} salt showed a significant visual colour change with a shift of 80nm. Detection of Aluminium ions in water by visual change has been of interest.[71-77] The shift observed is very high and thus needs to be investigated if it is due to the Al^{3+} binding. While ESI-Mass results were inconclusive, titration with acid confirmed that the protons released from the hydrolysis of aluminium salt are the reason behind the observation. There are a number of possible protonation sites within the Fe(III) complex as well as the bridges. The isolation and characterization of the protonated species proved difficult. Hence, the location of protonation could not be ascertained. The significance of this result is that the experiments on the detection of aluminium or any hydrolyzable metal salt in water or polar solvent need to consider the host's possible protonation and the possibility of binding with aluminium.

4.9. References

1 B. Liang, B. Li, Z. Li and B. Chen, *Chem. Eur. J.*, 2021, **27**, 12940–12952

2 D. M. Steinert, S. Ernst, S. K. Henninger and C. Janiak, *Eur. J. Inorg. Chem.*, 2020, 4502–4515

3 S. Cho, Y. Kim, S. Lee, H. Cho, J. Park, D. Hwan Hong, K. Kwon, H. Yoo, W. Choe and H. Ri Moon, *Eur. J. Inorg. Chem.*, 2022, e202101045

4 S. J. Lee and W. Lin, *Acc. Chem. Res.*, 2008, **41**, 521–537

5 V. Aggarwal, S. Solanki and B. D. Malhotra, *Chem. Sci.*, 2022, **13**, 8727–8743

6 P. Vairaprakash, H. Ueki, K. Tashiro and O. M. Yaghi, *J. Am. Chem. Soc.*, 2011, **133**, 759–76

7 M. Liu, L. Zhang and T. Wang, *Chem. Rev.*, 2015, **115**, 7304–7397

8 R. Freund, O. Zaremba, G. Arnauts, R. Ameloot, G. skorupskii, M.Dinca, A. Bavykina, J. Gascon, A. Ejsmont, J. Goscianska, M. Kalmutzki, U. Lachelt, E. Ploetz, C. S. Ddiercks and S. Wuttke, *Angew. Chem. Int. Ed.*, 2021, **60**, 23975-24001

9 Q. Zeng, X. Liu, Y. Zheng, K. W. K. Yeung, Z. Cui, Y. Liang, Z. Li, S. Zhu, X. Wang and S. Wu, *Chem. Soc. Rev.*, 2021, **50**, 5086-5125

10 L. E. Kreno, K. Leong, O. K. Farha, M. Allendorf, R. P. V. Duyne and J. T. Hupp, *Chem. Rev.* 2012, **112**, 1105–1125

11 B. Le Ouay, R. Minami, P. K. Boruah, R. Kunitomo, Y. Ohtsubo, K. Torikai, R. Ohtani, C. Sicard and M. Ohba, *J. Am. Chem. Soc.*, 2023, **145**, 11997–12006

12 P. Anithabanu and V. G. Vaidyanathan, *Int. J. Biol. Macromol.*, 2021, **190**, 56–60

13 B. Phukan, S. Ghorai, K. Deka, P. Deb and C. Mukherjee, *Crystal Growth & Design* **2018, *18***, 531-539

14 M. Sánchez-Sánchez, N. Getachew, K. Díaz, M. Díaz-García, Y. Chebude and I. Díaz, *Green Chem.*, 2015, **17**, 1500–1509

15 J. Dong, Y. Liu and Y. Cui, *Acc. Chem. Res.* 2021, **54**, 194–206

16 T. N. Nguyen, S. V. Eliseeva, I. Martinic, P. L. Carver, T. Lathion, S. Petoud and V. L. Pecoraro, *Chem. Eur. J.*, 2023, e202300226

17 G. González-Riopedre, M. R. Bermejo, M. I. Fernández-García, A. M. González-Noya, R. Pedrido, M. J. Rodríguez-Doutón and M. Maneiro, *Inorg. Chem.*, 2015, **54**, 2512–2521

18 W. Chen, X. Tang, W. Dou, Z. Ju, B. Xu, W. Xu and W. Liu, *Chem. Commun.*, 2016, **52**, 5124–5127.

19 B. Wang, B. Ma, Z. Wei, H. Yang, M. Wang, W. Yin, H. Gao and W. Liu, *Inorg. Chem.*, 2021, **60**, 2764–2770

20 X. Wang and J. J. Vittal, *Inorg. Chem.*, 2003, **42**, 5135–5142

21 R. R. Golwankar, A. Kumar, V. W. Day and J. D. Blakemore, *Chem. Eur. J.*, 2022, **28**, e202200344

22 M. Andruh, *Dalton Trans.*, 2015, **44**, 16633–16653

23 Q. Yao, Y. Wang, B. Zhao, X. Zhu, Y. Luo, D. Yuan and Y. Yao, *Inorg. Chem.*, 2022, **61**, 10373–10382.

24 G. Kumar and R. Gupta, *Inorg. Chem.*, 2013, **52**, 10773–10787

25 W. Gruszka and J. A. Garden, *Nat. Commun.*, 2021, **12**, 3252

26 C. J. Pedersen, *Angew. Chem. Int. Ed.*, 1988, **27**, 1021-1027

27 J. L. Lehn, *Angew. Chem. Int. Ed.*, 1988, 27, **89**-112

28 G. Mezei, C.M. Zaleski andV. L. Pecoraro, *Chem. Rev.*, 2007, **107**, 4933–5003

29 E. R. Trivedi, S. V. Eliseeva, J. Jankolovits, M. M. Olmstead, S. Petoud and V. L. Pecoraro, *J. Am. Chem. Soc.*, 2014, **136**, 1526–1534

30 M. Dubey, R. R. Koner and M. Ray, *Inorg. Chem.*, 2009, **48**, 9294–9302.

31 S. C. Sahoo and M. Ray, *Chem. Eur. J.*, 2010, **16**, 5004–5007

32 M. Dubey and M. Ray, *CrystEngComm*, 2013, **15**, 9648

33 K. Murayama and K. Aoki, *Inorganica Chim. Acta*, 1998, **281**, 36–42

34 D. F. Evans 1974 *J. Phys. E: Sci. Instrum*. 7 247

35 C. J. OConnor, Prog. Inorg. Chem., 1982, **29**, 203

36 CrysAlis CCD and CrysAlis RED. Oxford Diffraction Ltd, Yarnton, Oxfordshire, England. Oxford Diffraction, 2009

37 G. M. Sheldrick, Acta Crystallogr., Sect. A: Fundam. Crystallogr., 2008, A64, 112

8 M. N. Burnett and C. K. Johnson, ORTEP-III: Oak Ridge Thermal Ellipsoid Plot Program for Crystal Structure Illustrations, Oak Ridge National Laboratory Report ORNL-6895, 1996

39 Md. A. Alam, M. Nethaji and M. Ray, *Inorg. Chem.*, 2005, **44**, 1302–1308

40 Md. A. Alam, M. Nethaji and M. Ray, *Angew. Chem. Int. Ed*., 2003, **42**, 1940–1942

41 B. N. Figgis and J. Lewis, *Progress in Inorganic Chemistry, F.A. Cotton*., 1964, **6**, 37-239

42 X.-F. Ma, J.-L. Tian, W. Gu, S. Gao, S.-P. Yan and D.-Z. Liao, *Inorg. Chem. Commun*., 2008, **11**, 256–259

43 L. Baklouti and J. Harrowfield, *Dalton Trans*., 2023, **52**, 7772–7786.

44 E. Nizioł, D. Jędrzkiewicz, A. Wiencierz, W. Paś, D. Trybuła, W. Zierkiewicz, A. Marszałek-Harych and J. Ejfler, *Inorg. Chem. Front*., 2023, **10**, 1076–1090

45 T. Kurogi, Y. Ishida, T. Hatanaka and H. Kawaguchi, *Chem. Commun*., 2012, **48**, 6809.

46 T. A. Bazhenova, N. V. Kovaleva, G. V. Shilov, G. N. Petrova and D. A. Kuznetsov, *Eur. J. Inorg. Chem.*, 2016, **2016**, 5215–5221.

47 X. Chen, S.-B. Qiao, D. Liu, J.-P. Lang, Y. Zhang, C. Xu and S.-L. Ma, *CrystEngComm*, 2010, **12**, 1610

48 A. Kumar, S. D. Kurbah, I. Syiemlieh, S. A. Dhanpat, R. Borthakur and R. A. Lal, *Inorganica Chim. Acta*, 2021, **515**, 120068

49 The weak hydrogen bond in structural chemistry and biology. G. R. Desiraju and T. Steiner , IUCr Monographs on Crystallography ,

50 R. D. Shannon, *Acta Crystallogr. Sect. A*, 1976, **32**, 751–767

51 P. Purdy and R. J. Butcher, *Acta Crystallogr. Sect. E Crystallogr. Commun*., 2019, **75**, 714–716

52 D. E. Lynch, C. R. Reeves, D. R. Errabelli and D. G. Hamilton, *J. Mol. Struct*., 2021, **1229**, 129768

52 T. J. Boyle, L. A. M. Steele and A. Saad, *Inorganica Chim. Acta*, 2013, **394**, 259–268

54 J. Zhang, L. G. Hubert-Pfalzgraf and D. Luneau, *Inorg. Chem. Commun.*, 2004, **7**, 979–984

55 D. K. Sinitsa, T. S. Sukhikh, P. A. Petrov, V. A. Nadolinny, S. N. Konchenko and N. A. Pushkarevsky, *Eur. J. Inorg. Chem.*, 2019, **2019**, 4373–4383

56 C. Park, H. Choi, G. Y. Lee, B. K. Park and T.-M. Chung, *ACS Omega*, 2023, **8**, 22783–22787

57 Y. Sarazin, B. Liu, T. Roisnel, L. Maron and J.-F. Carpentier, *J. Am. Chem. Soc.*, 2011, **133**, 9069–9087

58 B. Liu, T. Roisnel and Y. Sarazin, *Inorganica Chim. Acta*, 2012, **380**, 2–13

59 B. Masci and P. Thuéry, *CrystEngComm*, 2007, **9**, 582–590

60 6R. Gardiner, D. W. Brown, P. S. Kirlin and A. L. Rheingold, *Chem. Mater.*, 1991, **3**, 1053–1059

61 J. Zhang, L. G. Hubert-Pfalzgraf and D. Luneau, *Inorg. Chem. Commun.*, 2004, **7**, 979–984

62 M. L. Foo, S. Horike and S. Kitagawa, *Inorg. Chem.*, 2011, **50**, 11853–11855

63 R. Ganguly, B. Sreenivasulu and J. J. Vittal, *Coord. Chem. Rev.*, 2008, **252**, 1027–1050

64 A. Kumar, D. Lionetti, V. W. Day and J. D. Blakemore, *Chem. Eur. J.*, 2018, **24**, 141–149

65 P. Bhunia, R. M. Gomila, A. Frontera and A. Ghosh, *Dalton Trans.*, 2023, **52**, 3097–3110

66 A. H. Reath, J. W. Ziller, C. Tsay, A. J. Ryan and J. Y. Yang, *Inorg. Chem.*, 2017, **56**, 3713–3718

67 T. Chantarojsiri, J. W. Ziller and J. Y. Yang, *Chem. Sci.*, 2018, **9**, 2567–2574

68 A. Kumar, D. Lionetti, V. W. Day and J. D. Blakemore, *Chem. Eur. J.*, 2018, **24**, 141–149

69 P. Bhunia, R. M. Gomila, A. Frontera and A. Ghosh, *Dalton Trans.*, 2023, **52**, 3097–3110

70 R. R. Golwankar, A. Kumar, V. W. Day and J. D. Blakemore, *Chem. Eur. J.*, 2022, **28**, e202200344

71 M. C. Tu, D. Rajwar, G. Ammanath, P. Alagappan, U. H. Yildiz and B. Liedberg, *Anal. Chim. Acta*, 2016, **912**, 105–110

72 A. R. Unniram Parambil, K. P., A. Silswal and A. L. Koner, *RSC Adv.*, 2022, **12**, 13950–13970

73 V. Kumar, P. Kumar, S. Kumar, D. Singhal and R. Gupta, *Inorg. Chem.*, 2019, **58**, 10364–10376

74 I. Song, P. Torawane, J.-S. Lee, S. D. Warkad, A. Borase, S. K. Sahoo, S. B. Nimse and A. Kuwar, *Mater. Adv.*, 2021, **2**, 6306–6314

75 M.-H. Yu, T.-L. Hu and X.-H. Bu, *Inorg. Chem. Front.*, 2017, **4**, 256–260

76 Y. Suzuki, I. Mizuno, Y. Tabei, Y. Fujioka, K. Shinozaki, T. Sugaya and K. Ishihara, *Inorg. Chem.*, 2019, **58**, 9663–9671

77 T. Chantarojsiri, J. W. Ziller and J. Y. Yang, *Chem. Sci.*, 2018**, 9**, 2567–2574

भारतीय प्रौद्योगिकी संस्थान गुवाहाटी
Indian Institute of Technology Guwahati

Chapter V

Stepwise synthesis of the rigid linear hetero-bimetallic [Co^{3+}, M^{2+}, Co^{3+}] chiral complex with a labile M^{2+} site at the centre

5.1. Introduction

In the previous chapter, we synthesized the Fe(III) complex polymeric chain using L-threonine-derived reduced Schiff base ligand and using alkali and alkaline earth metal ions of different charges and sizes. However, the assemblies obtained are paramagnetic; therefore, without the solid-state structure, characterization becomes challenging and solution-state studies are limited. In this chapter, we intend to synthesise Co(III) bis complex, the analogue of Fe(III), using the same L-threonine-derived reduced Schiff base ligand and replace alkali and alkaline metal ions with transition metal ions. By doing so, we can obtain a more rigid complex that will be better characterized using the spectroscopic technique.

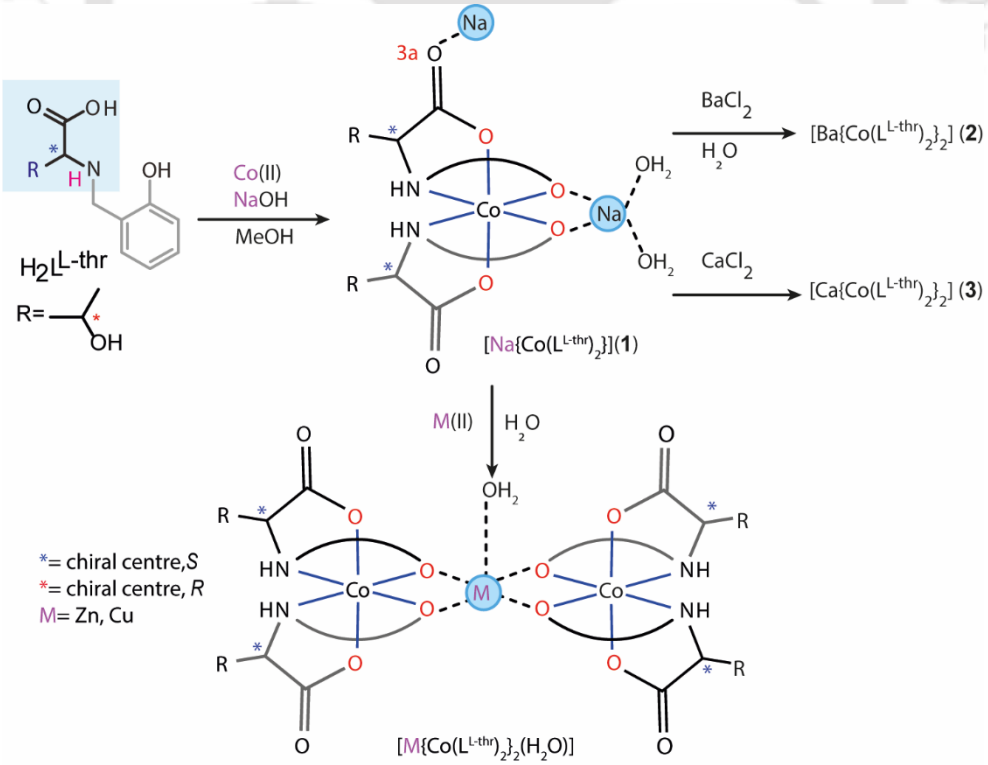

Scheme 5.1. Synthesis of ligand and stepwise synthesis of the linear heterobimetallic complexes.

Our choice of metal ion is such that the Co(III) complexes are likely to be diamagnetic such that we can use ^{1}H NMR spectroscopy to understand the interactions in the solution,[1,2] and we also plan to replace the central metal K^+ ion with metal ions of different charge and size and compare it with the previously synthesized complexes.[3–7] We tried to develop coordination complexes as the building blocks for constructing ordered structures in which two different metal ions could be placed in close proximity.[8,9] A coordination complex as the building block offers many benefits, such as spectroscopic and magnetic properties and structural rigidity. Such induced rigidity can place the auxiliary functional groups in a preorganized conformation with an option to control the geometrical placement of such groups.[10] These auxiliary functional groups could then be utilized to coordinate a secondary metal ion.[11] This synthetic strategy leads to the generation of heterodimetallic complexes and networks of a highly ordered nature.[12–15] The selection of the central metal ion was based on the possible application of the exposed Lewis-acidic metal ion in organic transformations.[16–19]

5.2. Experimental section

5.2.1. Materials and Methods

O-Salicylaldehyde and L-threonine were purchased from Aldrich and Co. Metal salts $BaCl_2 \cdot 2H_2O$, $Al(NO_3)_3 \cdot 9H_2O$, $Zn(NO_3)_3 \cdot 6H_2O$ and $Cu(NO_3)_3 \cdot 6H_2O$. were purchased from Sigma-Aldrich. The solvents used were purified before use, following the standard literature procedure. Elemental analyses were done using a ThermoFisher Scientific Flash Smart V CHNS/O analyzer. Details of the instruments used have already been described in Chapter 2.

5.3. Synthesis and Characterization

5.3.1. $H_2L^{L\text{-}thr}$. The amino acid L-threonine (2.00 g, 16.8 mmol) and $LiOH \cdot H_2O$ (0.71 g, 16.8 mmol) were dissolved in 25 mL of methanol and stirred for 10 min, which gave a colourless solution. The methanolic solution of salicylaldehyde (2.05 g, 16.8 mmol) was added dropwise to the above solution. The solution turned yellow immediately. The solution was stirred for 2 h, and solid $NaBH_4$ (0.8 g, 21.1 mmol) was added portion-wise. The solution turned colourless within a few minutes. It was stirred for another 1 h, and the solvent was removed using a rotary evaporator. The solid obtained was dissolved in ~5 mL of water and acidified to pH 6-7 using dil HCl, and we removed the water using a rotary evaporator. The sticky solid was dissolved in MeOH and kept for crystallization. Block-shaped crystals were obtained after three days.

The white crystals obtained were washed using acetone, collected, and dried under a vacuum desiccator. Yield 2.64 g (69.8%). ^{1}H NMR [$H_2L^{L\text{-}thr}$] (DMSO-d_6, 500 MHz ppm) 1.18 (d, 3H, H^{10}, *J*=10 Hz), 3.06 (m, 1H, H^{8}, *J*=5 Hz), 3.90 (m, 1H, H^{9}, *J*=10 Hz), 4.05 (d, 1H, H^{7a}, *J* =15 Hz), 4.05 (d, 1H, H^{7}, *J* =15 Hz), 6.78 (t, H, H^{4} *J*= 7.5 Hz), 6.80 (t, H, H^{2} *J*= 7.5 Hz), 6.91 (d, 1H, H^{3}, *J* =8 Hz), 7.25 (d, 1H, H^{5}, *J* =7.5 Hz). FTIR (KBr, cm^{-1}) ν $(COOH)_{asym}$ 1615 (s), 1492 (s), ν $(COOH)_{sym}$ 1407 (m). m/z (ESI-MS $[H_2L^{L\text{-}thr}+H]^{+}$); calcd: 226.10 found 226.10.

5.3.2. [Na{Co($L^{L\text{-}thr}$)$_2$}(H_2O)$_2$] (1). $H_2L^{L\text{-}thr}$ (0.2 g, 0.88 mmol) and NaOH (0.070 g, 1.76 mmol) were mixed in 15 mL of MeOH, which gave a clear solution. We added a methanolic solution of $Co(ClO_4)_2$• $6H_2O$ (0.16 g, 0.44 mmol). The solution turns pink immediately, and after stirring for 2 h, the solution turns green. We stirred for another 2 h and removed the solvent. The green solid was washed with MeCN, dissolved in 8 mL of Milli-Q water, layered with CH_3CN and kept in the freezer. The needle-shaped green crystals were obtained after 3 days. Yield: 0.18 g (74.5 %). FTIR (cm^{-1}): ν $(COOH)_{asym}$ 1627 (s), $(COOH)_{sym}$ 1482 (s). ^{1}H NMR of [Na{Co($L^{L\text{-}thr}$)$_2$}(H_2O)$_2$] (DMSO-d_6, 500 MHz. ppm) 7.04 (d, 2H, H^{5}, *J* =8.5 Hz), 6.95 (m, 2H, H^{2}, *J*=8 Hz), 6.94 (m, 2H, H^{4}, *J*=8.5 Hz), 6.81 (s, 2H, H^{NH}), 6.36 (t, 2H, H^{3}, *J* =7 Hz), 6.27 (s, 2H, H^{OH}), 4.12 (m, 2H, H^{9}, *J*=7 Hz), 4.05 (d, 2H, H^{7}, *J*=12.5 Hz), 2.93 (m, 2H, H^{8}, *J* =4.5 Hz), 2.86 (d, 2H, H^{7a}, *J* =12.5 Hz), 1.42 (d, 6H, H^{10}, *J*=7 Hz). (ESI-MS): m/z, [Co($L^{L\text{-}thr}$)$_2$]$^{-}$); calcd: 505.38 found 505.10, [{Co($L^{L\text{-}thr}$)$_2$}$_2$+H]$^{-}$; calcd: 1011.21 found 1011.21, [Na{Co($L^{L\text{-}thr}$)$_2$}$_2$]$^{-}$ calcd: 1033.19 found 1033.19. Anal. Calcd for [NaCo($L^{L\text{-}thr}$)$_2$(H_2O)]• $2H_2O$: C, 44.00, H, 5.70, N, 4.66. Found: C, 44.56, H, 6.01, N, 4.60.

Note. For elemental analysis, the crystalline samples were powdered and dried under a vacuum desiccator for several days before analysis. Thus, the number and type of solvent molecules in the crystal structure and isolated product differ. We used the formula weight of the bulk for solution concentration, percentage yield, and magnetic moment calculation.

5.3.3. [Ba{Co($L^{L\text{-}thr}$)$_2$}$_2$] (2). Complex **1** (0.2 g, 0.32 mmol) and $BaCl_2$• $2H_2O$ (0.039 g, 0.16 mmol) were mixed in 15 mL of MeOH, and the solution changed from green to deep green within a few minutes. We stirred for another 2 h, and the green solid precipitated out. We filtered the green solid using a G4 crucible and washed it with CH_3CN. Yield 0.201 g (52 %). FTIR (cm^{-1}): ν $(COOH)_{asym}$ 1634 (s), $(COOH)_{sym}$ 1483 (s). ^{1}H NMR of [Ba{Co($L^{L\text{-}thr}$)$_2$}(H_2O)$_4$] (DMSO-d_6, 500 MHz. ppm) 7.32 (d, 2H, H^{5}, *J* =8.5 Hz), 6.95 (m, 2H, H^{4}, *J*=7.5 Hz), 6.82 (m, 2H, H^{2}, *J*=7 Hz), 6.80 (s, 2H, H^{NH}), 6.42 (t, 2H, H^{3}, *J* =7 Hz), 6.28 (s, 2H, H^{OH}), 4.13 (m, 2H, H^{9}, *J*=6.5 Hz), 3.58 (d, 2H, H^{7}, *J*=13 Hz), 2.86 (m, 2H, H^{8}, *J* =5 Hz), 2.55 (d, 2H, H^{7a}, *J* =13

Hz), 1.38 (d, 6H, H^{10}, *J*=6.5 Hz). (ESI-MS): m/z, $[Co(L^{L\text{-}thr})_2]^-$); calcd: 505.38 found 505.10. Anal. Calcd for $[Ba\{Co(L^{L\text{-}thr})_2\}_2]\bullet 5H_2O$: C, 42.52, H, 4.58, N, 4.92. Found: C, 42.68, H, 5.04, N, 4.52.

5.3.4. $[Ca\{Co(L^{L\text{-}thr]})_2\}_2]$ (3). The Complex **1** (0.2 g, 0.37 mmol) and $CaCl_2$ (0.041 g, 0.37 mmol) were mixed in 15 mL of MeOH, and the solution changed from green to deep green within few minutes. We stirred for another 2 h and removed the solvent. The green solid was washed with MeCN, dissolved in 8 mL of Milli-Q water, layered with CH_3CN and kept in the freezer. The needle-shaped green crystals were obtained after 3 days. Yield 210 g (58%). ^1H NMR of $[Ca\{Co(L^{L\text{-}thr]})_2\}]$. $2H_2O$ (DMSO-d_6, 500 MHz. ppm) 7.30 (d, 2H, H^5, *J* =8Hz), 7.06 (m, 2H, H^2, *J*=8 Hz), 7.06 (m, 2H, H^4, *J*=8.5 Hz), 7.06 (s, 2H, H^{NH}), 6.57 (t, 2H, H^3, *J* =7 Hz), 6.27 (s, 2H, H^{OH}), 4.09 (m, 2H, H^9, *J*=7 Hz), 4.09 (d, 2H, H^7, *J*=12 Hz), 2.91 (m, 2H, H^8, *J* =5 Hz), 2.87 (d, 2H, H^{7a}, *J* =12 Hz), 1.45 (d, 6H, H10, *J*=7 Hz). (ESI-MS): m/z, $[Co(L^{L\text{-}thr})_2]^-$); calcd: 505.38 found 505.10. Anal. Calcd for $[Ca\{Co(L^{L\text{-}thr})_2\}_2]\bullet 2H_2O$: C, 48.62, H, 5.19, N, 5.15. Found: C, 48.57, H, 5.64, N, 5.21.

5.3.5. $[Zn\{Co(L^{L\text{-}thr})_2\}_2(H_2O)]$ (4). We dissolved the complex **1** (0.200 g, 0.37 mmol) in 10 mL of Milli-Q water. The solution turns green. We add the Methanolic solution of $Zn(NO)_3\bullet 6H_2O$ (0.51 g, 0.18 mmol) to the above solution. The solution turns deep green. We kept the solution in a conical flask for slow evaporation. After 3 days, the block-shaped, green crystal was obtained. The obtained crystals were collected, washed with ethyl acetate, and dried under a vacuum desiccator. Yield 0.19 g (54 %). FTIR (cm^{-1}): ν $(COOH)_{asym}$ 1621 (s), $(COOH)_{sym}$ 1486 (s). ^1H NMR of $[Zn\{Co(L^{L\text{-}thr})_2\}_2(H_2O)]$ (DMSO-d_6, 500 MHz. ppm) 7.40 (d, 4H, H^5, *J* =7 Hz), 7.17 (s, 4H, H^{NH}), 7.03 (m, 4H, H^2, *J*=8 Hz), 6.71 (t, 4H, H^3, *J*=7 Hz), 6.47 (m, 4H, H^4, *J* =7 Hz), 6.44 (s, 4H, H^{OH}), 4.30 (d, 4H, H^7, *J*=12.5 Hz), 4.17 (m, 4H, H^9, *J*=4.5 Hz), 3.00 (m, H, H^8, *J* =4.5 Hz), 2.96 (d, 4H, H^{7a}, *J* =12.5 Hz), 1.46 (d, 12H, H^{10}, *J*=7 Hz); m/z (ESI-MS, $[M - H]^-$, $[Zn\{Co(L^{L\text{-}thr})_2\}_2 - H]^-$ calcd:1073.13 found 1073.13. Anal. Calcd for $[Zn\{Co(L^{L\text{-}thr})_2\}_2(H_2O)] \bullet MeOH, H_2O$: C, 47.47, H, 5.42, N, 4.52. Found: C, 47.23, H, 5.28, N, 4.89.

5.3.6. $[Cu\{Co(L^{L\text{-}thr})_2\}_2(H_2O)]$ (5). We dissolved the complex **1** (0.200 g, 0.37 mmol) in 10 mL of Milli-Q water. The solution turns green. We add the Methanolic solution of $Cu(NO)_3\bullet 6H_2O$ (0.42 g, 0.18 mmol) to the above solution. The solution turns deep green. We kept the solution in a conical flask for slow evaporation. After 3 days, the block-shaped, green crystal was obtained. The obtained crystals were collected, washed with ethyl acetate, and dried under a vacuum desiccator. Yield 0.187 g, (52 %). FTIR (cm^{-1}): ν $(COOH)_{asym}$ 1622 (s), $(COOH)_{sym}$

1487 (s). m/z (ESI-MS, $[M-H]^-$, $[Cu\{Co(L^{L\text{-}thr})_2\}_2\text{-}H]^-$ calcd:1072.13 found 1072.13. μ_{eff} (powder, 298, K); 2.08 μB/Cu. Anal. Calcd for $[Cu\{Co(L^{L\text{-}thr})_2\}_2(H_2O)]\bullet$ MeOH, H_2O: C, 47.31, H, 5.47, N, 4.90. Found: C, 47.05, H, 5.18, N, 5.06

5.3.7. $[Co(HL^{L\text{-}thr})_2](NO_3)$ (6). Complex **1** (0.2 g, 0.37 mmol) and $Al(NO_3)_3\bullet$ $9H_2O$ (0.13 g, 0.37 mmol) were mixed in 15 mL of MeOH, and the solution changed from green to deep green within a few minutes. We stirred for another 2 h and removed the solvent. The green solid was washed with MeCN, dissolved in 8 mL of Milli-Q water, layered with CH_3CN and kept in the freezer. The green solid was obtained after 3 days. Yield 0.16 g (75 %). ^{1}H NMR of $[Co(HL^{L\text{-}thr})_2]^+$ (DMSO-d_6, 500 MHz. ppm) 7.10 (d, 2H, H^5, *J* =7 Hz), 6.99 (m, 2H, H^2, *J*=8 Hz), 6.99 (m, 2H, H^4, *J*=8.5 Hz), 6.7 (s, 2H, H^{NH}), 6.42 (t, 2H, H^3, *J* =7 Hz), 6.33 (s, 1H, H^{OH}), 4.18 (m, 2H, H^9, *J*=7 Hz), 4.12 (d, 2H, H^7, *J*=15 Hz), 2.99 (m, 2H, H^8, *J* =4.5 Hz), 2.91 (d, 2H, H^{7a}, *J* =15 Hz), 1.47 (d, 6H, H10, *J*=7 Hz). Anal. Calcd for $[Co(HL^{L\text{-}thr})_2]\bullet$ $4H_2O$: C, 41.32, H, 5.35, N, 6.57. Found: C, 41.45, H, 5.79, N, 6.97

5.4. X-ray Crystallography

Crystals of the complexes **1**, **4**, and **5** obtained during synthesis were used for X-ray analysis. The complexes **2** did not yield crystals. All geometric and intensity data for crystal **1** was collected at room temperature using a Bruker SMART APEX CCD diffractometer equipped with a fine focus 1.75 kW sealed tube Mo-Kα (λ= 0.71073 Å) X-ray source, with increasing ω (width of 0.3º per frame) at a scan speed of either 3 or 5 s/frame. The SMART software was used for data acquisition and the SAINT software for data extraction. Absorption corrections were done using a multi-scan. For the crystals (**4** and **5**), the intensity data were collected at room temperature using a single Source Super Nova CCD system from Agilent Technologies equipped with a fine focus 1.75 kW sealed tube with Mo-Kα radiation. The data were reduced using CrysAlis RED.[20] The structure solution and refinement were performed on the WinGX environment using the SHELXS97 SHELXL97 programs.[21] All non-hydrogen atoms were refined anisotropically. The hydrogen atoms were located from the Fourier maps and refined isotropically wherever possible. Thus, some C-H bonds will not be ideal and may vary. Most hydrogen atoms attached to the solvent molecules could not be located or fixed, so the molecular weight may not match. ORTEP obtained selected crystallographic data summarized in Table 5.1. A perspective view of the complex was obtained by ORTEP.[22]

Table 5.1. Selected crystallographic data for the complexes[a]

Compounds	**1**	**4**	**5**
Empirical formula	$C_{22}H_{26}CoN_2NaO_{10}$	$C_{45}H_{52}Co_2N_4O_{23}$ Zn	$C_{45}H_{54}Co_2Cu$ N_4O_{26}
M	560.37	1200.13	1248.32
Wavelength (Å)	0.71073	0.71073	0.71073
Crystal system	monoclinic	orthorhombic	orthorhombic
Space group	*C 2*	*P* 2_1 2_1 2_1	*P* 2_1 2_1 2_1
a, Å	20.568(2)	15.8445(8)	15.8775(4)
b, Å	7.6341(6)	17.5700(12)	17.5466(6)
c, Å	15.9451(16)	20.8146(9)	20.9975(5)
α, deg	90.00	90.00	90.00
β, deg	104.064(6)	90.00	90.00
γ, deg	90.00	90.00	90.00
V, Å^3	2428.6(4)	5794.5(6)	5849.8(3)
Z	4	4	4
ρ, g cm^{-3}	1.533	1.376	1.417
μ, mm^{-1}	0.784	1.053	1.003
Flack parameter	0.055(13)	0.02(3)	-0.020(11)
Reflections collected	26467	11523	11193
Independent reflections	16824	7184	8638
Goodness of fit	1.034	0.902	0.909
Final *R* indices [*I*	*R*1 = 0.0794	*R1* = 0.0731	*R1* = 0.0557
>2σ(*I*)]	*wR*2 = 0.1729	*wR*2 = 0.1792	*wR*2 = 0.1363
R indices (all data)	*R*1 = 0.1547	*R*1 = 0.1201	*R*1 = 0.0797
	*wR*2 = 0.2026	*wR*2 = 0.2190	*wR*2 = 0.1560

[a]Refinement method: full-matrix least-squares on F^2.

5.5. Results and Discussion

We synthesized the reduced Schiff base ligand $H_2L^{L\text{-thr}}$ using amino acid L-threonine and O-salicyaldehyde. We used LiOH to deprotonate the zwitterionic amino acid. *In situ,* the reduction of the Schiff base and subsequent pH adjustment resulted in the ligand. We characterized the ligand using ^{1}H NMR and ESI-Mass (experimental section 5.3.1). The reaction between divalent Co(II), NaOH, and ligand $H_2L^{L\text{-thr}}$ in MeOH at a 1:4:2 ratio yields complex **1**. Complex **1** was characterized using ^{1}H NMR, 2D- NMR, ESI-Mass, and solid-state structure. Complex **2** and **3** were synthesized by adding $BaCl_2$ and $CaCl_2$, respectively to the methanolic solution of complex **1**. We could not get the solid-state structure of complexes **2**, **3**, and **6** as the complexes failed to crystallize. We characterized using ^{1}H NMR and 2D- NMR. Complex **4** and **5** were synthesized by dissolving complex **1** in Milli-Q water and adding Zn(II) and Cu(II) salt, respectively and kept for slow evaporation (experimental section 4.3.4-5). The block-shaped green crystals of **4** and **5** were obtained after 3 days. We use ESI-Mass, ^{1}H NMR, 2D-COSY and HSQC to characterize Complex **4,** which is structurally characterized as well. However, we can only use ESI-Mass and solid-state structure to characterize complex **5**. All the complexes were characterized using elemental analysis, FTIR, and solid-state magnetism. The room temperature solid-state magnetic moment of complex **5** is 2.08 BM, which is within the expected range of monomeric Cu(II) complexes.[23]

5.5.1. $[Na\{Co(L^{L\text{-thr}})_2\}(H_2O)_2]$ (1). Complex **1** crystallized out in space group *C2*. The selected bond length and angles of the complex are given in Table 4.2. The Co(III) is coordinated to two tridentate $L^{L\text{-thr}}$ ligands, which are doubly deprotonated.

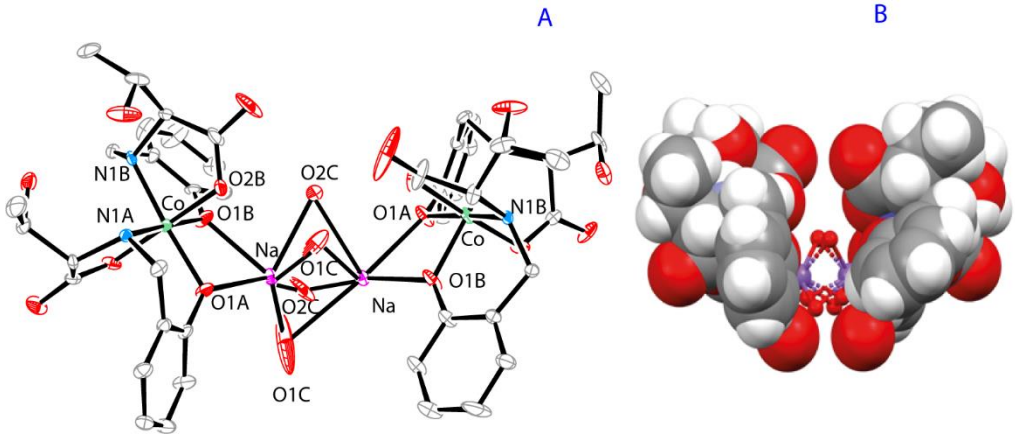

Fig 5.1. ORTEP diagram of Complex **1** with thermal ellipsoid set at 40 % probability (A) and space-filled model (B).

The complex has a facial geometry, with the two -NH amide group, the two phenolates in *cis* orientation and the two carboxylates in *trans* orientation. Na^+ ion is coordinated with the two cis-oriented phenolates and two water molecules in an asymmetric unit (Figure 5.2A) and is further coordinated with the other two water molecules of other units. Each Na^+ ion is hexacoordinated by four bridging water molecules and two phenolates. The two Na^+ ions are sandwiched by two Co(III) monomeric units acting as dimers (Figure 5.1B). The two carboxylates of the dimers are in short contact with the two Na^+ ions of the neighbouring dimer and so on, thereby forming a coordination polymer. The ligand in the complex has two chiral carbon centres, C8A and C9A, with *R* and *S* configurations, respectively, as the amino acid used in ligand synthesis has two chiral centres with *R* and *S* conformation. In addition to the asymmetric carbon centres in the ligand, the coordination of amine N1A to the Co(III) gives rise to asymmetric secondary nitrogen atoms and shows the *R* configuration. This phenomenon of opposite conformation preference at chiral Carbon and amine N has been observed in all the characterized complexes of this type of ligand.[24–26]

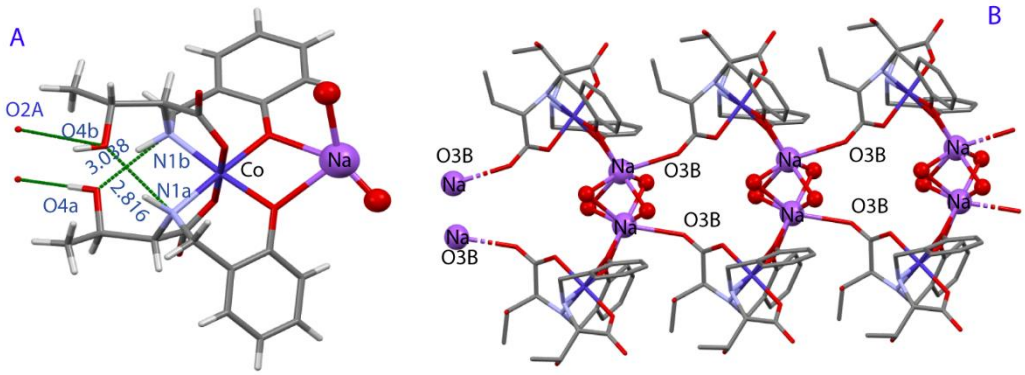

Fig 5.2. Ball and stick model of complex **1** (A) showing the intramolecular hydrogen bonding and (B) polymeric chain formation.

The selected bond lengths and angles of complex **1** are given in Table 5.2. The amide N1A is hydrogen bonded with the oxygen atom (O4B) of the other ligands' amino acid side chain, and the oxygen atom (O4B) is again hydrogen bonded with the carboxylates (O2A) of the neighbouring molecules. Two such inter-ligands hydrogen bonds exist in one monomeric unit (Fig 5.2A). We expect this could be the reason for obtaining facial geometry for the $L^{L\text{-thr}}$ ligand complexes, which have a hydrophilic, hydrogen bond-capable amino acid side chain. The non-covalent interaction of complex **1** is given in table 5.3. The hydrogen bond lengths (O4a…N1b and O4b…N1a) are 2.816 and 3.038 Å, respectively (Fig 5.2), consistent with the normal

hydrogen bond length. A cavity is formed in every dimer structure (Fig 5.1B), which can be used for trapping the molecules. The carboxylate (O3B) in every dimer is in short contact with the neighbouring Na atom, forming a coordination polymer, as shown in Fig 4.2B. This could be the reason for the poor solubility of this complex in organic solvents.[27]

5.5.2. [Zn{Co($L^{L\text{-}thr}$)$_2$}$_2$(H_2O)] (4). The Complex **4** crystallizes out in the space group *P 21 21 21* in an orthorhombic crystal system. The selected bond length and angles of the complex are given in Table 3.2. It has two Co(III) metal centres and one Zn(II) metal centre. The two Co(III) metal centres are coordinated by two tridentate ligands, which are doubly deprotonated, obtaining the facial, octahedral geometry, in which the carboxylates are in *trans* orientation and the amide NH, and the phenolates are in *cis* orientation (Fig 5.3A). The ligands in the complex have two chiral carbon centres, C8A and C9A, with *R* and *S* configurations, respectively, as the amino acid used in ligand synthesis has two chiral centres with *R* and *S* conformation. In addition to the asymmetric carbon centres in the ligand, the coordination of amine N1A to the Co(III) gives rise to asymmetric secondary nitrogen atoms and shows the *R* configuration. This phenomenon of opposite conformation preference at chiral Carbon and amine N has been observed in all the characterized complexes of this type of ligand.

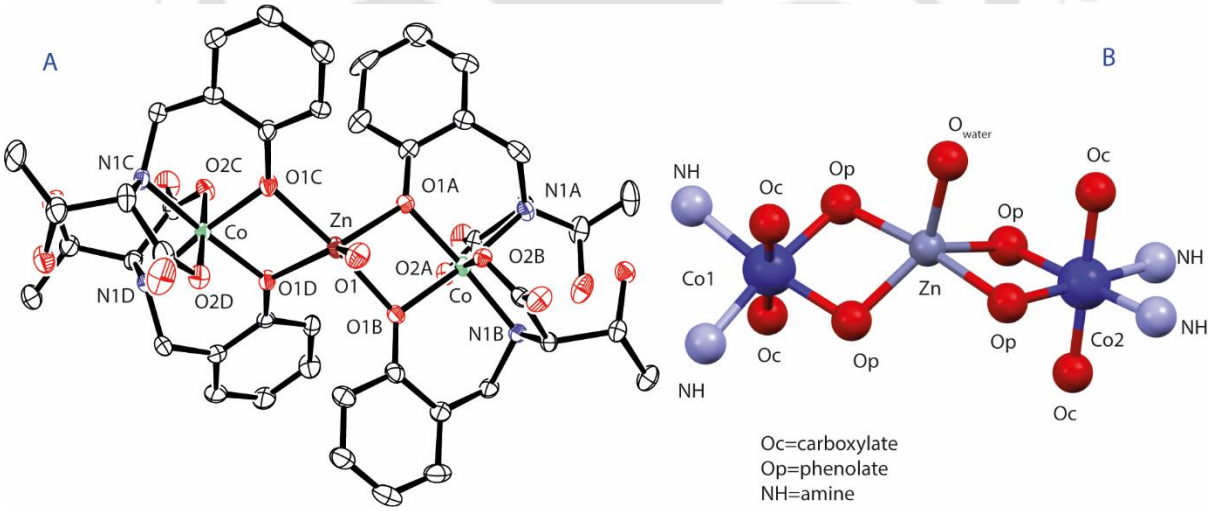

Fig 5.3. ORTEP diagram of Complex **3** with thermal ellipsoid set at 40 % probability (A) and Ball and stick model of the complex depicting the coordination sphere (B).

The amide N1A is hydrogen bonded with the oxygen atom (O4B) of the other ligands' amino acid side chain, and the oxygen atom (O4B) is again hydrogen bonded with the water molecule (O4), which is further hydrogen bonded with the neighbouring carboxylate (O3C) molecules.

Two such inter-ligands hydrogen bonds exist in one Co(III) unit similar to the complex **1** (Fig 5.1B).

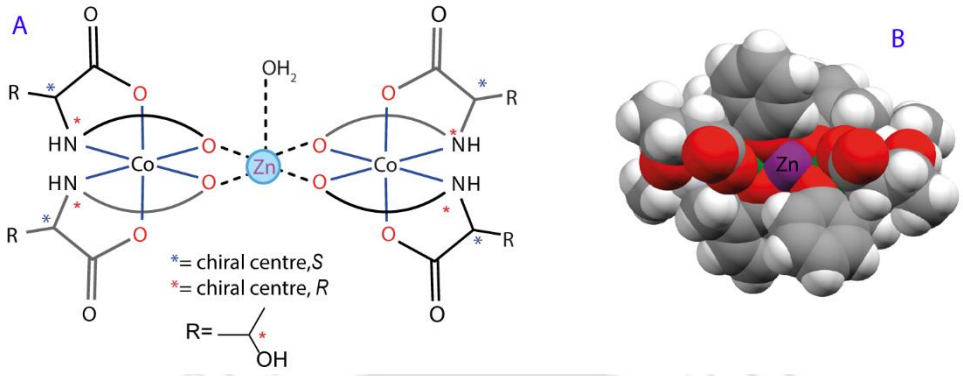

Fig 5.4 Sketch model of complex **4** (A) and space-filled model of the complex depicting the labile accessible Zn(II) centre.

The deviation of bond angles from 90° and 180° indicates that the Co(III) unit has a distorted octahedral geometry. The O1A-Co1-O1B deviated the most at 80.8° from 90°, and O1A-Co1-N1A deviated the most at 172.9° from 180°. The Zn(II) metal centre is coordinated with the two Co(III) units of *cis*-oriented phenolates and one free water molecule. The Zn(II) is slightly above the plane with a distance of 0.46 Å, thereby obtaining a distorted square pyramidal geometry around the Zn(II) centre. The water molecule binds with Zn(II) at an angle of approximately 128.95° from the plane, and the axial bond length Zn-O1(2.043 Å) is slightly longer than the known reported Zn-O bond length.[28–31] Structural characterization shows that the Zn(II) at the centre is surrounded by H-bond capable carboxylates within the C2 symmetric chiral environment. The Penta-coordinated Zn(II) has an easily replaceable water molecule in the axial position. The resultant architecture where a Zn(II) bound water surrounded by an H-bond capable chiral environment is reminiscent of the active site of hydrolytic enzymes (Fig 4.4A).[32–34] The space-filled model shows that the central metal ion Zn(II) is accessible.

5.5.3. $[Cu\{Co(L^{L\text{-}thr})_2\}_2(H_2O)]$ (4). Complex **5,** which has Cu(II) as a central metal ion, has a similar solid-state structure to its Zn(II) analogue, complex **4**. The crystal parameters are given in Table 5.1, and the selected bond length and angles of the complex are given in Table 5.2. The Zn(II) is slightly above the plane with a distance of 0.46 Å, whereas the Cu(II) in complex **5** is 0.44 Å above the plane. Hence, complex **5** is less distorted than Complex **4.** As expected, the axial bound labile water molecules with Cu-Owater (2.101 Å) bond length is slightly longer than the Zn-Owater (2.043 Å) bond length for copper complexes.[35–38]

Table 5.2 Selected bond length (Å) and angles (°) of complexes **1, 4,** and **5.**

	Co-Oc	Co-Op	Na-Op	Co-NH	Zn-Op	Zn-Ow
1	1.875(8), 1.900(8)	1.933(9), 1.904(8)	2.349(9), 2.303(10)	1.950(8), 1.936(8)		
3	1.874(7), 1.884(7), 1.889(7), 1.861(7)	1.892(7), 1.908(6), 1.901(6), 1.920(7)		1.939(7), 1.932(7), 1.936(8), 1.9790(7)	1.976(7), 2.045(8), 2.062(7), 1.982(6)	2.049(9)
					Cu-Op	Cu-Ow
4	1.876(6), 1.905(5), 1.878(5), 1.879(5)	1.912(5) 1.928(5), 1.929(4) 1.897(5)		1.949(6), 1.942(5), 1.949(4), 1.848(5)	2.053(5), 1.953(5), 1.955(5), 1.951(5)	2.101(6)
	Oc-Co-Oc	Op-Co-Op	NH-Co-NH	Op-Na-Op		
1	176.4(4)	82.2(4)	1.950(8)	67.0(3)		
				Op-Zn-Op	Op-Zn-Ow	
4	179.5(3), 179.7(3)	80.8(3), 81.7(3)	93.3(3), 92.4(3)	75.5(3), 128.5(3)	129.0(3), 95.4(3),	
				Op-Cu-Op	Op-Cu-Ow	
5	178.5(2), 179.03(3)	80.6(3), 80.1((19)	93.3(3), 93.3(3)	76.9(19), 103.9(2)	69.6(2), 132.2(2)	

Oc, Op, NH, and Ow represent carboxylate, phenolate, amine, and water, respectively.

Table 5.3. Non-covalent interactions in complexes **1**,**4**, and **5**.

Complex 1	D-H…A	D-H (Å)	H…A(Å)	D…A(Å)	DHA (°)
	C9B-H1B…O1B	0.9800	2.5400	3.427(15)	151.00
	C7B -H7BB… O2A	0.9700	2.5500	3.015(13)	110.00
	N1A-H1A…O4B	0.9800	2.1100	3.041(13)	159.00
	N1B-H1B…O4A	0.9800	1.9300	2.831(12)	152.00
Complex 4	N1A-H1A…O4B	0.9800	2.2400	3.178(12)	159.00
	N1B-H1B…O4A	0.9800	2.1000	3.035(13)	160.00
	N1C-H1C…O4D	0.9800	1.9600	2.893(12)	158.00
	N1D-H1D…O4C	0.9800	1.9900	2.920(11)	159.00
	C4C-H4A…O2D	0.9300	2.4600	3.341(12)	159.00
Complex 5	N1A-H43…O4B	0.9800	2.2000	2.941(7)	159.00
	N1B-H11…O4A	0.9800	1.9500	2.884(7)	159.00
	N1C-H27…O4D	0.9800	2.1100	3.052(9)	160.00
	N1D-H59…O4C	0.9800	2.2600	3.181(8)	157.00
	C4D-H54…O2A	0.9300	2.4900	3.384(9)	163.00

5.6. NMR spectroscopy

The ^{1}H and ^{13}C NMR spectra of the ligand and all the complexes are well-defined, and their signals can be easily assigned according to their structures. Table 4.6 summarizes the NMR data for these complexes. ^{1}H NMR of $H_2L^{L\text{-}thr}$ and all the complexes was recorded in DMSO-d_6 at 500 MHz. Since some of the proton positions overlapped, we used the 2D ^{1}H NMR spectroscopic technique to assign all the respective protons' possible peak positions. The exchangeable proton -NH and -OH are not detected in the ^{1}H NMR spectra of the ligand (Fig 4.5).

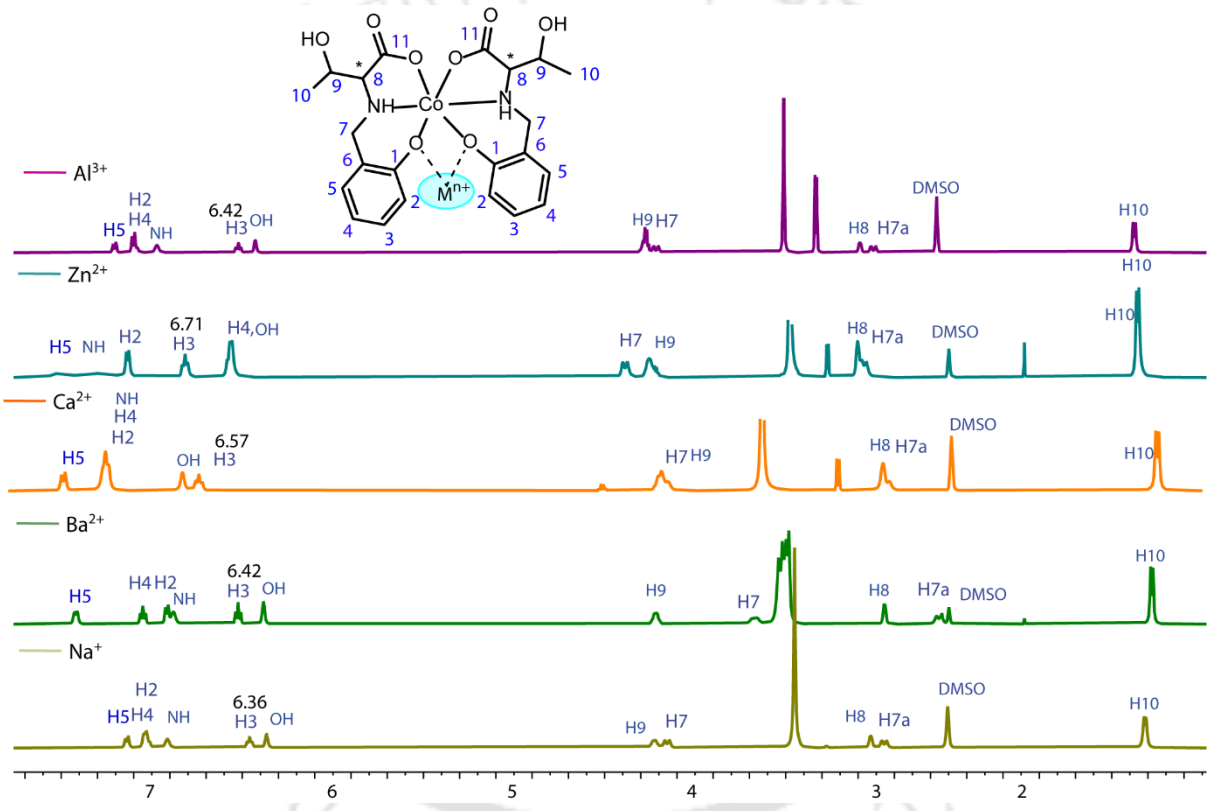

Figure 5.5. Combine ^{1}H NMR spectra of **$H_2L^{L\text{-}thr}$**, complex **1**, **2**, **3**, **4** and **6**

The ^{1}H NMR of all the complexes has been sharp and well-resolved resonance spectra, indicating the formation of complexes that are likely low-spin diamagnetic complexes except for complex **5**. The assignment of protons and Carbon was additionally corroborated with the 2D-COSY spectra and HSQC spectra as some protons' positions overlapped, and there are diastereotopic protons. Here, we observe and assign the -OH and -NH peaks in the complex spectra, which are absent in the ligand spectra.

Table 5.4. ^{1}H NMR peak position for the complexes.

		Peak position (ppm)				
labelled	$H_2L^{L\text{-}thr}$	**1**	**2**	**3**	**4**	**6**
	^{1}H	^{1}H	^{1}H	^{1}H	^{1}H	^{1}H
11						
10	1.18 (d 6H)	1.41 (d 6H)	1.38 (d 6H)	1.45(d 6H)	1.46 (d 6H)	1.47(d 6H)
9	3.90 (m 2H)	4.12 (m 2H)	4.13 (m 2H)	4.09(m 2H)	4.17 (m 2H)	4.18(m 2H)
8	3.06 (m 2H)	2.93 (m 2H)	2.86 (m 2H)	2.91(m 2H)	3.00 (m 2H)	2.99(m 2H)
7	4.05 (d 2H)	4.05 (d 2H)	3.58 (d 2H)	4.09(m 2H)	4.30 (d 2H)	4.12(m 2H)
7a	4.05 (d 2H)	2.86 (d 2H)	2.55 (d 2H)	2.87(m 2H)	2.96 (d 2H)	2.91(m 2H)
5	7.25 (d 2H)	7.04 (d 2H)	7.32 (d 2H)	7.30(d 2H)	7.40 (d 2H)	7.10(d 2H)
6						
4	6.91 (t 2H)	6.95 (t 2H)	6.95 (t 2H)	7.06(m 2H)	6.47 (m 2H)	6.99(m 2H)
3	6.78 (t 2H)	6.36 (m 2H)	6.42 (m 2H)	6.57(t 2H)	6.71 (t 2H)	6.42(t 2H)
2	6.80 (d 2H)	6.95 (m 2H)	6.81 (m 2H)	7.06(m 2H)	7.03 (s 2H)	6.99(m 2H)
1						
NH		6.81 (s 2H)	6.80 (s 2H)	7.06(s 2H)	7.17 (s 2H)	6.87(s 2H)
OH		6.27 (s 2H)	6.28 (s 2H)	6.65(s 2H)	6.44 (s 2H)	6.33(s 2H)

We compared the spectra of the complexes. We noticed the downfield shift, primarily the phenol aromatic protons, shifted significantly (Figure 4.5). This is due to the binding of the secondary cation with the Co(III) bis complex through the phenolates, as the phenoxide electron charge density presumably decreases upon the coordination of secondary cations, and this phenomenon exacerbates more as we move from Na^{+} to Zn^{2+}. Therefore, this effect can be summarised as the secondary cation-induced downfield shift of aromatic phenol protons. However, in order to estimate the magnitude of the downfield shift induced, we tried to explain in terms of the charge/ionic radius ratio of the secondary cation, also known as the polarising power of the cation. We calculate the charge/ionic size ratio value of the secondary cations of the complexes (Table 5.5) and plot the graph against the downfield shift of the aromatic phenol proton. We choose H3 as its peaks are well resolved and do not overlap with other proton peaks in all the complexes spectra.

Table 5.5. polarising power of the cation data.

M^{n+}	charge	Ionic size(Å)	Charge/ionic size	^{1}H NMR Peak position of H3
Na^{+}	+1	1.02	0.98	6.36
Ba^{2+}	+2	1.35	1.48	6.42
Ca^{2+}	+2	1.06	1.88	6.57
Zn^{2+}	+2	0.74	2.7	6.71
Al^{3+}	+3	0.54	5.6	6.42

We obtained a linear graph (Fig 5.6) suggesting that the downfield shift of the aromatic phenol protons is directly proportional to the polarising power of the secondary cation. We expect the aromatic phenol protons' of complex **6** to have maximum downfield shift if Al^{3+} bind. However, the spectra of complex **6** look similar to that of complex **1** except for a slight peak position shift. This suggests that Al^{3+} does not bind with the complex. Instead, it protonates due to its Lewis acidity nature. Hence, we could not consider Complex **6** to follow the pattern of downfield shift, so we ignored the data of Complex **6** and did not include it in the graph plotting. Thus, we can detect the spectroscopically silent metal ions in solution by ^{1}H NMR.

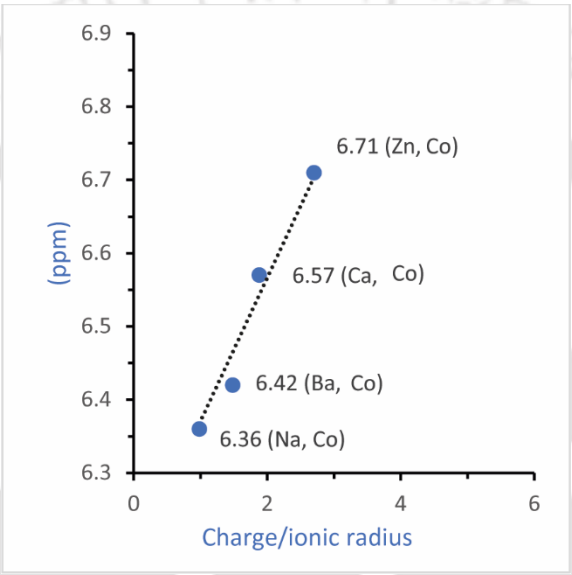

Figure 5.6. ^{1}H NMR shift of H3 Vs charge/ionic radius plot

Large deshielding of the NH protons is attributed to the increase in π electron density in the C–N bond upon coordination.[39] In all the complexes, resolved singlets for the protons of the NH groups are observed in their ^{1}H NMR spectra (see Fig 5.5). On the other hand, the chiral centre protons H8 and H9, as well as the diastereotopic protons 7 and 7a, have minimal or in reverse order of upfield shift (Fig 5.5 and Table 5.5), as the effect of the secondary cation on these protons are minimal since the rigid inert Co(III) coordinated with the amine, phenolates, and carboxylates are further away from the secondary cation.

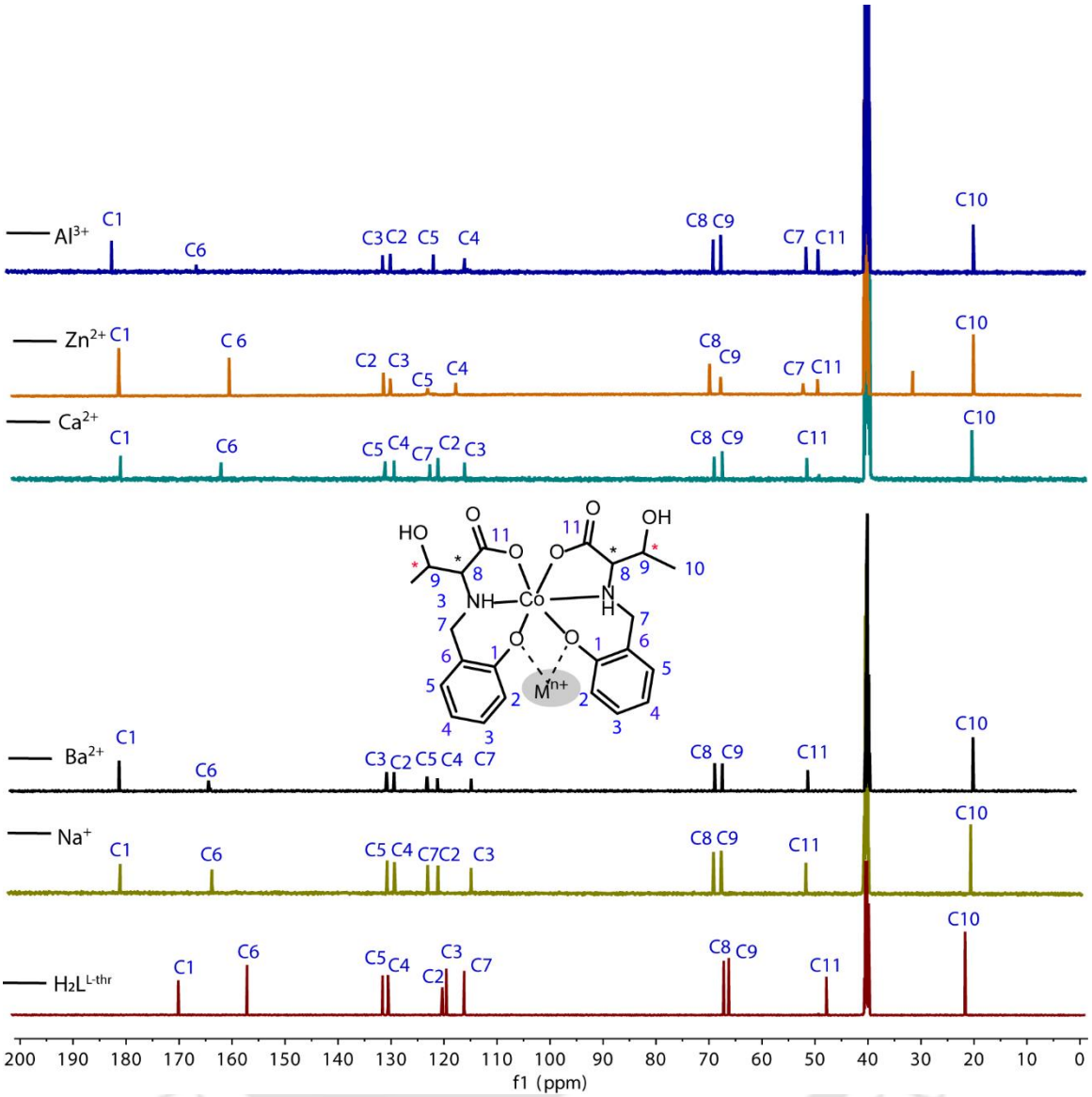

Figure 5.7. Combine ^{13}C NMR spectra of ligand and complexes.

The ^{13}C NMR signals are all shifted downfield to a maximum of 10 ppm. This is due to the binding of the secondary cation with the Co(III) bis complex through the phenolates, as the phenoxide electron charge density presumably decreases upon the coordination of secondary cations, and this phenomenon exacerbates more as we move from Complex **1** to **6** as their polarising power increases. However, the complex **6** carbon peak does not shift as expected (Fig 5.7). This also indicates that Al^{3+} does bind with the Co(III) complex.

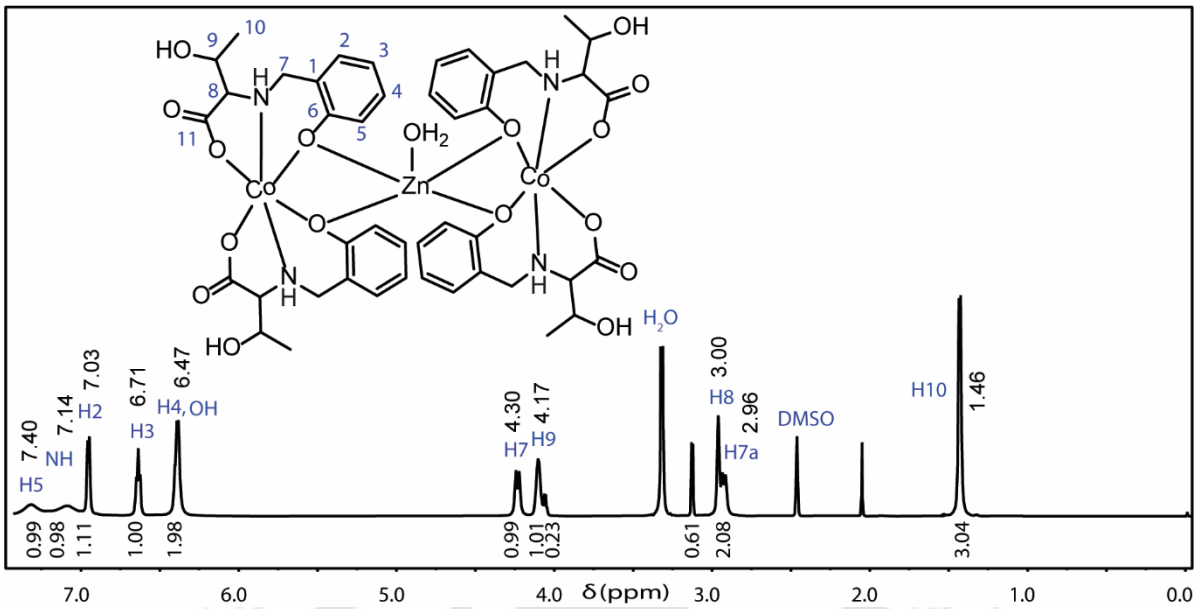

Figure 5.8. ^{1}H NMR spectra of complex **4**

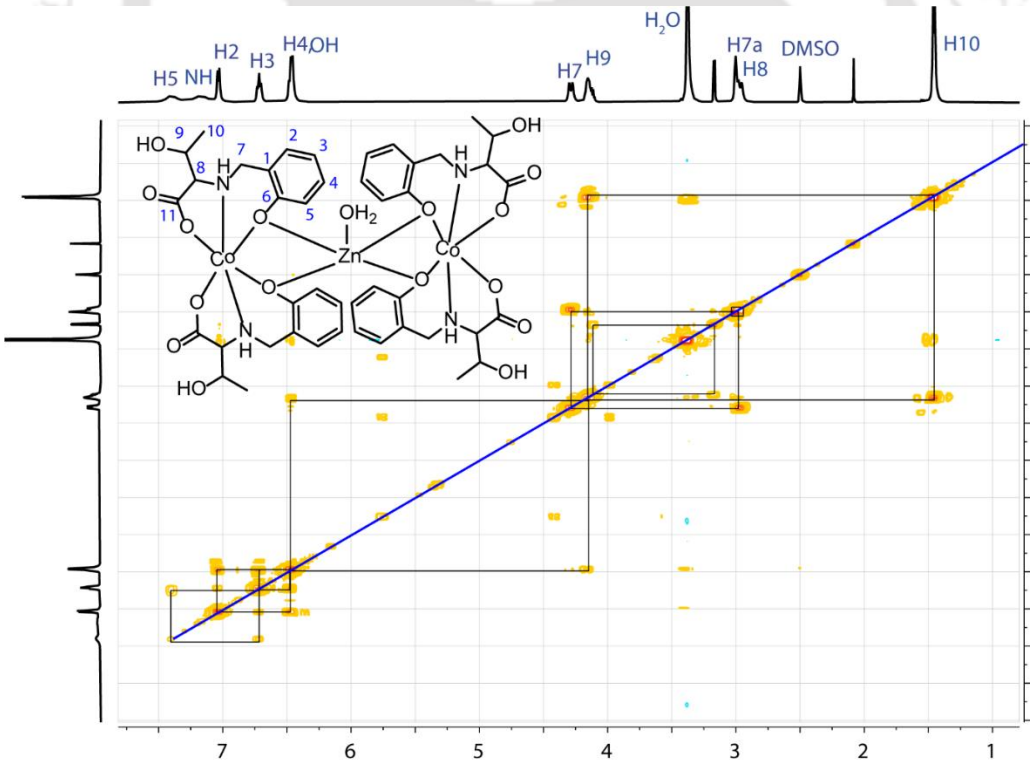

Figure 5.9. 2D-COSY spectra of complex **4**

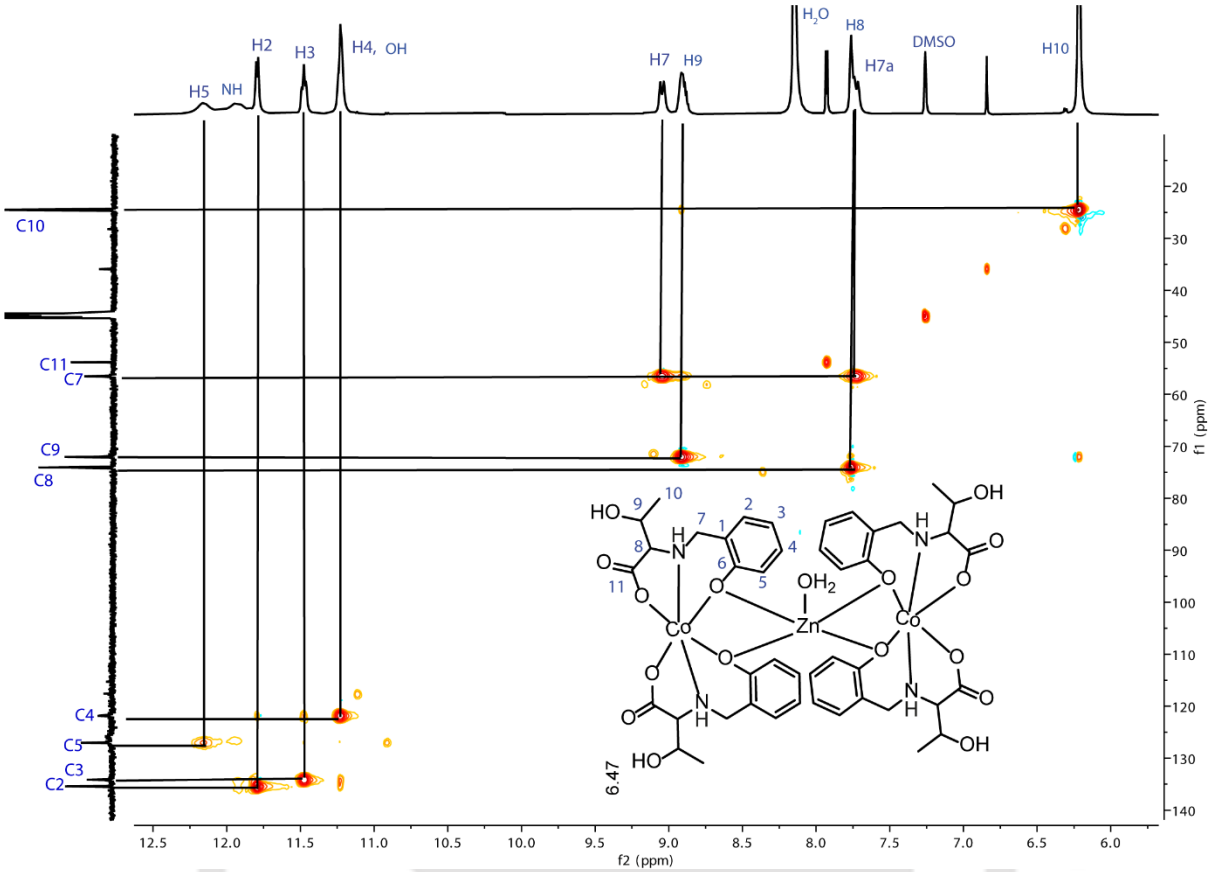

Figure 5.10. 2D-HSQC spectra of complex **4**

5.7. ESI-Mass spectrometry

The ESI-Mass spectra of all the complexes were recorded in ESI-MS(M^-). Complex **1** was recorded in methanol, and it shows the matching isotopic pattern (ESI-MS): m/z, $[Co(L^{L\text{-}thr})_2]^-$ calcd: 505.102 found 505.104, and isotopic pattern at 1011.21 corresponds to $[\{Co(L^{L\text{-}thr})_2\}_2+H]^-$, and isotopic pattern found at 1033.19 is matching with $[Na\{Co(L^{L\text{-}thr})_4\}]^-$ (Figure 4.11 and Table 4.6). The mass spectra of **1** give us the evidence that the Na^+ ion is bound with the Co(III) bis complex in the solution. The ESI-Mass spectra of complexes **2** and **3** only show the isotopic pattern of $[Co(L^{L\text{-}thr})_2]^-$ at 505.102 and 505.103, respectively. We could not get the evidence of Ba and Ca bound with the complex from the Mass spectra. The mass spectra of complexes **4** and **5** were recorded in MeOH. Both spectra show the isotopic patterns of $[Co(L^{L\text{-}thr})_2]^-$ and the isotopic pattern corresponding to $[Zn\{Co(L^{L\text{-}thr})_2\}\text{-}H]^-$ and $[Cu\{Co(L^{L\text{-}thr})_2\}\text{-}H]^-$ respectively (Fig 4.12 and 4.13), indicating that the linear trinuclear complexes identity are retained in the solution.

Table 5.6. Mass spectral data.[a]

	calc. m/Z (relative intensity)[b]	exp. m/Z (relative intensity)[b]
1	505.102(100), 506.102(25) 507.102(4)	505.104(100), 506.104(23) 507.104(7)
2	505.102(100), 506.102(25) 507.102(4)	505.102(100), 506.105(25) 507.107(4)
3	505.102(100), 506.102(25) 507.102(4)	505.103(100), 506.105(25) 507.108(5)
4	1073.125 (100), 1074.125(50), 1075.125 (73), 1076.125(41), 1077.125(52), 1078.125(23), 1079.125(8)	1073.128(100), 1074.122(55), 1075.125 (71), 1076.125(40), 1077.125(52), 1078.126(25), 1079.125(9)
5	1072.135 (100), 1073.135 (50), 1074.135(60), 1075.135 (26), 1076.135(7), 1077.135(1)	1072.128 (100), 1073.132 (54), 1074.132(66), 1075.132 (25), 1076.1325), 1077.135(1)

[a] in MeOH, [b] isotopic mass distribution of molecular ion peak with relative intensity values in parenthesis. **1**=Na[Co($L^{L\text{-}thr}$)$_2$], **2**=[Ba{Co($L^{L\text{-}thr}$)$_2$}$_2$], **3**=[Ca{Co($L^{L\text{-}thr}$)$_2$}$_2$] **4**=[Zn{Co($L^{L\text{-}thr}$)$_2$}$_2$], and **5**=[Cu{Co($L^{L\text{-}thr}$)$_2$}$_2$]

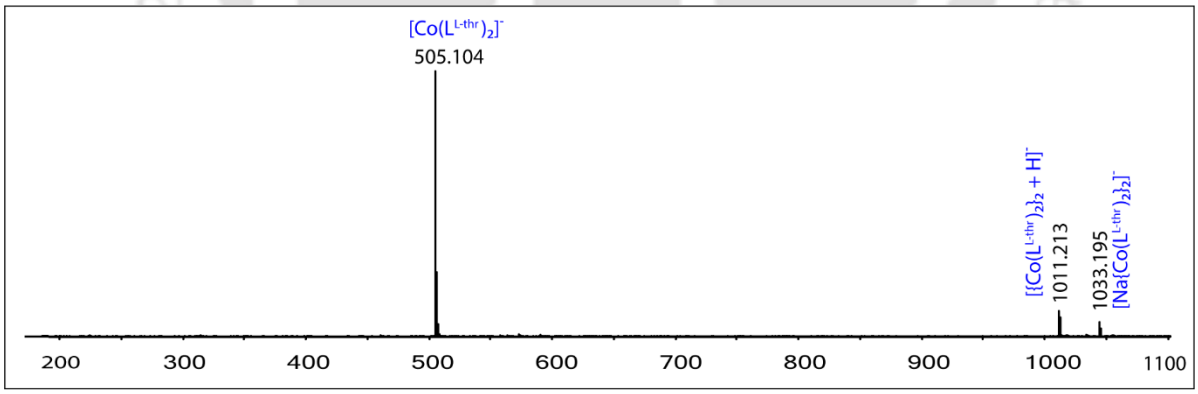

Figure 5.11. ESI-Mass spectra of **1** (-ve) in MeOH

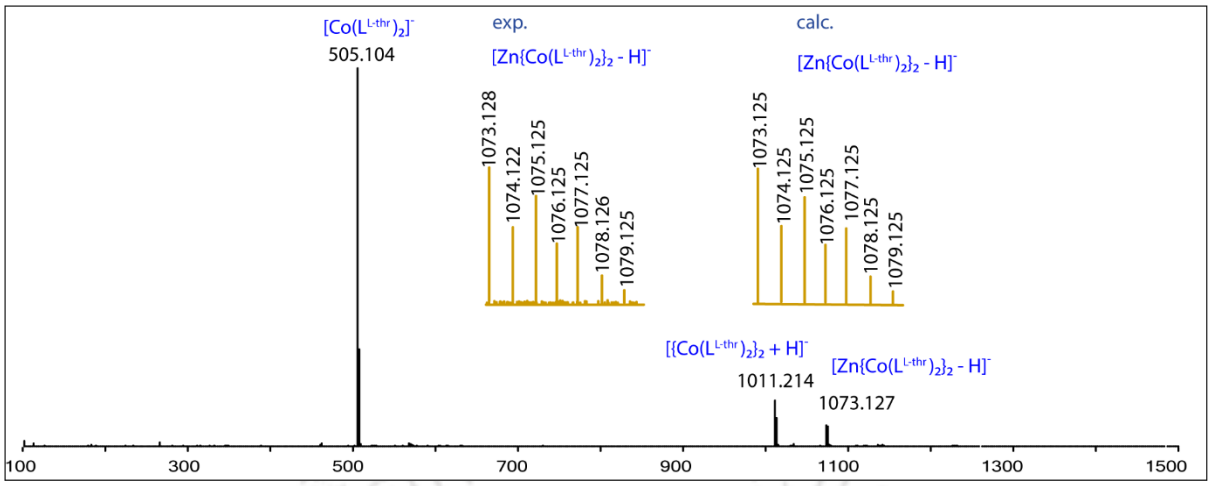

Figure 5.12. ESI-Mass spectra of **4** (-ve) in MeOH

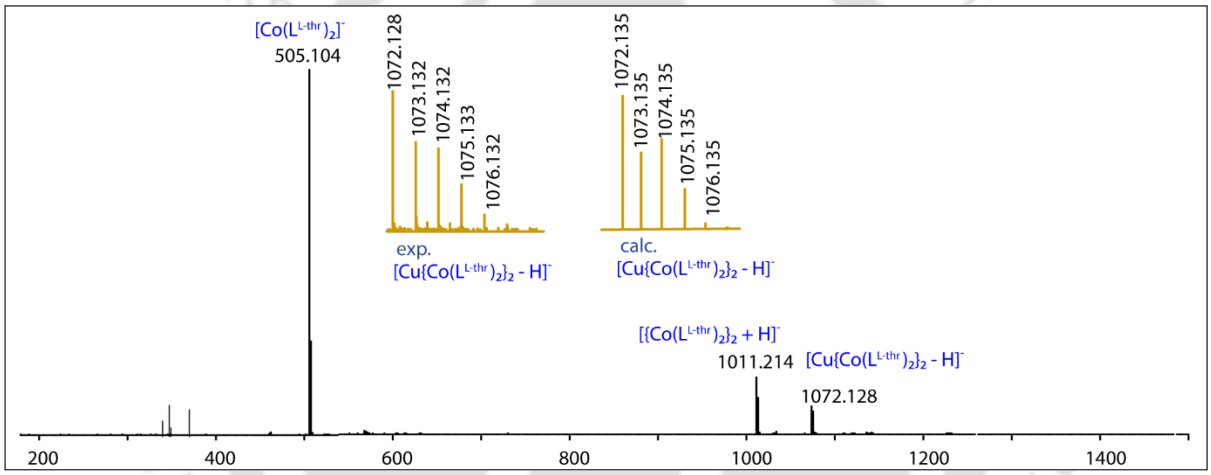

Figure 5.13. ESI-Mass spectra of **5** (-ve) in MeOH

5.8. UV-visible spectroscopy

The UV-vis spectra of all the complexes are carried out in a MeOH medium at room temperature. The electronic spectrum of each complex consists of a band at around ~350 nm. (ε = ~500). These bands are assigned as ligand-to-metal charge transfer transitions. In any low-spin cobalt(III) complex, two spins allowed d–d transitions. ^{1}A1g → ^{1} T1g and ^{1}A1g → ^{1}T2g are expected.[40,41] The band around 600 to 650 nm in the absorption spectrum of each complex may be attributed to one of these two expected transitions. The spin-allowed transition is obscured by a strong LMCT transition ~350 nm.[42] The complexes' electronic spectra are jointly presented in Fig 5.14. The blueshift of the d-d transition of the complexes as we go from complex **1** to **4** is evident in Figure 5.14 and Table 5.7.

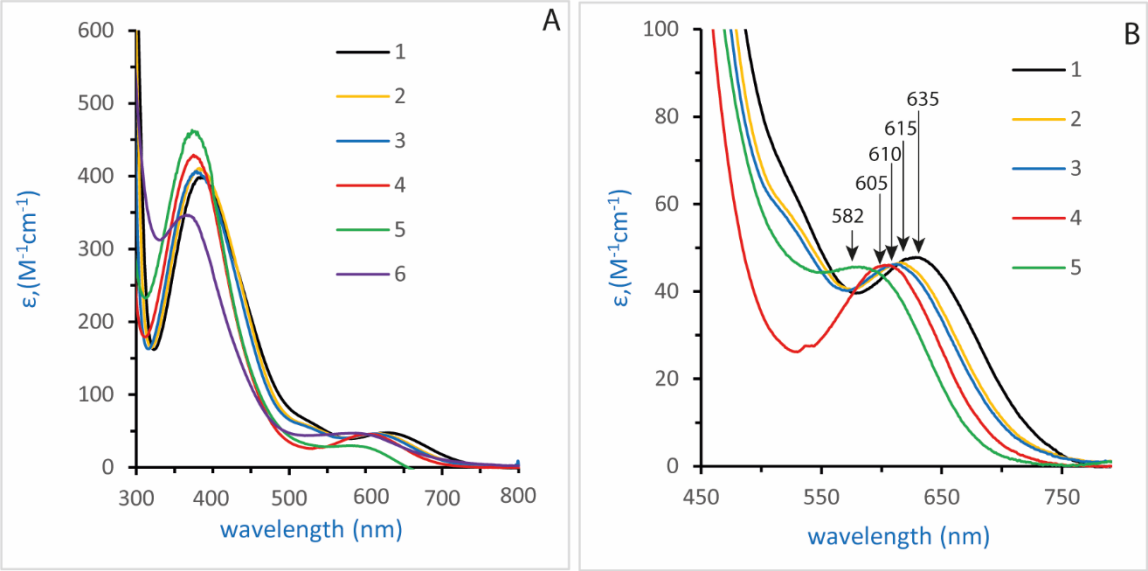

Fig 5.14. UV-visible spectra of the complexes in MeOH

The solid-state characterization (section 5.5) shows that the Co(III) bis complex remains the same in all the complexes. This indicates that the spectroscopically silent metal ions (Na^{+}, Ba^{2+}, $Ca^{2+,}$ and Zn^{2+}) cause minor perturbation in the ligand strengths around the Co(III). This observation provides an interesting way to distinguish the spectroscopically silent metal ions in the visible region. We think the difference in the charge and the size of the cation coordinating through the phenolate might have influenced the ligand field strength. It's worth mentioning that the value of complex **5,** which has d-d transition λ_{max} at 582 nm, is slightly out of touch with the linear trend. This could be due to the Cu(II) metal ion as Cu(II) itself has its own d-d transition around this region.[43–47] We studied the dependence of the λ_{max} values (i.e., charge transfer energies) on charge/ionic size for the heterobimetallic [Co(III), M]. The shift of the charge transfer energy to higher values in the complexes studied here can be ascribed to stabilizing the occupied orbitals on the metal. The stabilization of the metal-centred HOMO is achieved by the interaction of the Lewis acidic secondary metals with the bridging phenolate donors that are bound to the Co(III) centre.[48]

Table 5.7 Electronic spectral data.[a]

Complex	**1**	**2**	**3**	**4**	**5**	**6**
λ_{max}, (ε, $M^{-1}cm^{-1}$)	393(396)	386(413)	382(416)	372(426)	368(471)	367(346)
	635(49)	615(45)	610(43)	605(40)	582(42)	587(47)

[a] Scan range in MeOH, 200-800. ε values calculated using ~0.5 mM solutions.

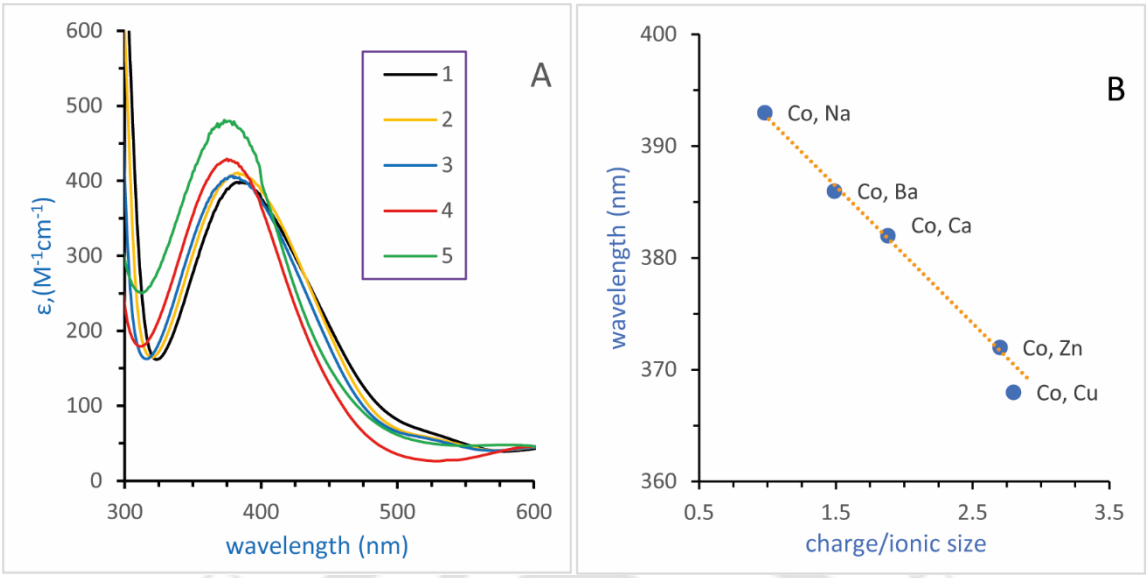

Fig 5.15. electronic absorption spectra of the complexes in MeOH (A) and plot of LMCT band shift vs charge/ionic size (B)

The effect of the redox-inactive cations on the ligand-centred LUMO orbitals, however, must be more modest in comparison to the shifts induced at the Co(III) centre, with the net result of the widening of the HOMO-LUMO gap that drives the shifts in the charge transfer band energies.[49] As the anticipated change in donor power of the phenoxide ligands could be modelled as a shift in oxygen-centred charge density, it is unsurprising that the preferred descriptor for the changes in the UV-visible spectra is the polarising power of the incorporated secondary metal ions. We expect complex **6** to have maximum blue shift if Al^{3+} bind. However, the spectra of complex **6** do not shift as predicted. This suggests that Al^{3+} does not bind with the complex. Instead, it protonates due to its Lewis acidity nature. Hence, we could not consider Complex **6** to follow the pattern of blue shift, so we ignored the data of Complex **6** and did not include it in the graph plotting. This agrees with the conclusion from ^{1}H NMR that Al^{3+} does not bind with the Co(III) bis complex. We plot the graph of the band shift of the LMCT versus the charge/ionic size of the corresponding heterobimetallic, revealing a uniform, linear trend (Fig 5.15), suggesting that the LMCT band blue is directly proportional to the polarising power of the secondary cation. [50,51] With this information, we can also detect the spectroscopically silent metal ions by UV-visible spectroscopy.

5.9. Conclusion

In this chapter, we have successfully synthesized inert Co(III) complexes of L-threonine-derived ligand. We also replace the secondary cations of different sizes and charges. Unlike the Cu(II) version, which forms the cyclic trinuclear when binding with a cation, Co(III) complexes, when bound with the cation, form a linear heterobimetallic complex. Structural characterization of complexes **4** and **5** shows that the Zn(II) and Cu(II) at the centre are surrounded by H-bond capable carboxylates within the C_2 symmetric chiral environment. The Penta-coordinated Zn(II) and Cu(II) have an easily replaceable water molecule in the axial position. The resultant architecture where a Zn(II) and Cu(II) bound water surrounded by an H-bond capable chiral environment is reminiscent of the active site of hydrolytic enzymes. We can use ^{1}H NMR and UV-visible spectroscopy to detect the spectroscopically silent metal ions in the solution. We also established how the polarising power of the cations relates directly to the UV-visible LMCT band shift and the proton's downfield shift in ^{1}H NMR.

5.10. References

1 M. L. Saha and M. Schmittel, *Inorg. Chem.*, 2016, **55**, 12366–12375.

2 J. E. M. Lewis and James. D. Crowley, *ChemPlusChem*, 2020, **85**, 815–827.

3 G. González-Riopedre, M. R. Bermejo, M. I. Fernández-García, A. M. González-Noya, R. Pedrido, M. J. Rodríguez-Doutón and M. Maneiro, *Inorg. Chem.*, 2015, **54**, 2512–2521.

4 D. Bansal, G. Hundal and R. Gupta, *Eur. J. Inorg. Chem.*, 2015, **2015**, 1022–1032.

5 K. Ghosh, K. Harms, A. Bauzá, A. Frontera and S. Chattopadhyay, *Dalton Trans.*, 2018, **47**, 331–347.

6 S. Roy, A. Bhattacharyya, S. Purkait, A. Bauzá, A. Frontera and S. Chattopadhyay, *Dalton Trans.*, 2016, **45**, 15048–15059.

7 K. Ghosh, K. Harms, A. Bauzá, A. Frontera and S. Chattopadhyay, *CrystEngComm*, 2018, **20**, 7281–7292.

8 A. Mishra, A. Ali, S. Upreti and R. Gupta, *Inorg. Chem.*, 2008, **47**, 154–161.

9 G. Kumar, A. P. Singh and R. Gupta, *Eur. J. Inorg. Chem.*, 2010, **2010**, 5103–5112.

10 N. F. Ghazali, K. R. Vignesh, W. Phonsri, K. S. Murray, P. C. Junk, G. B. Deacon and D. R. Turner, *Dalton Trans.*, 2022, **51**, 18502–18513.

11 C. Schulte To Brinke and F. E. Hahn, *Eur. J. Inorg. Chem.*, 2015, **2015**, 3227–3231.

12 N. W. Alcock, G. Clarkson, P. B. Glover, G. A. Lawrance, P. Moore and M. Napitupulu, *Dalton Trans*, 2005, 518–527.

13 E. V. Eames, R. Hernández Sánchez and T. A. Betley, *Inorg. Chem.*, 2013, **52**, 5006–5012.

14 S. Terashima, G. N. Newton, T. Shiga and H. Oshio, *Inorg. Chem. Front.*, 2015, **2**, 125–128.

15 B. Jana, L. Cera, B. Akhuli, S. Naskar, C. A. Schalley and P. Ghosh, *Inorg. Chem.*, 2017, **56**, 12505–12513.

16 V. Chandrasekhar, B. M. Pandian, R. Boomishankar, A. Steiner, J. J. Vittal, A. Houri and R. Clérac, *Inorg. Chem.*, 2008, **47**, 4918–4929.

17 V. Chandrasekhar, B. M. Pandian, R. Boomishankar, A. Steiner and R. Clérac, *Dalton Trans.*, 2008, 5143.

18 D. Visinescu, J.-P. Sutter, C. Ruiz-Pérez and M. Andruh, *Inorganica Chim. Acta*, 2006, **359**, 433–440.

19 K. L. Bushell, S. M. Couchman, J. C. Jeffery, L. H. Rees and M. D. Ward, *J. Chem. Soc. Dalton Trans.*, 1998, 3397–3404.

20 CrysAlis CCD and CrysAlis RED. Oxford Diffraction Ltd, Yarnton, Oxfordshire, England. Oxford Diffraction, 2009.

21 G. M. Sheldrick, Acta Crystallogr., Sect. A: Fundam. Crystallogr., 2008, A64, 112.

22 M. N. Burnett and C. K. Johnson, ORTEP-III, Oak Ridge National Laboratory Report ORNL-6895, 1996.

23 W. J. Geary, *Coord. Chem. Rev.*, 1971, **7**, 81–122.

24 Md. A. Alam, M. Nethaji and M. Ray, *Angew. Chem. Int. Ed.*, 2003, **42**, 1940–1942.

25 M. Dubey, R. R. Koner and M. Ray, *Inorg. Chem.*, 2009, **48**, 9294–9302.

26 R. Ganguly, B. Sreenivasulu and J. J. Vittal, *Coord. Chem. Rev.*, 2008, **252**, 1027–1050.

27 E. R. Engel and J. L. Scott, *Green Chem.*, 2020, **22**, 3693–3715.

28 U. Seetawan, S. Jugsujinda, T. Seetawan, A. Ratchasin, C. Euvananont, C. Junin, C. Thanachayanont and P. Chainaronk, *Mater. Sci. Appl.*, 2011, **02**, 1302–1306.

29 N. L. Marana, S. Casassa, E. Longo and J. R. Sambrano, *J. Phys. Chem. C*, 2016, **120**, 6814–6823.

30 Q. Umar, Y. H. Huang, A. Nazeer, H. Yin, J. C. Zhang, M. Luo and X. G. Meng, *RSC Adv.*, 2022, **12**, 32119–32128.

31 D. Ejarque, T. Calvet, M. Font-Bardia and J. Pons, *Molecules*, 2020, **25**, 3615.

32 L. F. Serafim, V. M. Jayasinghe-Arachchige, L. Wang, P. Rathee, J. Yang, S. Moorkkannur N. and R. Prabhakar, *Chem. Commun.*, 2023, **59**, 8911–8928.

33 M. Zhao, H.-B. Wang, L.-N. Ji and Z.-W. Mao, *Chem. Soc. Rev.*, 2013, **42**, 8360.

34 M. L. Zastrow and V. L. Pecoraro, *Biochemistry*, 2014, **53**, 957–978.

35 K. J. De Almeida, N. A. Murugan, Z. Rinkevicius, H. W. Hugosson, O. Vahtras, H. Ågren and A. Cesar, *Phys Chem Chem Phys*, 2009, **11**, 508–519.

36 S. A. Goldfield and K. N. Raymond, *Inorg. Chem.*, 1971, **10**, 2604–2607.

37 J. D. Silversides, C. C. Allan and S. J. Archibald, *Dalton Trans.*, 2007, 971.

38 B. J. Johnson, E. T. Yukl, V. J. Klema, J. P. Klinman and C. M. Wilmot, *J. Biol. Chem.*, 2013, **288**, 28409–28417.

39 J. Fang, X. Wei, J. B. Sapp and Y. Deng, *Inorganica Chim. Acta*, 2014, **411**, 5–10.

40 S. Chattopadhyay, G. Bocelli, A. Musatti and A. Ghosh, *Inorg. Chem. Commun.*, 2006, **9**, 1053–1057.

41 A. Banerjee, D. Das, P. P. Ray, S. Banerjee and S. Chattopadhyay, *Dalton Trans.*, 2021, **50**, 1721–1732.

42 J. E. Huheey Inorg. Chem., Harper Collins College Publisher, 1993, 387–387

43 C.-Y. Su, S. Liao, M. Wanner, J. Fiedler, C. Zhang, B.-S. Kang and W. Kaim, *Dalton Trans.*, 2003, 189–202.

44 J. S. Pap, B. Kripli, V. Bányai, M. Giorgi, L. Korecz, T. Gajda, D. Árus, J. Kaizer and G. Speier, *Inorganica Chim. Acta*, 2011, **376**, 158–169.

45 Ł. Czekański, S. K. Hoffmann, P. Barczyński, A. Gąsowska, R. Bregier-Jarzębowska, A. Zalewska, J. Goslar, M. Ratajczak-Sitarz and A. Katrusiak, *New J. Chem.*, 2016, **40**, 10526–10535.

46 D. Ghosh, P. K. Bera, M. Kumar, S. H. R. Abdi, N. H. Khan, R. I. Kureshy and H. C. Bajaj, *RSC Adv*, 2014, **4**, 56424–56433.

47 G. Sciortino, J.-D. Maréchal, I. Fábián, N. Lihi and E. Garribba, *J. Inorg. Biochem.*, 2020, **204**, 110953.

48 R. R. Golwankar, A. Kumar, V. W. Day and J. D. Blakemore, *Chem. – Eur. J.*, 2022, **28**, e202200344.

49 A. Kumar, D. Lionetti, V. W. Day and J. D. Blakemore, *Chem. – Eur. J.*, 2018, **24**, 141–149.

50 D. E. Herbert, D. Lionetti, J. Rittle and T. Agapie, *J. Am. Chem. Soc.*, 2013, **135**, 19075–19078.

51 E. Y. Tsui and T. Agapie, *Proc. Natl. Acad. Sci.*, 2013, **110**, 10084–10088.

Findings of the Thesis

The work presented in this thesis originated from an earlier observation of the formation of cyclic trinuclear from three coordinatively saturated Ni(II) octahedral complexes assembled around Na^+ and K^+ ions, using L-leucine derived reduced Schiff base.

In Chapter II, we synthesized a similar cyclic trinuclear, from Cu(II), KNO_3, and L-phenylalanine derived reduced Schiff base, in the ratio of 1:2:1. The ligand is chiral and have an aromatic side-arm. We also synthesize the Cu(II) bis complex, in which the carboxylates are in *trans* orientation. Using this Cu(II) bis complex as a monomer we synthesize the trinuclear in a stepwise manner by simply reacting it with KNO_3 in MeOH. The resultant trinuclear has three chiral clefts inside the pocket formed by the amino acid aromatic side-arm. The three Cu(II) bis complex monomeric units have exclusively *cis*-oriented carboxylates. We then disassembled the trinuclear by adding an excess of [18] crown- 6 and obtained the *cis*-oriented Cu(II) bis complex monomers. Thereby effectively converting *trans* to *cis* monomer. The newly obtained *cis*-oriented Cu(II) monomers readily form back the trinuclear assembly upon the addition of KNO_3. Hence the formation and disassembly of the trinuclear assembly is a reversible process. The process can be monitored by UV-visible and Mass spectrometry.

In Chapter III, we redesign the trinuclear by changing the ligand from aromatic side-arm to hydrophilic side-arm. We used Co(III) instead of Cu(II). The resultant Co(III) bis complex has a different structural motif, in which the phenolate is in the *cis* position. The Co(III) bis complex binds with K^+ to form a polymeric chain instead of a cyclic trinuclear. We also replaced the K^+ ion with Ba^{2+}.

In Chapter IV, using a similar L-threonine-derived ligand we synthesized the Fe(III) complex, which is anionic and its assembly formation with cations of different sizes and charge. Depending on the cations used, the resulting networks are either linear, two-dimensional or three-dimensional. One has the solvent-accessible space occupied with a hydrated chloride. We have not come across any water-soluble recrystallizable chiral coordination polymers. The polymeric chain of [Fe(III), Ba^{2+}] and [Fe(III), Al^{3+}] can be synthesized either directly from ligand or my salt metathesis from [Fe(III), Na^+]. The visible spectra of [Fe(III), Ba^{2+}] in Methanol or water showed ~10 nm shift of the charge transfer bands from [Fe(III), K^+]. However, the addition of Al^{3+} salts showed a significant colour shift. Further investigation confirmed that colour shift is due to partial protonation of the complex with proton generated

from salt hydrolysis. Most reports on visual aluminium detection consider aluminium's binding as the shift's source. Our results show that protonation due to hydrolysis can skew the observation.

In Chapter V, We synthesize the Co(III) complex, the Fe(III) analogue and its assembly with alkali and alkaline earth metal ions using a similar L-threonine-derived ligand. We then replaced the Na^{+} ion with transition metal ions Zn^{2+} and Cu^{2+} to synthesize a more rigid and sturdier assembly and at the same time, it can be better characterized using spectroscopic techniques. The resultant hetero-bimetallic architecture where a Zn(II) or Cu(II) metal ion at the centre bound to a water molecule surrounded by a hydrophilic region is a reminiscence of a hydrolytic enzyme. The hetero-bimetallic complexes [Co(III), M^{n+}] are diamagnetic, hence by using ^{1}H NMR, we employed the concept of charge/ ionic size also known as the polarising power of the cation to quantify the magnitude of the downfield shift of the aromatic protons.

Overall, in this thesis, we synthesized hetero-bimetallic and established the idea of designing a hetero-bimetallic into different shapes and sizes just by changing the secondary cation and we can obtain different structural motifs by changing the metal ions.

List of publications

1. "Water-soluble chiral coordination polymers of Li^+, Na^+, K^+, and Ba^{2+} with an anionic Fe(III) complex of l-threonine derivative and significant red shift of visible spectra with Al^{3+} salt". **Chanreingam L** and Manabendra Ray. Dalton Trans., 2024, https://doi.org/10.1039/D3DT03945E.
2. "Self-assembly triggered the *trans*-to-*cis* conversion of the mononuclear Cu(II) complex via cyclic trinuclear". **Chanreingam L** and Manabendra Ray. Manuscript under preparation.
3. "Stepwise synthesis of a rigid linear trinuclear [Co^{3+}, Zn^{2+}, Co^{3+}] chiral complex with a labile M^{2+} site at the centre". **Chanreingam L** and Manabendra Ray. Manuscript under preparation

Conferences

1. "FICS 2021" Department of Chemistry, Indian Institute of Technology Guwahati. 'Stepwise synthesis of a rigid trinuclear [Co^{3+}, Zn^{2+}, Co^{3+}] chiral complex with a labile Zn(II) site at the centre'.- **Poster presentation**.
2. "MTIC-XVII, 2022, Varanasi" held at BHU, 2022. 'The amino acid side arm determines whether a multinuclear chiral assembly would form or not'. - **Poster presentation**.
3. "Chemistry colloquium" Department of Chemistry. 'Indian Institute of Technology Guwahati Self-assembly triggered the *trans*-to-*cis* conversion of the mononuclear Cu(II) complex via cyclic trinuclear'.- **Oral presentation**.